CHALMERS
UNIVERSITY OF TECHNOLOGY

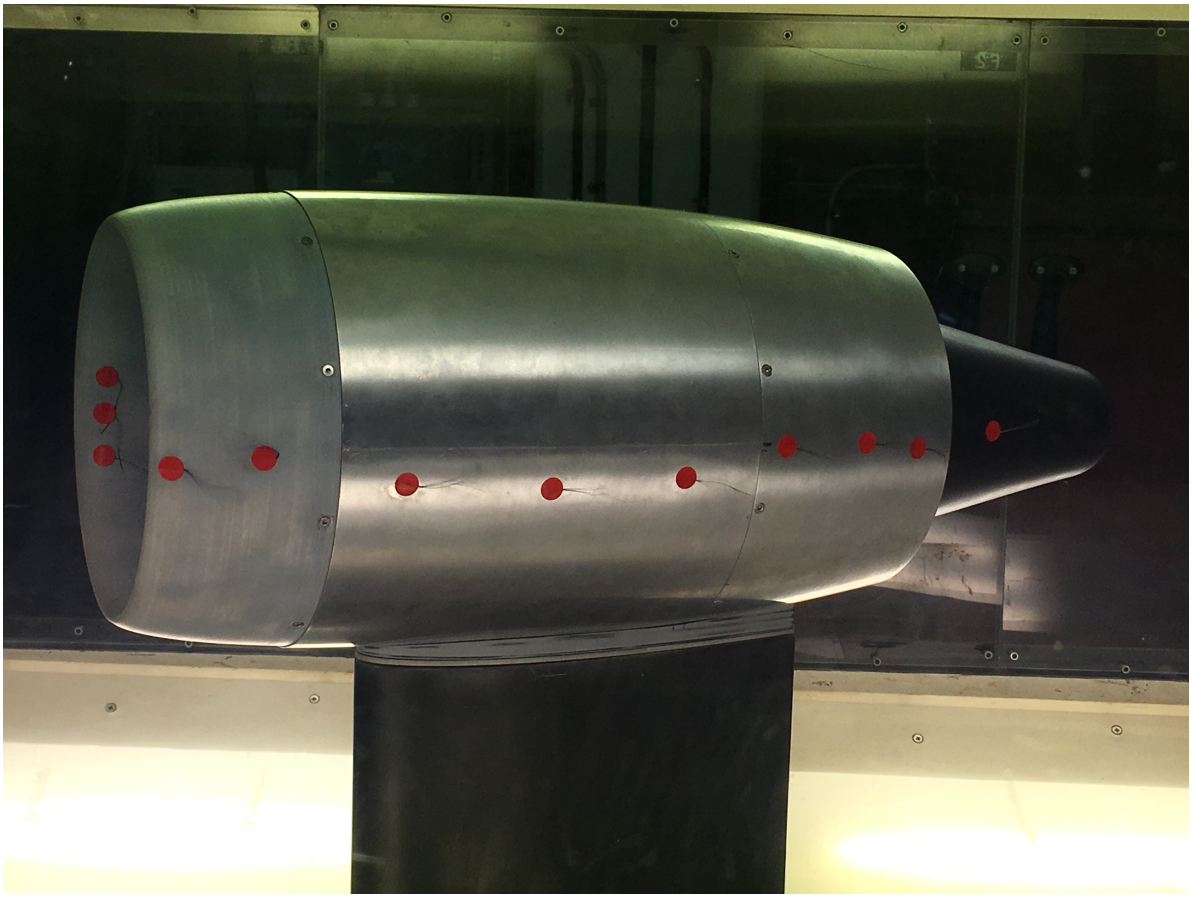

Experimental investigation of a turbofan nacelle at different mass flow ratios and angles of attack.

Master's thesis in Sustainable Energy Systems

JOHANNES DWALIBI

Department of Mechanics and Maritime sciences
CHALMERS UNIVERSITY OF TECHNOLOGY
Gothenburg, Sweden 2019

Master's thesis 2019:105

Experimental investigation of a turbofan nacelle at different mass flow ratios and angles of attack.

JOHANNES DWALIBI

CHALMERS
UNIVERSITY OF TECHNOLOGY

Department of Mechanics and Maritime sciences
Division of Fluid Dynamics
Chalmers University of Technology
Gothenburg, Sweden 2019

Experimental investigation of a turbofan nacelle at different mass flow ratio and angle of attack.
JOHANNES DWALIBI

Supervisors: Vinícius Tavares Silva, Mechanics and Maritime science and Anders Lundbladh, GKN Aerospace
Examiner: Olivier Petit, Mechanics and Maritime sciences.

Master's Thesis 2019:105
Department of Mechanics and Maritime sciences
Division of Fluid Dynamics
Chalmers University of Technology
SE-412 96 Gothenburg
Telephone +46 31 772 1000

Cover: Ongoing tests. The model inside the wind tunnel under the following conditions: Wind tunnel air velocity 30 m/s, AoA=25°and EDF RPM=7873. Surface tufts show flow separation at the lip external and internal surfaces.

Gothenburg, Sweden 2019

Experimental investigation of a turbofan nacelle at different inflow ratios and angle of attacks.

JOHANNES DWALIBI
Department of Mechanics and Maritime sciences
Chalmers University of Technology

Abstract

The air travel sector is rapidly increasing worldwide motivated by the push for greater connectivity in an increasingly globalised economy. The turbofan engine is widely used for aircraft propulsion and it is designed to satisfy the increasing demand for fuel efficiency. As bypass ratio (BPR) increases, the overall efficiency of the engine increases which is a main factor that yields lower specific fuel consumption (SFC). However, high-bypass ratios are accompanied by increased weight and nacelle drag. Therefore, turbofan nacelles require careful design to balance performance benefits of the higher propulsive efficiency against weight and drag penalties. In order to reduce the drag it is necessary to understand how the flow-field around it behaves at different flight conditions. Therefore, a scale model of a powered turbofan nacelle was built and tested at the Chalmers low speed wind tunnel. A 3D axisymmetric nacelle geometry was generated using the class shaped transformation (CST) method which allows for parametric aerodynamic geometry definitions. Furthermore, the geometry is imported to a CAD software, where the mechanical design and assembly modelling were conducted. The model was manufactured, build and tested in the wind tunnel. Measurements of force, fan speed and static pressure were carried out for different angles of attack (AoA) and mass flow ratios (MFR). In addition, surface tufts were used in order to visualise the flow-field, changing angles of attack (AoA) has been conducted using rotary table and mass flow ratios (MFR) have been controlled by varying (EDF) rotational speed in accordance with the wind tunnel air velocity. Results show that the flow around the nacelle body differs substantially depending on whether the fan is turned on or off, suggesting that experiments using flow-through nacelles would not be enough for thoroughly assessing the aerodynamic behaviour of this component. It was also observed that the higher the (MFR) is, the larger the backward forces are.

Keywords:CST, Drag, Axisymmetric nacelle, Angle of attack, Mass flow ratio, Wind tunnel, Load cell, Measurement, Flow visualisation .

Preface

This study has been conducted during the spring and autumn of 2019 and completes the Master's programme Sustainable Energy Systems at Chalmers University of Technology. The study has been led, and carried out in collaboration with GKN Aerospace. The experimental processes were conducted at Chalmers's Department of Applied Mechanics, Gothenburg. The industrial supervisor of this thesis was Anders Lunbladh from GKN who provided assistance on the different phases of the thesis, by holding several discussions and meetings concerning the project. The Academic supervisor was Vinícius Tavares Silva who has been involved in all the details and active to solve all the obstacles encountered throughout the entire process. The examiner was Olivier Petit, Assistant professor at the Division of Fluid dynamics.

Göteborg November 2019.

JOHANNES DWALIBI

Acknowledgements

First of all i would like to thank GKN Aerospace, represented by Anders Lunbladh, for giving me the opportunity to perform this experiment study which gives me a concrete understanding about the nacelle design. I would also appreciate the efforts exerted by Olivier Petit,my examiner, for his valuable directives. The enormous thanks go to my supervisor, Vinícius Tavares Silva, who has followed up and contributed to all the steps leading to accomplish this project.Last but not least i am grateful for having assistance from Valery Chernoray and Isak Jonsson who provided endless cooperation concerning the lab facility, and Reine Nohlborg who helped us machining some parts at Chalmers prototype workshop.

JOHANNES DWALIBI, Gothenburg, 11 2019

Nomenclature

Greek symbols

η_p	–	propulsive efficiency	α	–	Geometric angle of attack
τ	–	Shear stress	ρ	–	Density
ψ	–	Abscissa for CST function	ξ	–	Ordinate for CST function
β_{te}	–	Trailing edge angle			

Other Symbols

C_D	–	Drag coefficient	D_p	–	Pressure drag
L_D	–	Lift coefficient	D_{total}	–	Total drag
q_∞	–	Stream dynamic pressure	D_{ram}	–	Intake momentum drag
V_∞	–	Free stream velocity	F_{nps}	–	Net propulsive force
$\dot{m}$	–	Mass flow	F_{gross}	–	Total thrust force
D_f	–	Friction drag	A_{HL}	–	Highlight area
V_{out}	–	Output voltage	L/D	–	Lift to drag ratio

Abbreviations

SFC	–	Specific fuel consumption	C	–	Class function
BPR	–	Bypass ratio	S	–	Shape function
FPR	–	Fan pressure ratio	c	–	Chord
MFR	–	Mass flow ratio	Pas	–	Pascal
AoA	–	Angle of attack	R	–	Resistance
CST	–	Class-shape Transformation	EDF	–	Electric ducted fan
CC	–	Core cowl			
CFD	–	Computational fluid dynamic	V	–	Velocity
PLA	–	Polyactic acid	P	–	Pressure
CNC	–	Computer numerical control	TIT	–	Turbine inlet temperature
ADC	–	Analog-to-digital converter	OPR	–	Overall pressure ratio
DAQ	–	Data acquisition device	CAD	–	computer-aided design
CO_2	–	Carbon dioxide	NO_x	–	Nitrogen oxides
BPn	–	Bernstein polynomial of order n	L	–	Length
r	–	Radius	M	–	Mach number

Contents

1
Introduction

1.1 Background

The last fifty years have witnessed a huge growth in air travel sector which has been accompanied with two substantial criteria, travelling faster and consuming less fuel. These two requirements go one against the other. Civil aviation sector has been dominated by the turbofan engines, also called *bypass engines*, which have been designed achieve a high propulsive efficiency η_p and a low specific fuel consumption SFC. These improvements are realised by employing higher BPR and lower *Fan Pressure Ratio* FPR. Structurally, the entire engine is enclosed into a nacelle which is conventionality attached to the aircraft wing by means of a pylon, the whole assembly is called the 'pod' [1].
According to [1] the negative influence of 'pod' drag on propulsion efficiency η_p occurs particularly at high values of BPR. Hence reducing the 'pod' drag contributes to a reduction in fuel consumption and greenhouse gas emissions, and subsequently to a decrease of CO_2 footprint.

Flightpath 2050, the Europe's Vision for Aviation, calls for 50% overall CO_2 emission reduction by 2050, which is equivalent to 75% reduction of CO_2 emission per passenger kilometre, and a 90% reduction in NOx emissions.These challenges are Inextricably linked to reducing the drag in turbofan nacelles [2].

GKN Aerospace and Chalmers have unified their efforts and expertise aiming to perform experimental research in high bypass turbofan nacelles. This thesis consists of building and testing a scale model of a powered turbofan nacelle in the Chalmers low speed wind tunnel. The goal is to be able to evaluate the influence of different mass flow ratios and angles of attack in the nacelle drag.

1.2 Goal

The main objective of this study is to design and build a scale model of a powered high bypass turbofan nacelle to be tested in the Chalmers low speed wind tunnel. The goal is to be able to measure the nacelle drag under different wind tunnel conditions. The test rig consists of an electric ducted fan (EDF) surrounded by a nacelle designed to be flexible for testing different intake geometries. Measuring the nacelle drag under different mass flow ratios and angles of attack, is the key result expected from this project.

1.3 Limitation

Linked to the project work of measuring the drag of an axisymetric nacelle, the main limitations are:

1.3.1 Flow similarity

One of the drawbacks of using the available low speed wind tunnel is the difficulty to achieve flow similarity between the high speed flight conditions and the wind tunnel test section, for more details about this limitation see section 2.3. Hence, the experiment fails to achieve identical C_D and C_L between a real turbofan nacelle and the scale model. Those parameters would have been used to predict the real $drag$ and $lift$ forces applied on a real nacelle [3]. Therefore, flow similarity can only be achieved by low speed flight conditions, such as take-off, climbing and descent.

1.3.2 The core engine

In this study the scale model nacelle is powered by an electric ducted fan (EDF) and not a gas turbine engine as a real aircraft nacelle would be. It is not feasible to use a gas turbine engine inside the wind tunnel which is at this experiment's disposal. Since in EDF's the flow is no longer split between the core engine and the bypass duct, some adaptations were required in the nacelle design. The core cowl was designed for not allowing the 'hot stream' to enter it. Therefore, the portion consisting of the hot nozzle and plug in a turbofan engine was replaced by a spherical surface as it can be seen in section 3.1.6.

2

Theory

This chapter describes the theory associated to this work necessary to the reader understand the functionality of a turbofan engine and its nacelle, it is also given some glimpse about the measurements and flow similarity.

2.1 Turbofan engine and nacelle

The turbofan engine employs an annular bypass duct wherein a large portion of the total flow, called the *cold stream*, bypasses the core path and is often ejected through a separate cold nozzle. The core flow or *hot stream* travels downstream from the inlet fan to the compressor, combustion chamber, turbine and finally ejected through the hot nozzle. Figure 2.1 illustrates the different components of the turbofan engine. In doing so, the mean jet velocity is decreased and therefore the propulsion efficiency η_p is increased. From its nomenclature the turbofan engine or *bypass engine* is mainly described by its *bypass ratio* BPR which is defined by the ratio of the cold stream over the hot stream mass flows $BPR = \dot{m}_c/\dot{m}_h$. As mentioned before the entire turbofan engine is enclosed into a nacelle attached to the aircraft wings by means of a pylon, the combination of these components is called the 'pod' [1].

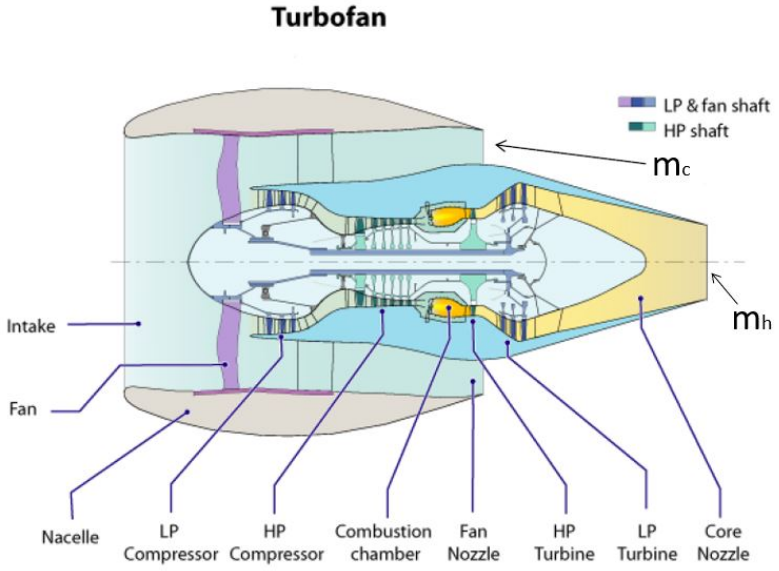

Figure 2.1: Turbo fan engine components [4]

2.1.1 Optimisation of Turbofan engine

Several parameters contribute to the optimisation of the turbofan engine. While *Overall Pressure Ratio* OPR and *Turbine Inlet Temperature* TIT determine the quality of the engine, BPR and FPR govern the engine effectiveness to transform the input energy to useful thrust. The trend to improve the SFC is illustrated in the figures 2.2a and 2.2b. Figure 2.2a shows that there has been a steady decrease

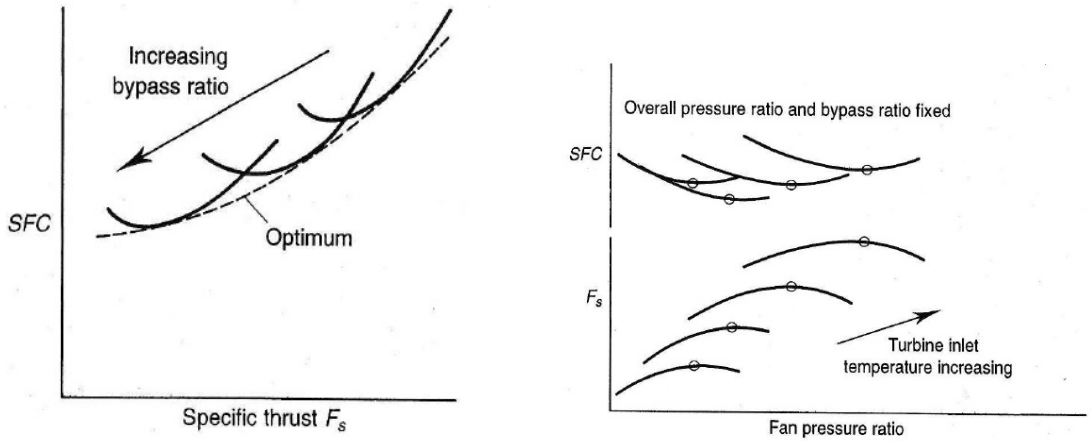

(a) SFC Vs BPR **(b)** SFC Vs FPR

Figure 2.2: SFC optimisation [1]

in SFC by increasing BPR. Meanwhile figure 2.2b reveals that a gradual rise in FPR leads to a marked increase in SFC. High BPR and low FPR engines require large fan diameter and accordingly nacelle size. The choice of having this engine configuration can critically affect the 'pod' drag [1]. Figure 2.3 depicts the effect of that drag on the propulsion efficiency η_p. It can be noticed that at the desirable feature of high BPRs, η_p is very sensitive and it has steep fall for a slight increase of α, which is defined as:

$$\alpha = \frac{pod\,drag}{momentum\,drag} \tag{2.1}$$

Here rises the need to understand the behaviour of nacelle drag at different conditions i.e. different mass flow ratios and angles of attack which they are explained in section 2.1.3

2.1.2 Drag and thrust bookkeeping

The four types of drag, acting on the real nacelle, are [5]:

- The interference drag: Occurs when two components intersect each other so their boundary layers interact and become thicker causing more drag. In other words, two components brought together will generate a drag higher than the sum of their separate drags[6]. The interference drag has not been analysed in this experiment assuming the nacelle as isolated body .

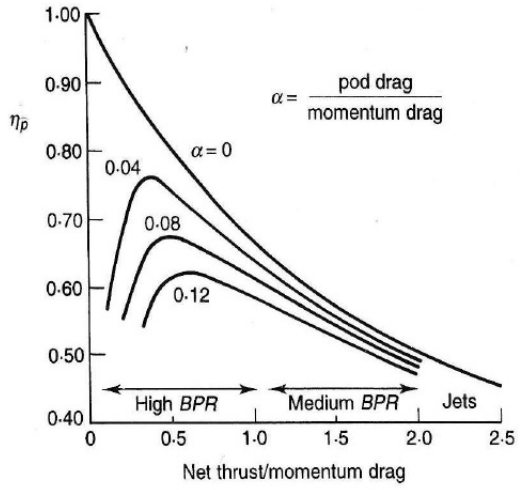

Figure 2.3: Effect of 'pod' drag on propulsion efficiency [1]

- The profile drag: Is the main components of drag that is measured in the current experiment. It is composed of two parts: skin friction drag D_f and pressure drag D_p while the first is the integral of the shear stress τ over the nacelle body, the second denotes for the integral of the pressure distribution over the nacelle outer area. Hence, the latter is due to flow separation and both are acting on the outer surface of the nacelle. [7, 8].
- The wave drag: It occurs due to compressibility effects due to the formation of shock waves and it is part of the pressure drag [6]. Since the flow regime in this study is limited to *subsonic* regime hence, the wave drag is excluded.
- The spillage drag: This type of drag occurs when the amount of mass flow crossing the fan is less than the amount of mass flow entering the inlet duct. Consequently the excess amount of this mass flow is *spilled out* from the inlet duct and goes out around the cowl lip. In turns the pressure at the rear side of the nacelle decreases and contributes in increasing the drag [5].

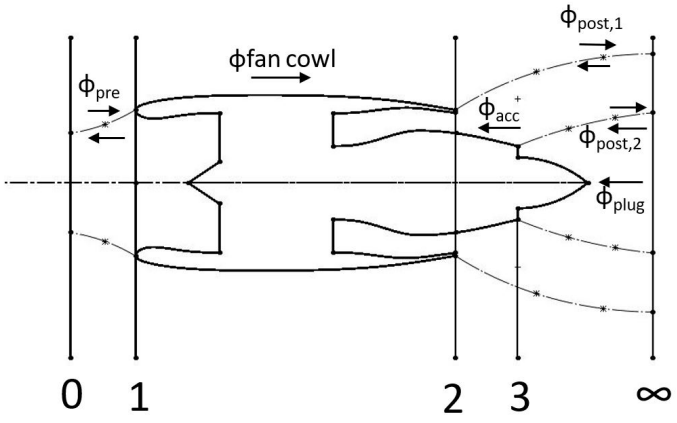

Figure 2.4: Forces acting on turbofan nacelle

The forces acting on the nacelle could be sorted in three groups: pre-entry, nacelle and post-exit forces. These are illustrated in Figure 2.4 which depicts as well the

streamtubes entering and exiting the nacelle.
The pre-entry forces are obtained by calculating the pressure forces and momentum flux applied on the streamtube in front of the nacelle between station 0 and 1. See Figure 2.4, the corresponding equation [5] is:

$$\phi_{pre} = \int_{A1} PdA + \dot{m}_1 V_1 - (\int_{A0} PdA + \dot{m}_0 V_0) \tag{2.2}$$

It is good to highlight that theoretically the cowl surface is split into two parts fore-body covering from the front end of the nacelle to the maximum cowl radius and the after-body covering from the ridge till the rear end of the nacelle. Hence the subject drag is decomposed into two parts: fore-body and after-body, denoted respectively by the subscripts f and a. Finally the nacelle drag would be presented as follow:

$$\begin{aligned} D_{nacelle,f} &= \phi_{pre} + \phi_{nacelle,f} \\ D_{nacelle,a} &= \phi_{post} + \phi_{nacelle,a} \end{aligned} \tag{2.3}$$

The post-exit forces $\phi_{post,1}$ and $\phi_{post,2}$ designate the cold stream and core stream forces respectively. However $\phi_{fan-cowl}$, ϕ_{acc} and ϕ_{plug} denote the drag emanated on the following surfaces: the nacelle cowl, the after core cowl and the exhaust plug.
For the sake of simplicity, let's define the total drag as D_{total} and the total thrust force generated by the fan as F_{gross} the intake momentum drag as D_{ram} so the net propulsive force F_{nps} could be computed as follow [5, 1]:

$$\begin{aligned} F_{net} &= F_{gross} - D_{ram} \\ D_{ram} &= \dot{m}_{inlet} V_0 \\ F_{nps} &= F_{net} - D_{total} \end{aligned} \tag{2.4}$$

The above definitions and equations are true for the real turbofan engine i.e. when the engine comprises fan, compressor, combustion chamber, turbine and exhaust nozzle. However, the model which is designed and built for the purpose of this study has some modifications due to the limitation mentioned in 1.3.2. Having stated that, the measured drag on the built model represents $\phi_{fan-cowl}$ in other term the *profile drag* acting on the surface of fan cowl. Figure 2.5 shows cross section for the model wherein the hot exhaust nozzle and the plug are omitted and replaced by the core cowl CC. More details about this modification are presented in section 3.1.6.

2.1.3 Mass flow ratio and angle of attack

In this section it will be presented an overview about the definition of the mass flow ratio as well as the angle of attack (AoA). These quantities are the main variables to be changed during the wind tunnel tests, in order to assess their influence in the nacelle's drag.

- Mass flow ratio

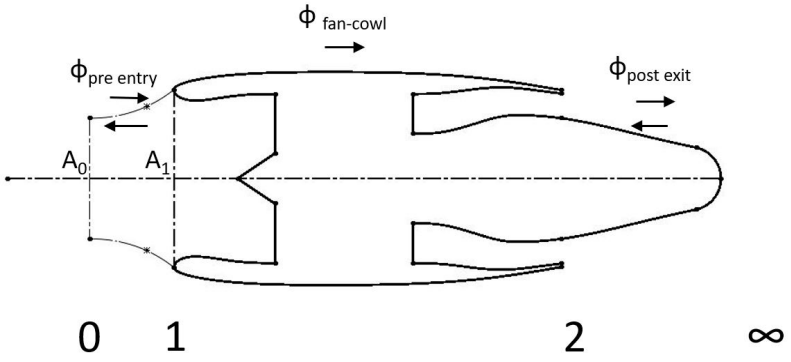

Figure 2.5: Drag forces distribution over the built model

The mass flow ratio MFR is defined as the ratio of streamtube capture area A_0 and the highlight area A_{HL}[9]

$$MFR = A_0/A_{HL} \tag{2.5}$$

As the MFR is increased to values greater than 1, the stagnation point tends to move downstream of the external lip surface and the streamlines will have a behavior similar to the one presented in figure 2.6b . On the contrary, if the mass flow is decreased to values lesser than one, the stagnation point will shift to the inner surface of the lip, as shown in figure 2.6a. The MFR can be controlled in a wind tunnel by changing either the wind or the fan speed. The more the fan speed is increased the higher will be the streamtube capture area and hence the MFR will be greater. Similarly, lower mass flow ratios will be achieved for higher wind tunnel speeds.

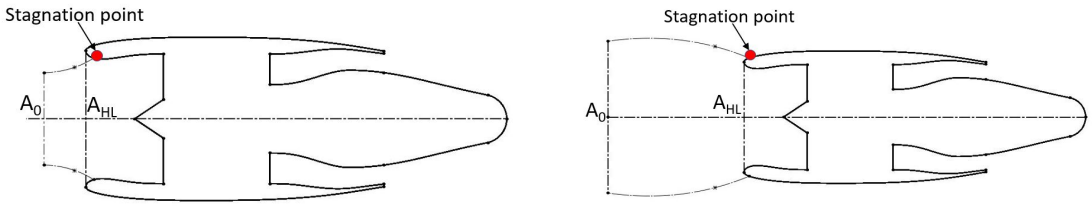

(a) Mass flow ratio at cruise condition **(b)** Mass flow ratio at take-off condition

Figure 2.6: MFR vs Stagnation points

- Angle of attack.

  The angle of attack defined between the axis of an axisymetric nacelle and the direction of V_∞ (the relative wind) is called the *geometric angle of attack* α [8], as illustrated in figure 2.7a. A positive angle of attack is required in cruise to mitigate the effects of the wing upwash and during take-off and climbing the angles of attack can reach values between 204.13 and 304.13.

- Droop angle and non-axisymetric nacelle.

  The nacelle is usually designed with a droop angle between 3°and 6°. This is to ensure that the nacelle face is orthogonal to the inlet streamlines [9] which are

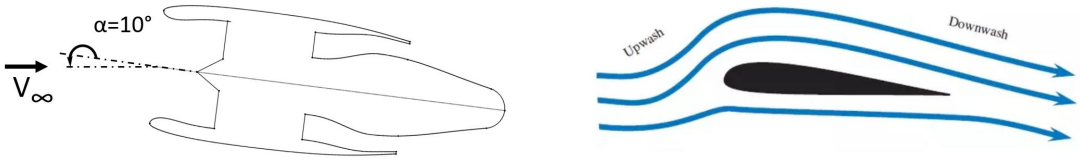

(a) AoA for an axisymetric nacelle **(b)** Wing upwash phenomenon

Figure 2.7: AoA and wing upwash

deviated upward from the horizontal line due to wing upwash phenomenon which is illustrated in figure 2.7b. On the other hand, separation plays a substantial role in drag generation particularly during take-off and climbing, therefore, thicker inlet lips with round leading edges are imposed on the bottom section of the lip in order to get rid of these separations and increase the inlet overall performance[9]. Moreover, some nacelles can be flattened in section of the intake in order to increase the ground clearance. Figure 2.8 depicts the discussed parameters that make the nacelle asymmetric. As mentioned previously this study is not taking in consideration any of these factors and we limit the design to an axisymmetric nacelle.

(a) Droop angle [10] **(b)** Bottom section lip [11]

Figure 2.8: Assymetric nacelle

2.2 Measurements

In this section it will be presented both the theory behind the measurement techniques used in this thesis and a brief overview on the data acquisition procedure. Error and uncertainty calculation are addressed as well.

2.2.1 Load cells

The load cell, also called force transducer, consists of a solid piece of metal, mainly Aluminium, which can sustain and measure the applied forces. Its performance rely mainly on the capability of responding and deflecting when loads are applied and removed sequentially. The load cell mechanism consists of converting an input

mechanical load into an output signal. The load cell would be classified based on its type of output signal e.g. electric, pneumatic and hydraulic. The frequently utilised load cell is the strain gauge type, which has an electric output signal as a response to an applied mechanical load. Strain gauge load cells provide an accuracy ranging between 0.03% and 0.25% of the full scale and this type of load cell could be employed to a wide variety of industrial applications [12].
All the strain gauge load cells are employing *the Wheatstone bridge circuit* as shown in the figure below, comprising a network of four resistances bridge arms $R1...R4$.

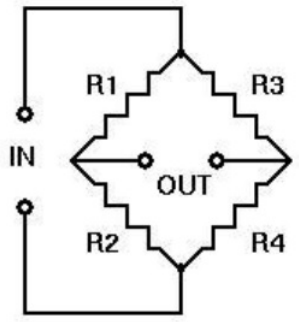

Figure 2.9: Wheatstone bridge

The setup is equivalent to two parallel voltage divider circuit (R_1&R_2) from one side and (R_3&R_4) from the other side. The output signal is taken and measured from the middle nodes of the two aforementioned circuits. The measuring concept employs a spring referred to as *sensing element* which leans when the forces/loads are applied or due to temperature changes.In figure 2.9 if one resistance is strain gauge then the network is quarter bridge. If two resistances are strain gauges the network is called half bridge however if all the resistances are strain gauges then it is known as full bridge [12]. Figure 2.10 shows the working concept of strain gauge. It can be noticed that a tension force tends to narrow the area delimited by the strain sensitive pattern which gives rise to resistance at the terminals. Conversely, compression force leads to a thicker area of the strain pattern and therefore lower resistance is obtained at the terminals. Increase or decrease in the circuit resistance results in an output voltage V_{out} that is proportional to the force applied to it.

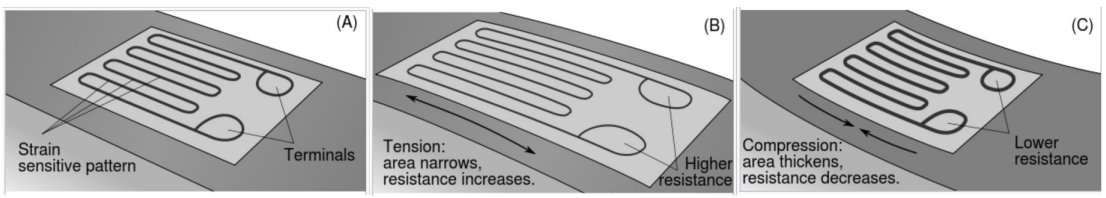

Figure 2.10: working concept behind the strain gauge [13]

Several errors can be encountered while using an electric load cell unit. The type of these errors and their sources are listed below [12]:

- Non-linearity: this type of error is observed when load cell signal output is no more a linear function of the force input.
- Hysteresis: when a load force is increased from "zero" to "rated output" the reading follows certain curve however, the same reading follows another curve when the applied load force is decreased from the "rated output" to "zero". The maximum difference between these two curves is called hysteresis. The hysteresis error value is normally specified as percentage of the rated output.
- Temperature effect: the sensing element is made often from metal such as steel, stainless steel, aluminium or a copper-beryllium alloy, which have a non-linear length expansion once they are exposed to temperature changes. Load cells are designed to compensate the temperature shift effect, however, resilient temperature changes might impose considerable errors which exceed the allowable tolerance.
- Creep: is the error obtained when the output signal changes with the time. The creep could be positive or negative. In order to avoid creep, the measurements shall be done rapidly when the load is applied.

2.2.2 Measurement chain, Errors and Uncertainty

- In practice the measurement of a certain physical property is not taken in direct manner. Instead, the measurement chain is employed to evaluate the desired property [14]. It is composed of several components such as the probe, the transducer, manipulation element and finally the display or acquisition system. The probe senses the physical property (g) and transforms it into a signal detectable by a transducer. Example of probes: pitot tube thin film, hot wire.., etc. The transducer is an energy conversion device. It converts the physical quantity received from the probe into an electrical form (f). This new form of signal,the electrical form, has effective features such as amplification, conversion, transmission and quick response. The manipulation element is employed to minimise signal's alteration and could be an amplifier, filter or emitter. Display or acquisition element is used to convert the output of the previous component into an interpretable form. The several elements are arranged sequentially as depicted in figure 2.11 [14]

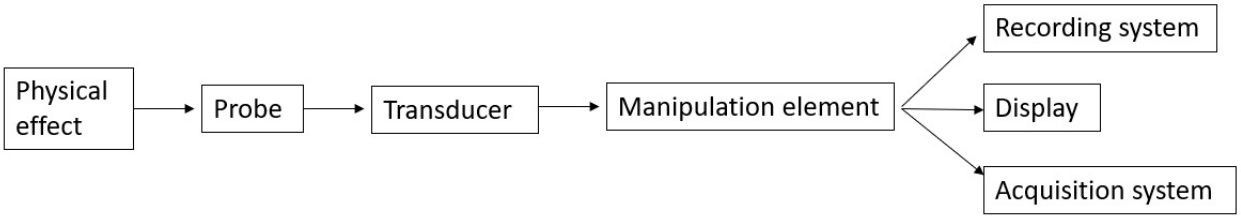

Figure 2.11: Description of the mesurement chain

- Errors and Uncertainty [14] are two different concepts. The error express the difference between *the real* and *the corrected* values and can be of two different types: Random error and Bias error. The former represents a standard deviation about a certain mean while the latter is fixed,constant and systematic. However the uncertainty outlines the possible range that the error might vary within it. e.g.

$$\alpha = 500W/m^2K \quad \pm 25W/m^2K \quad (20:1) \tag{2.6}$$

the term $\pm 25W/m^2K$ represents the uncertainty while the confidence level is expressed by $(20:1)$ which means if 20 experiments have been conducted 1 will fall outside the range of 475...525. It is notable that for a given confidence level, when experiments are conducted with larger care, uncertainty decreases.

2.3 Flow similarity

It is well known that satisfying flow similarity is inevitable in order to have a promising aerodynamic experiment. This section brings an overview of what flow similarity is and what are the benefits of fulfilling its requirements.
The *lift coefficient* C_L and *drag coefficient* C_D, for a certain aerodynamic body, can be defined in function of *the free stream dynamic pressure* q_∞.

$$q_\infty = \frac{1}{2}\rho_\infty V_\infty \tag{2.7}$$

where ρ_∞ and V_∞ are the density and velocity , respectively, in the free stream, far ahead of the body.

$$\begin{aligned} C_L &= \frac{L}{q_\infty S} \\ C_D &= \frac{D}{q_\infty S} \end{aligned} \tag{2.8}$$

L is the lift force, D is the drag force applied on the body and S is the reference area. The choice of S is arbitrary and will depend on the body geometry. It can be the cross section area for a sphere or the planform area for an airplane wing [7, 8]
It is particularly interesting to calculate *lift-to-drag ratio* L/D, which defines the aerodynamic efficiency of a body shape. Hence, it has the vital effect on the energy needed to make an aerodynamic body move in the air. The higher L/D the lower energy needed and the higher energy efficiency obtained. Examining the equation 2.8 it can be straightforward deduced equation 2.9

$$\frac{L}{D} = \frac{C_L}{C_D} \tag{2.9}$$

On the other hand it has been proven that the dimensionless coefficients C_L & C_D could be correlated to Reynolds number (Re), free stream Mach number (M_∞) and

angle of attack (α) using dimensionless analysis or *Buckingham pi Theorem*. Hence equation 2.10 reads

$$\begin{aligned} C_L &= f_1(R_e, M_\infty, \alpha) \\ C_D &= f_2(R_e, M_\infty, \alpha) \end{aligned} \tag{2.10}$$

Two flows are dynamically similar if:

1. The bodies and any other solid boundaries are geometrically similar for both flows.
2. The similarity parameters (R_e, M_∞, α) are the same for both flows .

Therefore, in a limited sense, but applicable to many problems, we can say that flows over geometrically similar bodies at the same Mach and Reynolds numbers are *dynamically similar* [7], and hence the lift and drag coefficients will be identical for the bodies. This is a key point in the validity of wind-tunnel testing. If a scale model, such as a nacelle, is tested in a wind tunnel, the measured lift and drag coefficients will be the same as for free flight as long as the Mach and Reynolds numbers of the wind-tunnel test-section flow are the same as for the free flight case. Bearing in mind that there are other similarity parameters such as specific heat could influence the flow. In addition, differences in freestream turbulence between the wind tunnel and free flight can have an important effect on C_D and the maximum value of C_L.

In order to make the above concept more concrete for the reader we present a simple numerical example of similarity requirement. Assuming an aircraft flying at 885 km/h at standard altitude of 11,582 m which has its corresponding pressure and temperature of 20,712 Pa and 216 K respectively. The model is tested in wind tunnel where the temperature is 238 K. In order to have flow similarity conditions wind tunnel test section must have a velocity of 929 km/h and pressure 11 *bar* [7]. Most standard subsonic wind tunnels are not pressurised as such because of the extra large financial cost involved [7]. Today for the most part experiments do not attempt to simulate all the parameters simultaneously: rather, Mach number simulation is achieved in one wind tunnel, and Reynolds number simulation in another tunnel. The results from both tunnels are analysed and correlated to obtain reasonable values of C_L and C_D.
For a nacelle the mass flow ratio is of similar importance as the angle of attack for a wing, determining external and internal pressure distributions, stagnation and separation points. By selecting the wind tunnel speed and fan speed, flow similarity can be achieved relative this parameter for cases corresponding to take-off, climb and cruise. At the Chalmers low speed wind tunnel, the wind speed is limited to 60 m/s. Therefore, experiments can achieve Mach number similarity at low speed conditions only, where low speed refers to ISA, sea level conditions and Mach numbers typical of take-off. However, due to the low inlet Mach number, limited by the fan power for full turbofan power cases we have to sacrifice the similarity relative to Mach number altogether to achieve the correct mass flow ratio. The simultaneous correct mass flow ratio and Mach number can only be achieved for cases corresponding to part power for the full scale turbofan and low external speed. These cases are of low interest to us. As noted above, without pressurisation viscous similarity is not

possible for a sub-scale nacelle, but we can hope to reach high enough Reynolds number (above roughly half a million) to get turbulent boundary layers and thus results which can be correlated with flow calculations.

3
Methods

3.1 Nacelle Geometry

In this section the paper presents the method led to the geometry generation of the modelled nacelle. The CST method is explained with its related constraints and inputs. Several geometry outputs from the different phases are shown at the end of this section.

3.1.1 Class Shape Transformation method introduction

The nacelle could be described mathematically by a continuous but non-analytic function because at the round nose the slope goes to infinity and because of the corresponding large variations of curvature over the surface. Hence a huge number of coordinates are required to define the geometry. This raises the need of a fundamental geometric transformation technique which comprise a simple analytic and well behaved "*Shape function*". This function controls and describes the geometric key parameters such as leading edge radius, trailing edge boattail angle, and closure to a specified aft thickness. The "*class function*" generalises the method for a large variety of geometries. The "shape function" and "class function" are combined in the class shape transformation (CST) methodology, which provides an innovative and reliable approach for describing rather arbitrary 2D and 3D geometries [15].

3.1.2 Development of CST

The CST method is described by a class function $C(\psi)$, a shape function $S(\psi)$ and a term for defining the vertical offset between the end points, as it can be seen in equation 3.5
The general form of a class function is defined as:

$$C(\psi) = \psi^{N1}(1-\psi)^{N2} \tag{3.1}$$

where $\psi = x/c$, c is the cord length. The values of the exponents N1 and N2 of the class function, define the basic class of geometries. As it can be seen in figure 3.1 several geometries were generated from the fact of varying the exponents N1 and N2 , for an unitary shape function $S(\psi) = 1$) [15]. In particular we are interested in obtaining round nose and pointed aftbody, these characteristics are fulfilled in case where

$$N1 = 0.5 \;\; and \;\; N2 = 1.0 \tag{3.2}$$

It is important to notice that the shape function $S_n(x/c)$ is remained equal to "1", it means the shape function does not have any contribution in *shaping* the geometry.

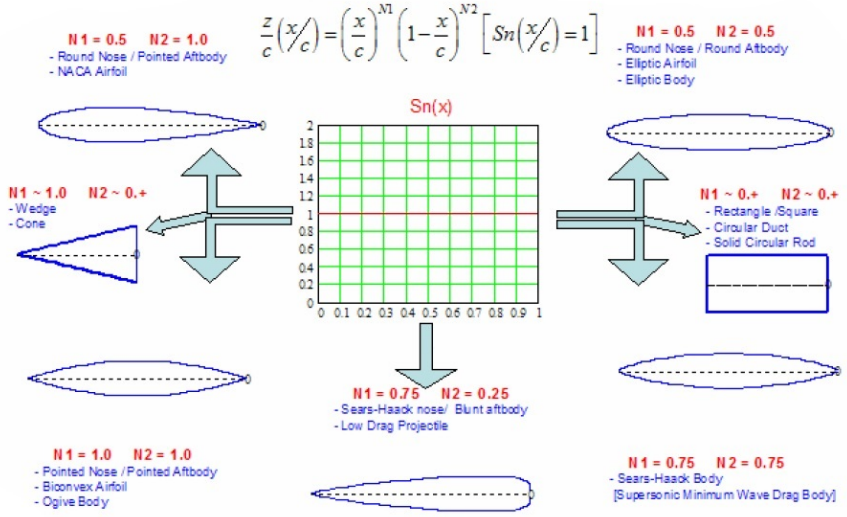

Figure 3.1: Fundamental geometry class emanated from unity "1" [15]

In order to shape the geometry setup, it is necessary to decompose the shape function into Bernstein polynomials which have the mathematical property of "Partition of Unity". The definition of a Bernstein polynomial of order n, BPn, is [16, 15]:

$$\begin{aligned} BPn &= \sum_{i=0}^{n} K_{i,n}\psi^i(1-\psi)^{n-i} \\ BPi,n &= K_{i,n}\psi^i(1-\psi)^{n-i} \\ BPn &= 1 \end{aligned} \tag{3.3}$$

The variable ψ is limited to values from 0 to 1. The coefficients factors $K_{i,n}$ are binominal coefficients defined as:

$$K_{i,n} = \frac{n!}{i!(n-i)!} \tag{3.4}$$

The CST curve is now constructed from weighting each component of the Bernstein polynomials before summing them and then multiplying the class function, so

$$\xi(\psi) = C(\psi)S(\psi) + \psi\Delta\xi t_e \tag{3.5}$$

$$\xi(\psi) = \psi^{0.5}(1-\psi)\sum_{i=0}^{n} bp_i BPi,n + \psi\Delta\xi t_e \tag{3.6}$$

where bp_i are called the weighting coefficients and the term $\psi\Delta\xi t_e$ is added to control the closing of the trailing edge. If all the weighting coefficients were equal to one, the shape function would not have any effects on the class function, because the summation of the Bernstein polynomials would be equal to one.

3.1.3 CST Constraints

Certain constraints need to be implemented on the profile curve, ξ , in order to solve the weighting coefficients bp_i by the mean of system of linear equations. The constraints related to the outside fan cowl curve are addressed in this paragraph then in the further part the constraints required to define the inlet curve are investigated. These constraints are presented in figure 3.2.

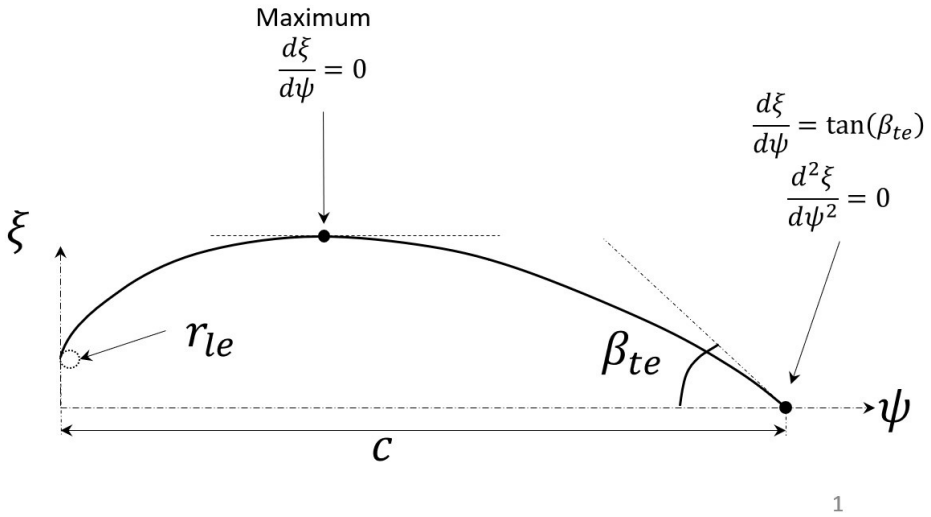

Figure 3.2: Constraints applied on the cowl curve

In the present thesis, fourth order Bernstein Polynomials are used (n=4). This leads to five (5) unknown weighting coefficients $bp_0 ... bp_4$. Two among them, bp_0 and bp_4 are straightforward computed from the input parameters. Hence, we still need three conditions to solve or to *close the system* with the three other coefficients bp_1,bp_2 and bp_3. Those conditions are:

- The Maximum ξ_{max} and the position of the maximum $\psi(\xi_{max})$.
- The first derivative, which represents the tangent (or slope), at the maximum is equal to "0"

$$\frac{d\xi}{d\psi} = 0 \tag{3.7}$$

- Impose the second derivative at the trailing edge to be zero. It is worth mentioning that the second derivative describes the concavity of the curve, when it is positive, the curve is upwardly concave and conversely when it is negative the curve is downwardly concave. An inflection point marks the transition from concave up and concave down. The second derivative will be zero at an inflection point which in this case the trailing edge point.

$$\frac{d^2\xi}{d\psi^2} = 0 \tag{3.8}$$

Writing the equation 3.6 on matrix form :

$$B = AX \tag{3.9}$$

$$B = \begin{bmatrix} b_1 \\ b_2 \\ b_3 \end{bmatrix} A = \begin{bmatrix} a_{1,1} & a_{1,2} & a_{1,3} \\ a_{2,1} & a_{2,2} & a_{2,3} \\ a_{3,1} & a_{3,2} & a_{3,3} \end{bmatrix} X = \begin{bmatrix} bp_1 \\ bp_2 \\ bp_3 \end{bmatrix}$$

where the components of the matrices B and A are as follow [16]:

$$\begin{aligned} b_1 &= \xi(\psi) - (bp_0 BP_{i=0,4}(\psi) + bp_4 BP_{i=4,4}(\psi))C(\psi) - \psi\Delta\xi_{te} \\ b_2 &= \frac{d}{d\psi} b_1 \\ b_3 &= \frac{d^2}{d\psi^2} b_1 \end{aligned} \tag{3.10}$$

$$\begin{aligned} a_{1,j} &= (BP_{j=1,4}(\psi) + BP_{j=2,4}(\psi) + BP_{j=3,4}(\psi))C(\psi) \\ a_{2,j} &= \frac{d}{d\psi} a_{1,j} \\ a_{3,j} &= \frac{d^2}{d\psi^2} a_{1,j} \end{aligned} \tag{3.11}$$

where j=1,2,3. Once the terms in equations 3.10 and 3.11 are obtained, it is straightforward to compute the three unknown coefficients bp_1,bp_2 and bp_3.
However, bp_0 is deduced from the the initial fore-body radius r_{le} correlated by the below equation [16]:

$$bp_0 = \sqrt{\frac{2r_{le}}{L_{cowl}}} \tag{3.12}$$

where L_{cowl} is the the cowl length denoted by c in figure 3.2. The coefficient bp_4 is related to the boattail angle β_{te} through the following equation:

$$bp_4 = tan(\beta_{te}) + \frac{\Delta\xi_{te}}{L_{cowl}} \tag{3.13}$$

Hence, the CST function presented in equation 3.6 could be fully developed and built.

On the other hand figure 3.3 depicts the main conditions necessary to develop the inlet curve, these conditions are [17]:

- Throat station.
- Throat area or radius.
- End of inlet station.
- End of inlet area or radius.

In addition to the above listed constraints it is necessary to match the inlet and cowl nose radius. Five conditions are set and accordingly five linear equations are employed to solve the five unknowns bp_0...bp_4 emanated from the fourth order Bernstein polynomial. The procedure is quite similar to the methodology utilised for building the cowl curve.

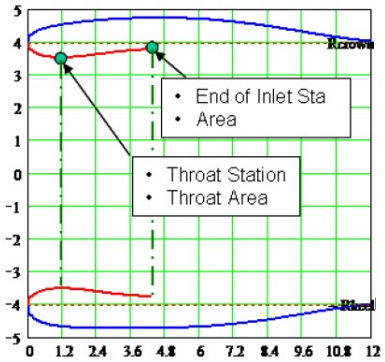

Figure 3.3: Constraints to build inlet curve [17]

It is important to highlight that the exhaust duct and core cowl are made of CST curve, and their details can be found in [16].

3.1.4 Input parameters to CST

In order to generate the nacelle geometry a MATLAB based tool was implemented in the master thesis [16] and further adapted especially for the test rig setup. In particular, the MATLAB function requires five inputs data presented and explained briefly in table 3.1.

Input	Definition	Specification
g(1)	r_{max}/r_{hi}	Height of the nacelle profile
g(2)	f_{max}	Location of the max radius in % of the nacelle length
g(3)	$f_{if} = \frac{r_{if} f_{max} l_{tot}}{(r_{max} - r_{hi})^2}$	Non-dimensional initial fore-body radius $\simeq 0.796$
g(4)	$\frac{r_{te} - r_{hi}}{r_{hi}}$	Non-dimensional trailing edge displacement
g(5)	β_{te}	Trailing edge angle

Table 3.1: Input to CST method

The obtained ordinates from the MATLAB function ψ and ξ are scaled by the profile length either $L_{fan\ cowl}$ or L_{inlet}. Bearing in mind that, the vertical ordinate ξ has to be shifted by the highlight radius. The scaling summary can be presented as follow

$$x_{fan\ cowl} = \psi L_{fan\ cowl} \tag{3.14}$$
$$y_{fan\ cowl} = r_{hi} + \xi L_{fan\ cowl} \tag{3.15}$$
$$x_{inlet} = \psi L_{inlet} \tag{3.16}$$
$$y_{inlet} = r_{hi} + \xi L_{inlet} \tag{3.17}$$

Since the aim of this thesis is experimental measurement for the nacelle drag it has been decided not to investigate further in the geometry generation.

3.1.5 Sample of geometry generated

The nacelle geometry is represented by a .csv file created by the MATLAB based tool. These points are imported into the ANSYS ICEM meshing software, for CFD simulations, and automatically converted into a 3D geometry. For the sake of simplicity, the ANSYS tools were used for generating the nacelle CAD geometry. The output geometry file (.tin) generated by ICEM was exported to the ANSYS SPACECLAIM software, which, in turn, is able to generate STEP files. The STEP files are compatible to the SOLIDWORKS software, which was used to fulfill the mechanical design of the rig. This apparently laborious procedure makes possible to avoid working with STL surface files within SOLIDWORKS, which can be time consuming and generate several geometry imperfections. Figure 3.5a shows the 2D longitudinal curves of an axisymmetric nacelle generated by the MATLAB code. It can be seen that the nacelle consists of three main curves: Fan cowl, inlet and exhaust duct. The core engine curve consists of the fan and the aft core cowl. Figure 3.5b illustrates the 3D model generated by the MATLAB code. The one piece CAD model and Figure 3.5d shows a general view for the assembled model.

3.1.6 Difference between real and adapted geometry

This subsection presents the main difference between the original turbofan nacelle geometry and the modified geometry of the scale model used for this experiment. With reference to figure 3.4, bottom profile illustrates the real turbofan nacelle geometry wherein the hot exhaust nozzle, the plug and the real core cowl are denoted by A, B and C respectively. The top profile shows the adapted geometry of the scale model for this study. It can be seen that A and B are simulated with a round afterbody R tangent to C, to constitute what is called in this thesis core cowl CC.

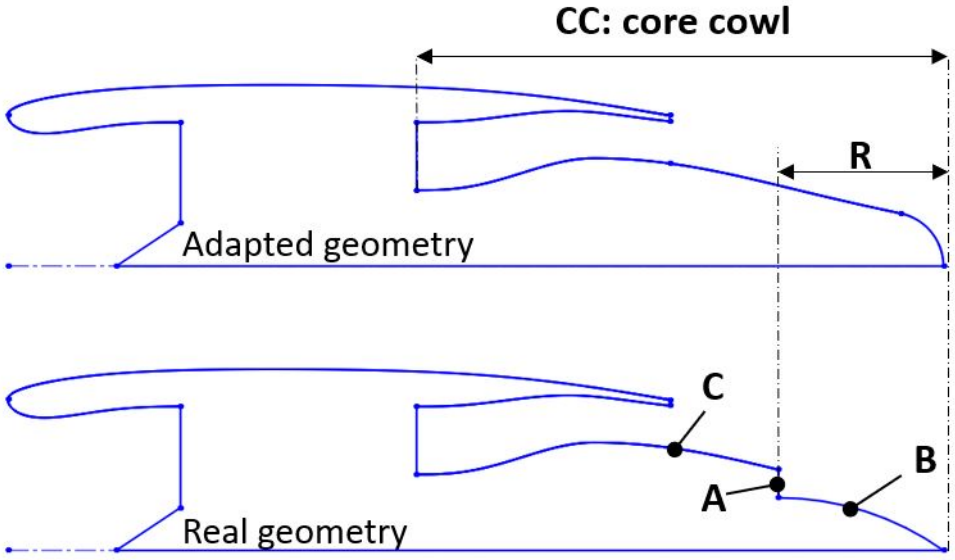

Figure 3.4: Difference between real and adapted geometry

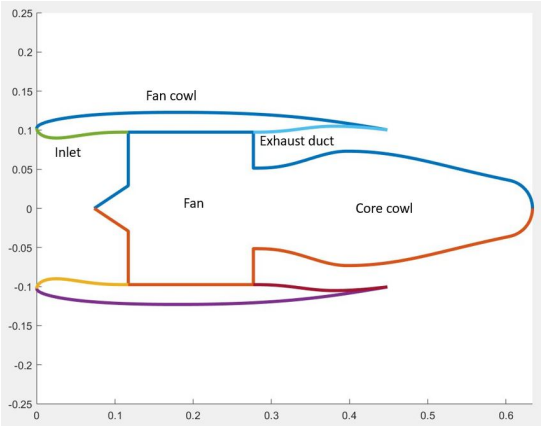

(a) Matlab Section view

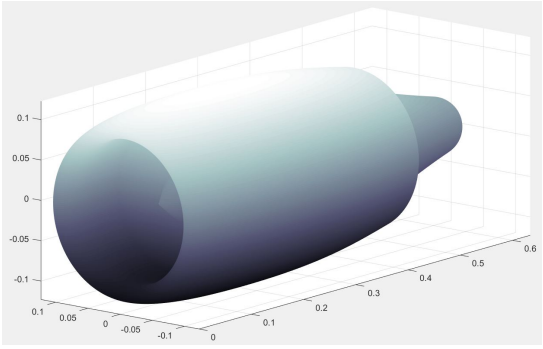

(b) Matlab 3D view

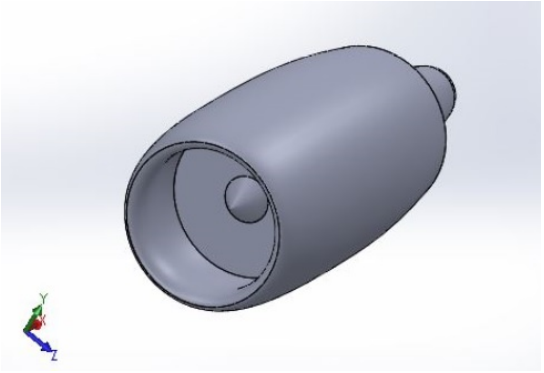

(c) One piece CAD model

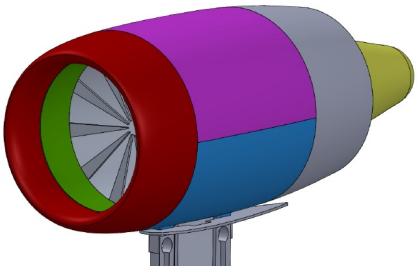

(d) Assembled model

Figure 3.5: Model geometry process

3.2 Rig setup

This section is the main part of this paper. It will explain in details the processes led to successfully complete the manufacturing and assembly of the model. In order to fulfill the main goal of this thesis, which is to perform nacelle drag measurements under different AoA and MFR, several questions had to be answered during the design procedure. They will be addressed in this section: How to provide variable MFR ? How to change AoA ? What should be the size of the model ? how to split the nacelle parts ? Which measurements should be performed? How to correct the results for wind tunnel wall interference ? What is the expected value of the measured drag? what material will be used to fabricate the nacelle parts ? and how to make the design flexible for future researches.

3.2.1 The fan

Let's start by describing the key feature that distinguishes this study from previous similar ones. The current experiment investigates the profile drag over a *powered nacelle* i.e. the nacelle has been implemented with a *core engine* which is the EDF. In doing so, MFR become controllable, and it has the potential to vary around the unity as described in section 2.1.3. A considerable number of flow-through nacelle

experiments can be found in the open literature [18, 19, 20], although it is hard to find direct drag measurements in powered nacelles. This probably happens due to the fact that it is not trivial task to split the thrust and drag forces in a conventional wind tunnel force balance. Apart from the easiness to control the MFR, powering a nacelle brings the benefit of making possible to assess the influence of the fan in the nacelle aerodynamics performance. This is particularly important for the case of short inlets, where the fan and the nacelle are closely coupled together.

The EDF which has been chosen for the experiments is a **Schübeler** DS-DIA-215 HST®, an efficient and powerful EDF with a 195mm fan diameter capable of achieving a static thrust of up to 250N at 15kW of power. The exhaust Speed Range vary between: 84-98 m/s and the overall efficiency is about: 78 % [21]. Further description is available in the Appendix A.
Since the nacelle size is correlated to the fan size, the criteria for selecting the fan was mainly its dimensions. In order to achieve a measurable profile drag, the nacelle outer area has to be considerably large which in turn requires large fan diameter. Hence, the largest EDF size in its category has been selected knowing that the size of the model shall not increase significantly the *blockage ratio*, which is defined as the ratio of the frontal area of the blockage to the cross-section area of the wind tunnel. Moreover, a large model facilitates to perform a diversity of measurements in the internal parts of the nacelle, such as positioning pressure probes and hot wire anemometers, or even installing pressure taps.

3.2.2 Nacelle parts

As previously stated the 3D model generated by MATLAB is converted into CAD format and then altered, split and assembled to satisfy the project goals. As it can be seen in figure 3.6 the one piece nacelle model has been split into several components. In this paragraph we will state briefly the requirements behind doing such splits and in the further sections the same is developed in details. Firstly, the purpose of splitting the lip (I) is to have the flexibility to conduct further researches with different geometries, such as an asymmetric lip or a shorter intake. Secondly, the inlet duct (II) and exhaust duct (V) have to be attached to the fan (EDF) which in turn is fastened to the main structure. However, the lip (I),center body (III & VI) and after-body (VI) have to remain floating for drag measurement purpose. Thirdly, it was chosen to separate CBUP (III), CBLP(VI) and the After-body(VI) to make the assembly process & sequence feasible and simple. The different parts shown in figure 3.6 are listed in the table below 3.2 which describes the material, name and acronym for each item.
Figure 3.7 shows a longitudinal cut of the nacelle mechanical assembly. Normally, the profile drag would be measured for the external surface of the nacelle cowl, between points (A)→(B) however it was necessary to perform a cut in the inlet duct, for the reasons listed in section 3.2.2.1. Therefore, the drag is measured from point (A')→(B). The components (I),(III),(VI) and (IV) are connected together as follows: (I) is circumferentially bolted to the front of parts III and IV at the point D axial location. Part VI is also bolted to the rear of parts III and IV, but at the point

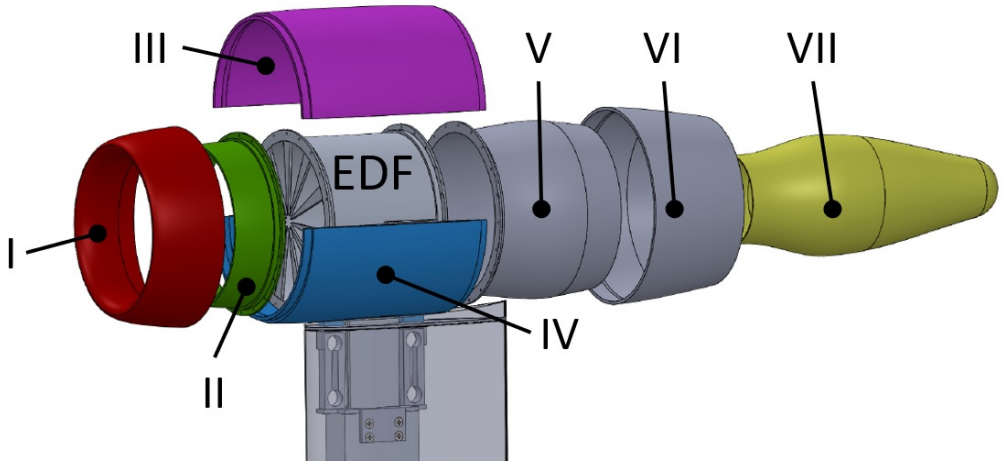

Figure 3.6: Exploded view of the modelled nacelle

item number	nommenclature	acronym	material
I	Lip	-	APL
II	Inlet duct	-	APL
III	Center body - Upper part	CBUP	Aluminium
VI	Center body - Lower part	CBLP	Aluminium
V	Exhaust duct	-	Aluminium
VI	After-body	-	Aluminium
VII	Core cowl	CC	APL

Table 3.2: Nacelle parts

E axial location. On the other hand, (III) and (IV) are connected laterally as it can be seen more clearly in figure 3.6. This set of components (I),(III),(VI) and (IV) (hereafter called: *floating set*) is completely separated from the other parts (II) and (V), by means of a circumferentially axial gap at points (A') and circumferentially radial gap at point (B). Both gaps are designed to be 2mm. Furthermore, the described floating set rests on the two load cells at points (C) allowing these to measure the captured profile drag between (A')→(B). Furthermore, to assure axial freedom of movement for the floating set, a 1mm gap has been provided at the location of horizontal plane (P). The two loading cells are attached and fixed to the structure by means of mean of a customised support, fabricated from a U shape aluminum profile.
Whilst the floating set is kept free to move, the components (II),(V) and (VII) are attached to the (EDF) which, in turn, fastened to the main structure denoted by the (Structure) in figure 3.7. This (Structure) does not have the freedom to move axially i.e. in the flow direction, instead it has the capability to rotate employing a rotary table and hence it provides different (AoA). The (fairing) in the shape of NACA0024 profile plays the role to cover the support and makes the whole structure more aerodynamically.

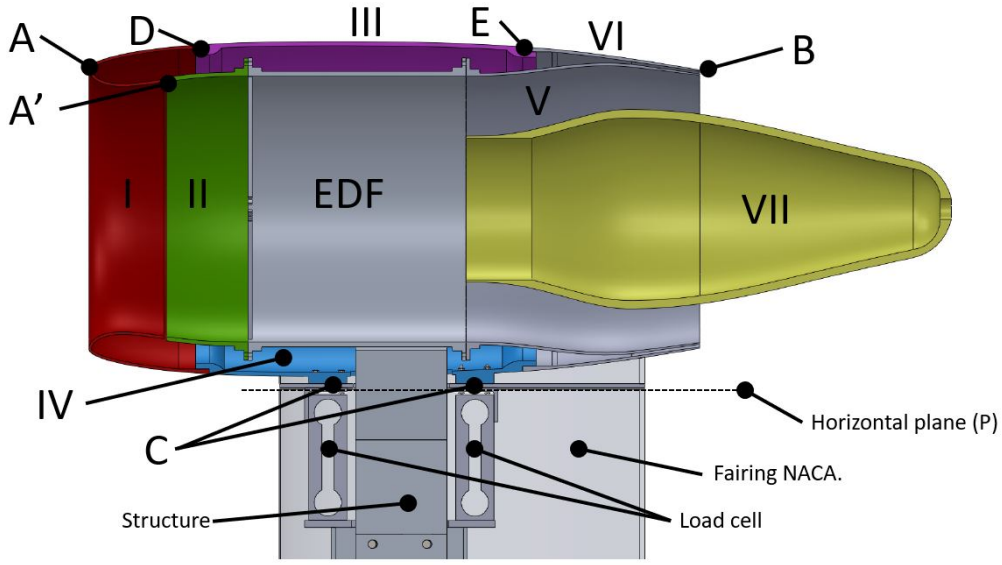

Figure 3.7: Longitudinal section details

3.2.2.1 The lip (I)

Besides the need of having replaceable lip for further researches (with different geometries) the baseline followed to crop the lip was the stagnation points locations, since the static pressure is high in this region, what could lead to a considerable amount of flow passing through the gap. As it can be seen in figure 2.6 the stagnation points have different positions around the front of the nacelle as a depending on the flight conditions and their corresponding MFR. The intent was to avoid a cut in the zone swept by the stagnation points. Moreover, it is known that the flow accelerates in the region between the inlet highlight and its throat, what results in a low pressure zone[22]. A gap in this region would cause considerable air suction inside the nacelle. In order minimise the effects of these gaps in the flow, a 2D axisymmetric CFD simulation was performed. A very fine mesh of about 700000 elements was generated using ANSYS ICEM. The y^+ was kept around 0.1 to guarantee a good near wall resolution and solve the viscous sub-layer.

The CFD solver @ANSYS FLUENT V18.2 was used for performing the simulation, which was carried out using the Reynolds-Averaged Navier-Stokes (RANS) equations, by applying the pressure-based solver together with the $k-w$ SST turbulence model. The pressure-velocity coupled scheme was selected jointly with second-order interpolations adopted for both the convection and diffusive terms. Air was modelled as an ideal gas and viscosity was calculated using Sutherland's law, with the three coefficient equation. The boundary conditions were defined as shown in figure 3.8. A rectangular farfield, with pressure farfield boundary conditions, was placed around the nacelle. The fan inlet was set to be a pressure outlet with target mass flow rate and the fan outlet is carries mass flow inlet boundary conditions. The boundary conditions were defined to roughly match the expected wind tunnel conditions, as follows:

- Fan inlet static pressure: 95925.63 Pa

- Fan inlet total temperature 289.317 K
- Mass flow rate 3.1356 kg/s
- Fan outlet static pressure:
- Fan outlet total temperature: 304.4282 K
- Farfield Mach number: 0.147
- Ambient pressure: 101.18 Kpa
- Ambient Temperature: 288 K.

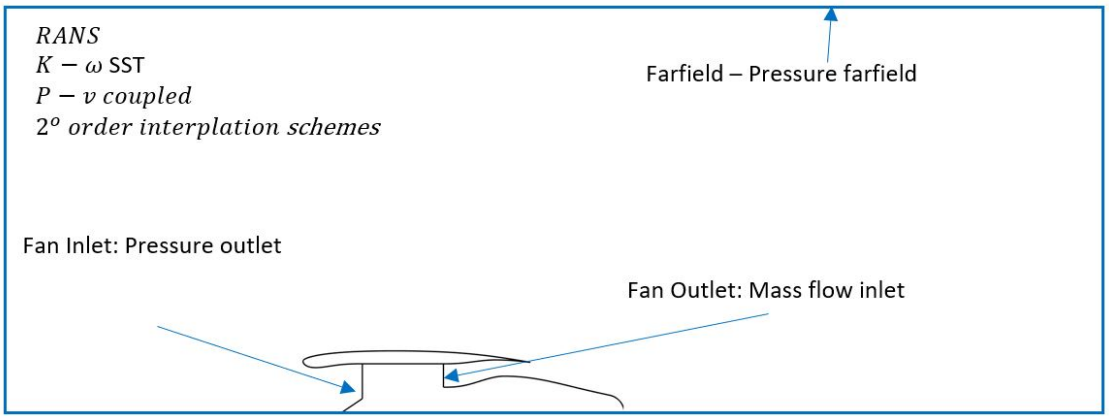

Figure 3.8: CFD setup

The results are presented in figure 3.9 where it can be seen that the said suction zone extends up to 0.055(m) from the front inlet. Hence it has been decided to perform the cut just after this distance which corresponds at point (A').
However, the cut in the fan cowl which demarcates the lip (I) was performed at 20% of the total nacelle length. This value was chosen so that a drooped lip geometry could be generated without altering the symmetry of the nacelle centerbody and afterbody parts. In other words the cowl curve cut at point (D) has a geometrical consideration conversely to the inlet curve cut which has aerodynamic criteria.
Thereupon, the split took place at points (A') and (D) (figure 3.7) which demarcate the lip (I). This leads, as well, to outline the inlet duct (II) after ensuring the 2mm gap. Besides that, the first limit defining (III) has been set at point (D). The technical drawing for the lip is shown in figure B.2 of appendix B.

3.2.2.2 The inlet duct (II)

As described in the previous section the inlet duct has been defined once the lip dimensions are determined. (II) is positioned between the (EDF) face and the gap at point (A'). In fact (II) is attached to (EDF) by means of circular flanges which have been 3D printed and glued to the (EDF) external face. The technical drawing for the inlet duct is shown in figure B.3 of appendix B.

3.2.2.3 The centerbody (III) & (IV)

The centerbody comprises the two components (III) and (IV) which are the upper part and lower part respectively. Their first axial limit at point (D) was defined

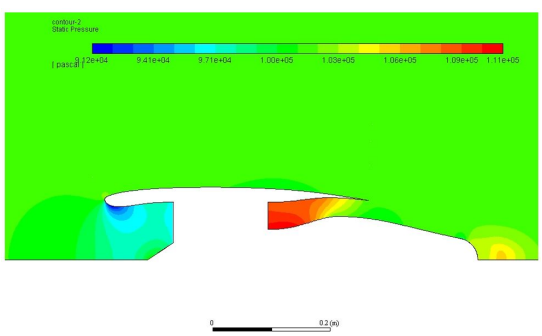

(a) Static pressure contour

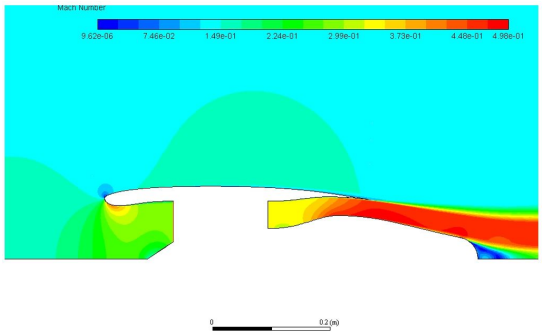

(b) Mach number contour

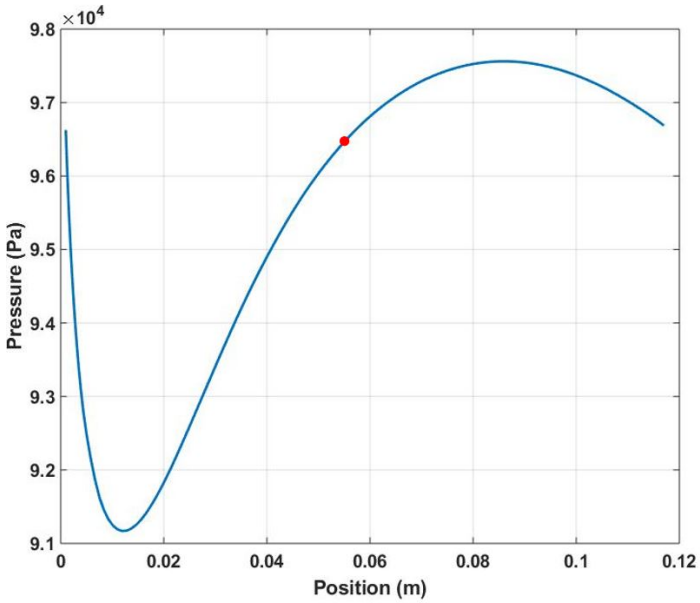

(c) Inlet pressure distribution

Figure 3.9: CFD results

earlier by the lip design however their second axial limit at point (E) is governed by the location of the load cells particularly the rear one. Thus, it can be seen how the circumferential cut is performed just after the location of posterior load cell at point (C). This makes possible to fasten the two load cells to the same components (IV) of the floating set rather than having each load cell fastened to different parts (e.g. IV and VI). Another reason for not having parts VI merged with III and IV is making the assembly feasible i.e. it would not be possible to place the fan and the fork inside the nacelle if those parts are not split from each other. In the same context i.e. to ease the assembly and make the alignment more flexible, the two parts (III) and (IV) were laterally split and provided with groove and bump connection shown in figure 3.10. The technical drawing for the centerbody is shown in figures B.4 and B.5 of appendix B.

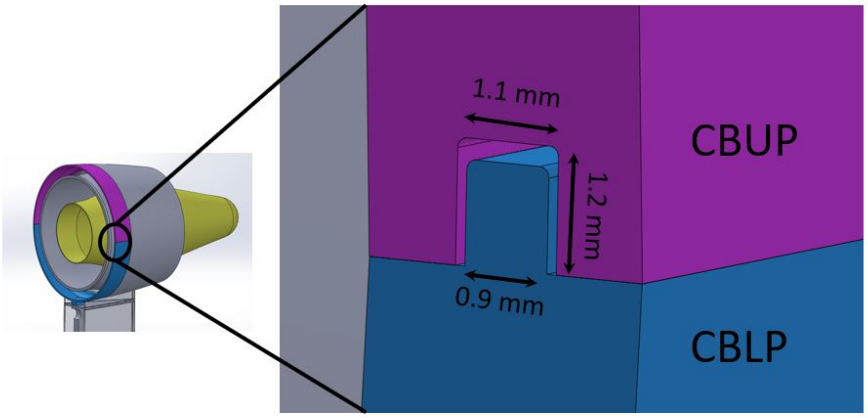

Figure 3.10: CBLP and CBUP lateral connection detail

3.2.2.4 The exhaust duct (V)

This part is extended from the (EDF) rear face till the trailing edge at point (B). Comparing the two figures 3.5a and 3.7 it can be noticed that (V) has never been split. Similarly to (II) this part is attached to the (EDF)by means of a flange which is glued to the EDF external surface. The technical drawing for the exhaust duct is shown in figure B.7 of appendix B.

3.2.2.5 The after body (VI)

Figure 3.7 shows that the after body (VI) is extended from the point (E) till the trailing edge (B). The circumferential cut at point (B) requires a radial gap which is designed to be 2mm, adding the thickness of (VI)(1mm) and (V)(1mm) makes the trailing edge height of 4mm. At the early design stage, there were two options to reduce this height and accordingly reduce the risk of flow separation at the trailing edge. Although these options could have had positive effect in the subject of preventing separation, they were problematic in the context of measuring the drag

- Option 1: perform the cut at point (B') instead of (B) as shown in figure 3.11 and hence the exhaust duct (V) would have extended from the (EDF) rear face till (B') giving the chance to reduce the trailing edge height. However, doing this would have omitted, from the measurement, the drag that occurs over the surface between (B') and (B) because (V) is attached to the (EDF) and not to the floating set.
- Option 2: perform the cut at point (B"), this would have the same positive effect as option 1. However, in this option the drag measurement would have grabbed pressure forces applied on the surface between (B") and (B). This due to the fan flow passing through the exhaust duct. As a consequence the drag measurement would have been wrong.

In conclusion it has been decided to turn down theses options and perform the cut at the trailing edge (B) as presented in figure 3.7. The technical drawing for the after body is shown in figure B.6 of appendix B.

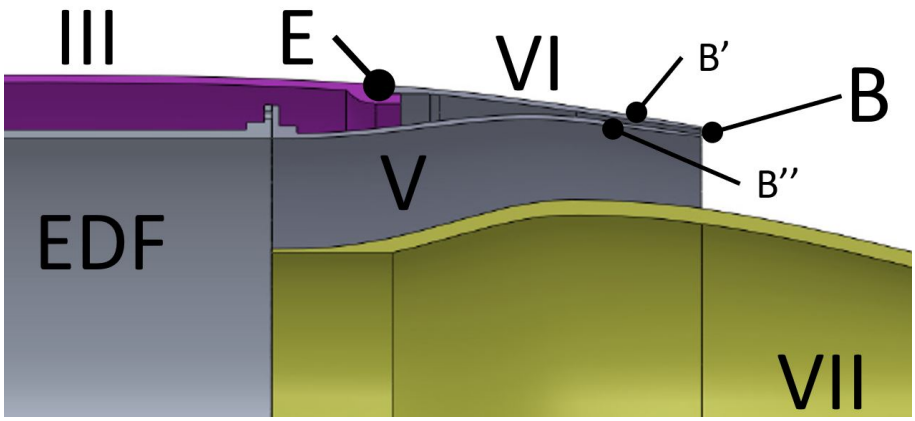

Figure 3.11: After body cutting options

3.2.2.6 The core cowl (VII)

It is worth noting that, all the components were designed in SOLIDWORKS as follows: the curves generated by the MATLAB code shown in 3.5a are **preserved** externally (i.e. where the curves are in contact with the flow streamlines) and extruded internally. While this concept is applicable to the following parts (I,II,III,IV,V,VI) it has some limitation towards the part (VII). The core cowl curve is *conserved* externally and extruded internally, this is feasible at the rear pointed end of (VII). However, a built-in plug is equipped at the EDF, what makes necessary to perform a cylindrical cut at the front part of the core cowl, so that it could be mounted around the existing plug. For reference see figure 3.7 at points (K), and figure 3.12. Likewise the built-in plug was provided with a hole at its rear end, the same was adapted to (VII). This hole contributes to the ventilation of the fan electric motor. The technical drawing for the core cowl is shown in figure B.8 of appendix B.

Figure 3.12: Fan existing plug and core cowl

3.2.3 Structure parts

The design of the structural system had many challenges in order to fulfil the rig requirements. Space limitation was the main difficulty. The structure has to carry safely the thrust (approx. 250N) generated by the EDF. The deflections resulting from such load must be minimal to avoid measurement disturbance. Additionally,

the structure should have enough stifness to mitigate and absorb the vibrations that might occur during the tests. The whole structure should be able to rotate for the drag measurements at positive AoA.

NB: The roman numbers (I,II..etc) utilised in this section 3.2.3 denote for the **structure** components (figure 3.13b). Meanwhile, in the previous section 3.2.2, they indicate the **nacelle** parts.

The fork (I) has been designed in half circular shape of 5mm thickness. Its diameter matches with the fan diameter. Parts (II) and (III) denote the right bracket and left brackets respectively, those were provided to assure certain distance between the nacelle bottom part and the aluminium duct. This distance was required to fit the two load cells (VI) and (VII). It is worth noting that only the right bracket (II) is attached to the fork, then the left bracket (III) is attached to (II). All these three attachments are provided by the mean of four bolts sets. This solution was necessary for enabling (II) and (III) to fit in a 5cm width aluminium duct (V). This width was a crucial limitation in order to provide a *standard NACA* profile for the fairing, this topic is more developed in section 3.2.5. Before proceeding further it is necessary to highlight that the (EDF) is fastened to the fork by means of two lugs diametrically opposite as shown in figure 3.13a. A custom part (IV) has been designed to receive the two load cells and in the same time (IV) had to fit externally to the aluminium duct. This part (IV) has a specific opening enabling the two brackets to be inserted in (V) from one side, and allow the power cables to be routed from the (EDF) downward in (V). Finally, the structure component (V) is fixed at its bottom end to a rotary table which enables the whole assembly to rotate for a certain desired angle, and therefore provides an (AoA) relative to the wind tunnel flow stream, as shown in figure B.1.

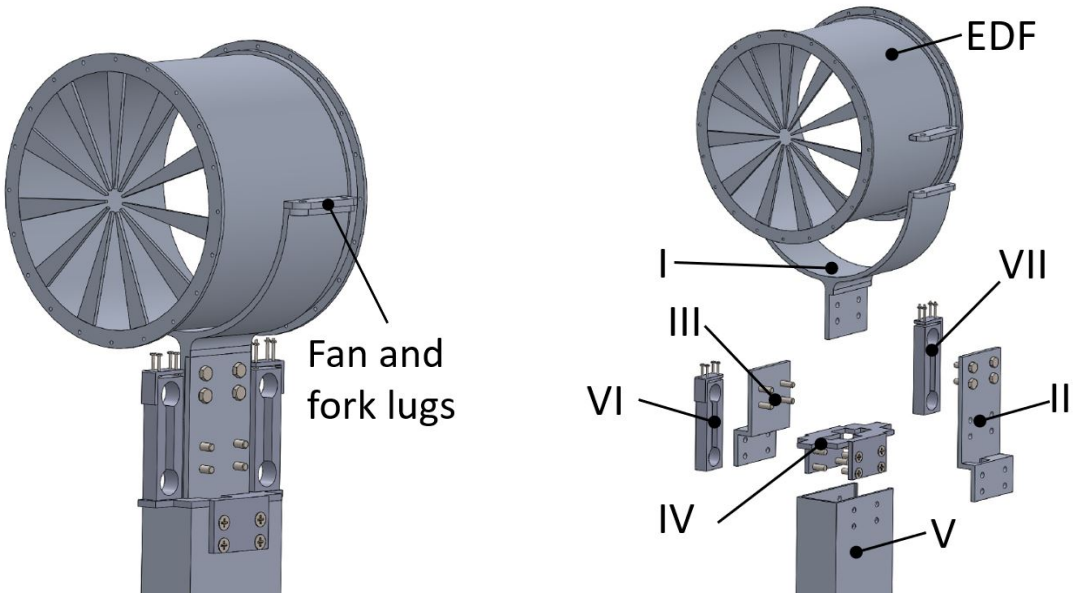

(a) Assembled structure **(b)** Structure: Exploded view

Figure 3.13: Structure components

item number	nommenclature	Drawing
I	Fork	B.12
II	Right bracket	B.13
III	Left bracket	B.14
IV	Load cell support	B.15
V	Aluminium duct	B.16
VI	Front load cell	A.5
VII	Posterior load cell	A.5

Table 3.3: structure parts

After designing the structure system, a static study has been conducted using the SOLIDWORKS static simulation feature. This study had the aim to verify the deflections occurring at the most critical parts. It was intended to be sure that minimum deflection is occurring in the load direction and have enough safety margin from the material yield strength. Significant deflection would have lead to incorrect measure of drag. The results are shown in figure 3.14 where it can be seen that the maximum displacement in Z direction is 0.26mm and it takes place at the point where the fork (I) and the (EDF) are fastened to each other. Figure 3.14c shows the total displacement which is equal to the shift in Z direction, the maximum value of displacement was considered to be acceptable for the current experiments. This was foreseen since the vector applied load is parallel to the Z direction. It is noteworthy that an iterative process has been followed i.e. we have started designing the parts (I,II,III and V) with less thickness (2mm) and continuously increasing it until it reaches (5mm) so we obtained this acceptable displacement. The simulation has been set assuming the lower part of the Aluminium tube (V) is a *fixed support* . At that location it is fastened to the rotary table as shown in figure C.1.

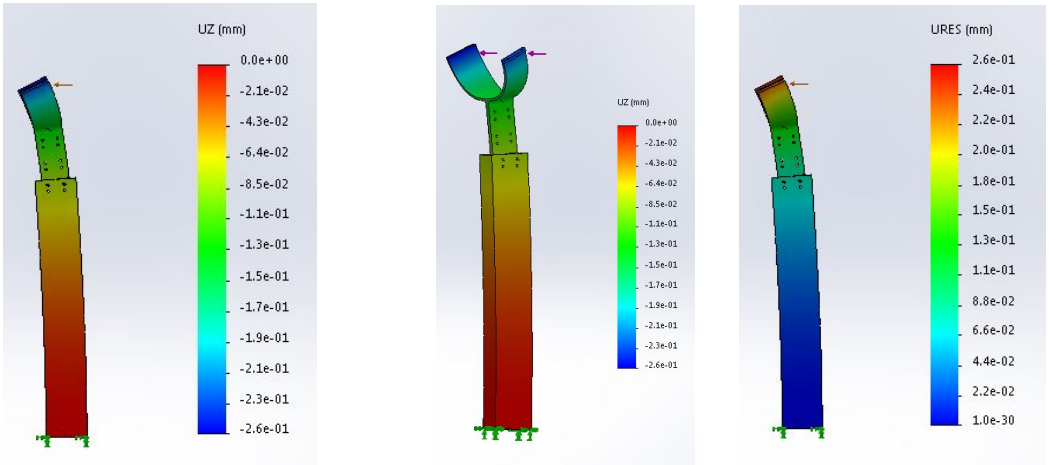

(a) Sectional view: Z displacement

(b) 3D view: Z displacement

(c) Sectional view: total displacement

Figure 3.14: Structure displacement due to EDF propulsive force (250 N)

3.2.4 Data acquisition process

An illustration for the data acquisition process used in this experiment is shown in figure 3.15. Two DAQ devices (NI 9237) and (USB-6210) have been used: the first is to collect the data from the load cell measurements and the second is integrated with the power control network. Both are shown in figures 3.18 and 3.19 respectively. Each DAQ device comprises three key components: the signal conditioning circuitry, analog-to-digital converter (ADC), and a computer bus [23] .

- Signal conditioning circuitry: Output signals from load cell could be noisy or difficult to measure it. Signal conditioning circuitry makes this signal adequate to be received by an ADC. This circuitry comprises of filtering, isolation, amplification, and attenuation.
- Analog-to-digital converter (ADC): is a ship that converts the analog signal to digital before being processed by digital equipment. In fact, the analog signal is continuously changing over the time so the ADC takes a periodic samples of this signal at predefined time rate. These samples are sent to a computer through a computer bus.
- Computer bus: is defined as the communication interface between DAQ and computer. DAQ devices are implemented on wide range of computer buses such as USB, PCI, PCI Express, and Ethernet.Lately, DAQ devices have been equipped for wireless communication.

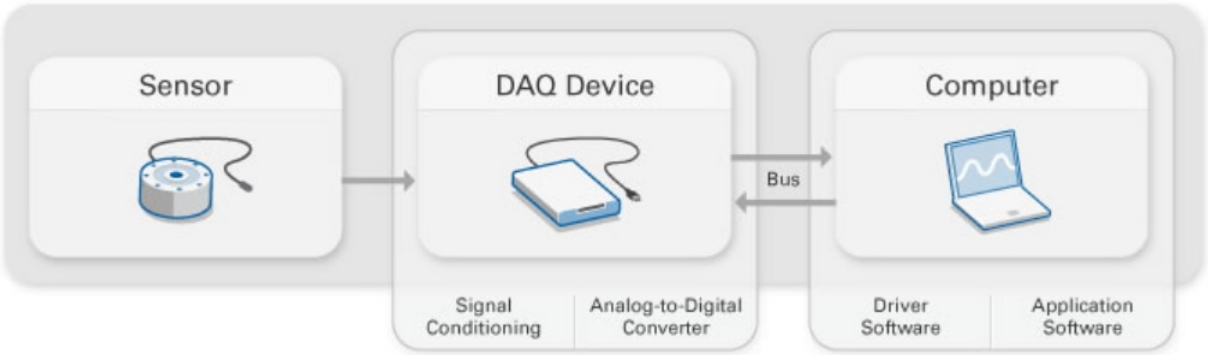

Figure 3.15: Data Acquisition system functionality

3.2.5 Fairing

It has been decided, from the early start of the design process, to provide a fairing for the support in order to minimise as much as possible the interference effects between the aluminium tube and the nacelle body. In that context, we had the objective to get rid from any potential separation occurring at the level of the fairing when the angle of attack is employed. Hence, it was decided to use a *symmetrical* 4-digit NACA series airfoil, which has very good stall characteristics, to build a constant cross section fairing. [24]. The assembly required a relatively thick NACA profile to enable it covering the aluminum duct. This subject is linked to the limitation mentioned in the previous section 3.2.3 about the width of aluminium duct. In

fact, it was more practical to select a wider aluminium profile to ease the mounting procedure of the structural parts. However, the widest profile found in [25] was NACA 0024 airfoil, max thickness 24% at 30% chord, max camber 0% at 0% chord (0% because of the symmetry). While designing a NACA profile it is true that the longer the chord the thicker is the airfoil, why didn't we adopt such procedure ? the answer is revealed in figure 3.16a which is the bottom view of the model. The distance d constituted the main driving parameter in the course of selecting the fairing profile and beforehand the aluminium tube. The objective was to increase this distance as much as possible to reduce the effects of the potential flow separation that might occurs at the fairing trailing edge. Such separation would definitely have negative effects on the drag measurement. On top of that, maximising this distance means reducing the fairing wetted area which has a positive impacts on reducing both the fairing drag and the interference drag in the fan cowl. Hence, a small part of the fairing is attached to the nacelle body, this component is called *fairing upper part*. Coming back to the design of NACA, a MATLAB code has been prepared employing the equation mentioned in [24] to generate the profile shown in figure 3.16b. It is important to highlight that the camber line and chord line were coinciding because of the symmetry hence the camber line equation has been disregarded and only the distribution equation has been utilised in the code. Once again, an iterative process has been followed (by changing the chord length) to come up with a result that a *standard* profile with 270mm chord would be able to cover the aluminium tube (shown in red in figure 3.16b). The technical drawing of the fairing is shown in figure B.9. Itt can noticed that the total chord length is 276mm instead of 270mm as generated in MATLAB. This is due to the external extrusion of (3mm) applied on the fairing.

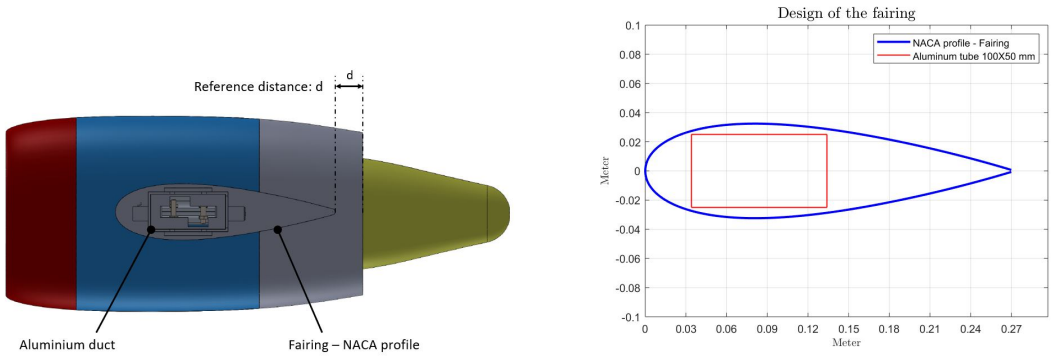

(a) Model bottom view **(b)** Matlab output

Figure 3.16: Fairing design

The closure between the fairing and the nacelle body is an important detail. At the vicinity of the nacelle CBLP the fairing has been cut to constitute two parts: the lower part denoted by *fairing* and the upper part called *fairing upper part*. The two parts have been separated by a gap of 1mm and a plate which has the shape of NACA profile called hereafter "*NACA plate*". The objective was to minimise as much as possible the *fairing upper part* since it is attached to the nacelle body and therefore the drag force read by the load cells will include the drag of the

fairing upper part. This part is shown in the technical B.10. This component, the fairing upper part, was designed and sliced based on the lower part faring and as per nacelle 3D curve, this has been done using SOLIDWORKS feature *cavity*. The above mentioned *NACA plate*, shown in technical drawing B.11, has been put in service to provide more rigidity for the load cells, reducing the probability of damage due to vibration or side loads, and decreasing their potential of twisting during high AoA by increasing the stiffness of the system. The fairing and its upper part were 3D printed using PLA material whereas the NACA plate is made of aluminium. Finally we have to point out that the NACA plate is fastened from its lower face to the load cells and its upper face to the nacelle CBLP as illustrated in figure 3.17

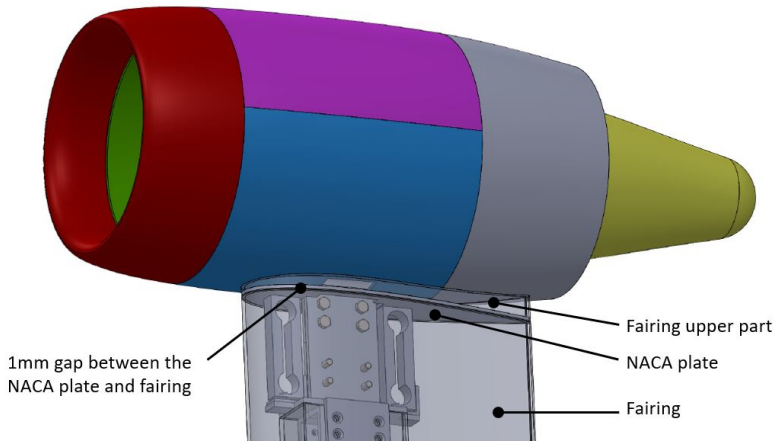

Figure 3.17: Fairing components

3.2.6 Load cells

This section must be read in accordance with section 4.1.
Prior to selection of load cells, an analytic calculation has been made to evaluate the skin friction drag over the nacelle cowl. The flat-plate theory has been employed in order to estimate the magnitude of drag to be obtained in the experiments. Although there is no exact theory for turbulent flat-plate flow, the most widely accepted result is simply an integral analysis [3]. The following inputs have been used.

- U= 60 m/s (wind tunnel air flow velocity)
- L= 0.448 m (nacelle length)
- T_0=273 K
- S_{air} = 110.4 Sutherland constant
- μ_0=1.71 E-5 kg/(m.s) Dynamic viscosity
- T=288 K (wind tunnel test section temperature)
- $S_{nacelle} = 0.367m^2$ (nacelle area)
- $\rho = 1.2kg/m^3$ (air density - assuming incompressible flow)

Using Sutherland law

$$\frac{\mu}{\mu_0} \approx (\frac{T}{T_0})^{\frac{3}{2}} \left(\frac{T_0 + S}{T + S}\right) \tag{3.18}$$

μ = 1.783 E-5 kg/(m.s). Reynolds number Re_L is calculated as follow:

$$Re_L = \frac{\rho U L}{\mu} \tag{3.19}$$

Re_L=1.809 E6. It is higher than 10^6 thus the flow is turbulent at the fan cowl trailing edge. The drag coefficient for fully turbulent boundary layer $C_{f_{turb}}$ is computed using equation 3.20 [6]:

$$C_{f_{turb}} = \frac{0.455}{(log_{10}(R_e))^{2.58}} \tag{3.20}$$

$C_{f_{turb}}$=4.02E-3 Hence the skin friction drag acting on the outer surface of the nacelle is obtained by employing the equation 3.21[3]:

$$D_f = \frac{1}{2}\rho U^2 C_{f_{turb}} S_{nacelle} \tag{3.21}$$

Yielding

$$\boxed{D_f = 3.18N}$$

Therefore, the rated capacity of the load cells was selected to be 0.3 kg. In doing so, it is ensured that the measured drag will be between the safe overload limits of the transducers. Besides that, as precociously stated, two load cells were selected, instead of one, so that they could act as a stable support for the floating set. The instruments have been purchased from **VETEK** model number 108AA [26]. More information about these load cells can be found in their technical drawings and data sheet see A.5. In compliance with section 2.2.1 the data cables from the load cells are connected to a DQA device model number NI 9237 made by **National instruments** detailed information can be found in [27]. The DAQ is then connected to the computer wherein the software "Labview" is employed to visualise and store the data received from the load cells. A detailed single line diagram is presented in figure 3.18 shows the data acquisition from the load cells

3.2.7 Wind tunnel

The wind tunnel disposal at this experiment is Chalmers L2 Wind-tunnel which have the following characteristics [28]

- Closed loop.
- Octagonal cross section area $2.08M^2$.
- Cross section dimensions 3M 1.8M 1.25M (L.W.H).
- Maximum wind speed is 60 m/s.
- Contraction ratio 5.86:1

The main fan is $2M$ diameter, it has 6 blades and it is powered by a motor of $170KW$. A set of stators, used for supporting the motor and for cooling purpose, have been installed downstream of the main fan. A cooling fan of $50KW$ is used to inject the fresh air. Before being injected in the main stream, the inlet flow

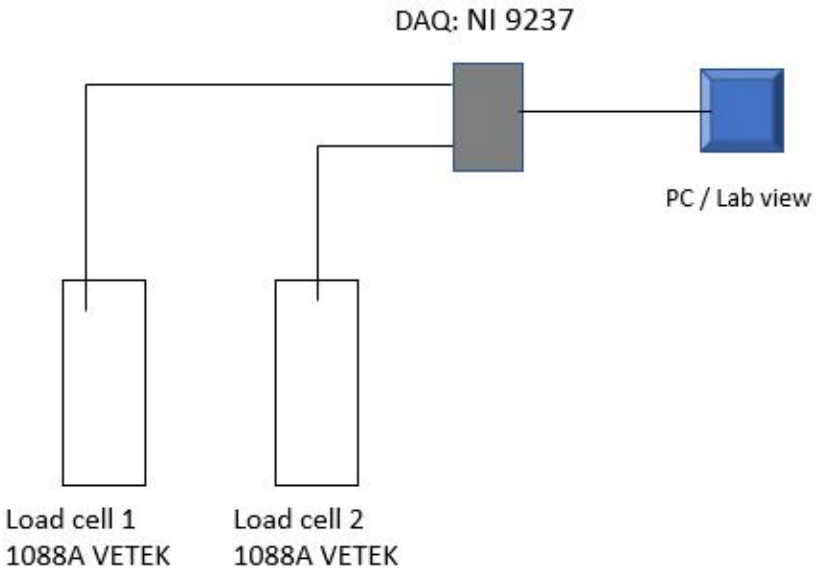

Figure 3.18: load cells data acquisition

temperature is controlled by an intercooler. The temperature is maintained within one degree difference. A breather slot of 20 mm has been fixed, at the posterior end of the test section, to regulate the pressure. The tunnel's fan mixture levels and wind speeds are regulated by the user through Labview 2012. The nacelle centre was mounted in the centre in the X,Z direction. The Y distance from the floor was 625mm.

3.2.8 Electric power supply

The power provided to the EDF was supplied by using Three Sealed Lead-Acid Batteries in series. Each unit has 6 cells, $12V$ and capacity of $100Ah$. More data are shown in A.6 and A.7. Power cable routing is made as follow: from the cathode and anode two cables 2x25mm^2 are connected to the power controller (TMM 40063-3 for Multicopters X2-SERIES [29]). Upstream of the power controller the cable at the anode side passes through an electrical switch for safety purposes. Downstream the controller a set of three cables 3x16mm^2 are feeding the EDF motor. At the controller level a data cable is connecting the controller to the data acquisition device DAQ and further to the computer via USB cable wherein The fan rotational speed is then controlled through Labview. A current transducer or hall sensor HAS 100-S [30] has been installed at one of the power feeder entering the EDF and it is connected to the DAQ. The input voltage signal frequency is used to get the RPM of the EDF. The DAQ device used in this network is a multi-function digital input/output device its model number: USB-6210 made by **National Instruments**. More data about this device can be found in [31].
The single line diagram shown in figure 3.19 illustrates the electrical power connections as well as the data acquisition set up.

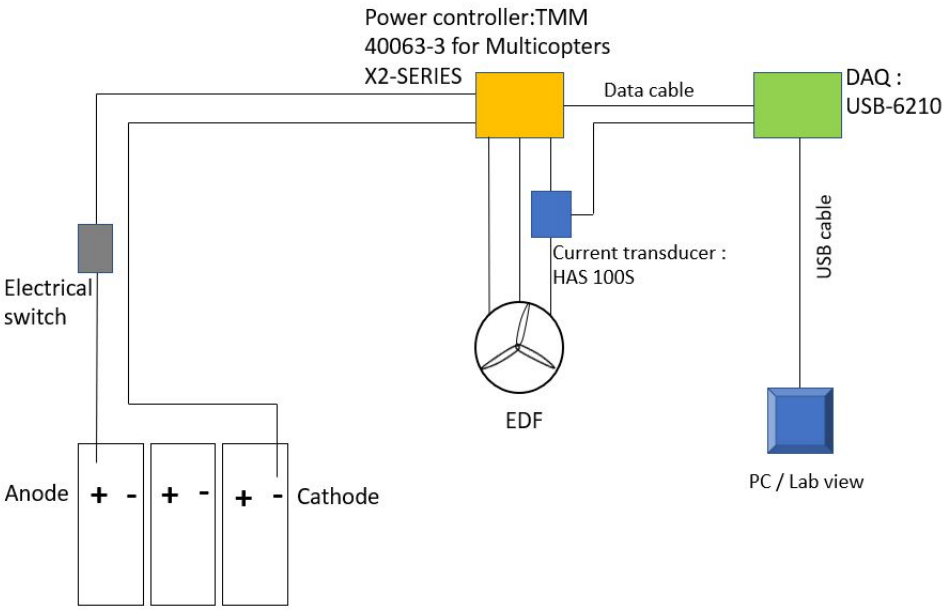

Figure 3.19: Power distribution and control

3.2.9 3D printing and surface preparation

The 3D printer used in this reasearch is **Modix Big60 v2** which has the capacity to print up to 600 mm object. The large size parts such as the fairing have been printed in several sub-parts and then glued together. The slicing software employed was *cura* and the filament material was PLA. The parts presented acceptable surface roughness as printed, however, a special surface treatment was applied to get rid of the wavy surface resulting from 3D printer. The treatment process consists of polishing the part with 240-grit sandpaper then applying "P360 2K HS" which is a filling primer. After the primer is completely dry, the surface is sanded with 323-grit sand paper until it achieves a surface smooth enough to proceed with the experiments.

3.2.10 Sequence of installation

This subsection describes the sequence and lists the steps recommended for proper installation of the model.

1. Fix the aluminium tube (bottom end) to a working desk/table.
2. Pull in the power and control cables through the aluminium tube.
3. Fasten the two brackets and the load cell supports to the aluminium tube top end. It is recommended that the load cells are pre-mounted to their supports.
4. Lay down the NACA plate on top of the load cells. Glue the fairing upper part to the NACA plate.
5. Insert the CBLP into the brackets and fasten it to the load cells.
6. Prepare the "sub-assembly = Inlet duct + (Fan+core cowl)+ Fork + exhaust duct"
7. Fasten the sub-assembly, by means of the fork, to the right bracket.

8. Connect the power and data cables.
9. Install the CBUP.
10. Insert the lip and fasten circumferential the screws to CBLP and CBUP.
11. Insert the after-body.
12. Dismantle the whole assembly from the working desk
13. Slide the fairing from the bottom side of the aluminium tube.
14. Axial and circumferential alignments are required for both gaps located at inlet duct and exhaust duct.

4

Results

4.1 Load cell upgrading and correction

The early tests performed on the model showed considerable vibration. Due to these vibration the measured loads were exceeding the rated capacities of the the two load cell (0.3 Kg) hence the load cells were upgraded to keep the measurements within the rated range. The new selected load cells are the same model, but with an improved rated capacity of 5 kg. Even though some accuracy was lost after the rated capacity was increased, the new load cells still have a good accuracy in the order of 0.1g. Moreover, the latter load cells are stiffer and contribute to reduce the assembly vibration. No adaptations in the original design were necessary, due to very similar dimensions between the former and the latter load cells.
Moreover, it was noticed that some residual stresses were acting on the load cells after the assembly process hence the feature "offset nulling", in LABVIEW, was used to reset the values to zero. It is worth noting, that the load cells have been fixed in such way their indicating arrows are in the same direction of the freestream velocity V_∞. If the force is in the direction of the indicating arrow, the output reading from the load cell is positive otherwise it is negative.

4.2 Pressure taps

Static pressure measurements were performed at the circumferential gap, near the fan face and just downstream of the fan outlet guide vanes. These data have been used in further steps to calculate the MFR. Figure 4.1 shows the location of the pressure taps. Note that these instruments reads the relative pressure, hence to get the absolute pressure, the ambient pressure is added to the measured value.

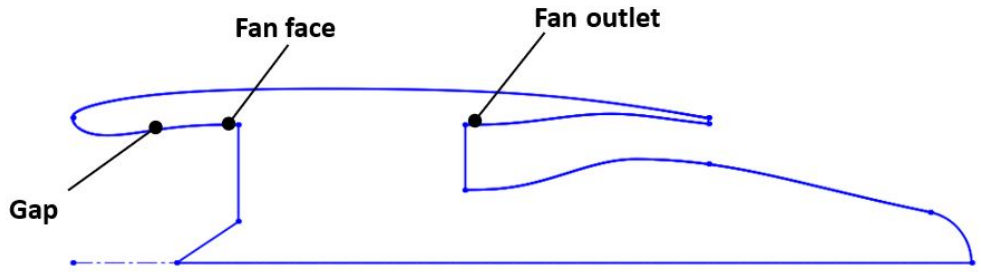

Figure 4.1: Pressure taps location

4.3 Test procedure and data processing

A LABVIEW code was written to acquire the measured data, as well as to provide an input signal do the electronic speed controller (ESC). Data from the load cells, pressure taps, wind tunnel manometer and hall sensor are processed, filtered, averaged and saved continuously in a text file. Each test process in different file, the file name was based on the test conditions i.e. AoA, percentage of maximum power demand for EDF and wind tunnel air velocity. The file nomenclature can be seen in second column in figure 4.8. The speed controller was programmed to continuously give input pulse signals to the fan, during specified periods. All the results presented in this thesis were collected using the same procedure:

1. The nacelle positioned at the desired angle of attack.
2. The wind tunnel speed is gradually increased from 0 to the desired value using steps of 5 m/s.
3. the fan speed was ramped up from zero to the desired speed throughout several steps and then ramped down to zero again. Once the fan had reached the aimed rotational speed, this was kept constant for 60 seconds, so that time was enough to go through all the fan transient response and gather enough data during its steady operation

The pulse signal to the EDF is a percentage of the total power available in the batteries. Therefore, the fan rotational speed can differ, for two different experiments, for the same input pulse signal. this difference will only be expressive when the batteries have a low state of charge. The data have been converted to excel and read by MATLAB wherein they have been filtered and averaged. The filter consists of excluding the readings during the ramp up and ramp down of the fan, since these are not relevant. Moreover, any value with exceeded three times the average of any measured quantity has been removed from the computation.

4.4 Wind tunnel mapping

A plan has been set to perform the tests and try to get results for the different analysis such as the effect of changing AoA, MFR and wind tunnel air velocity. The following tables show in blue dots the setup of the different tests. Figure 4.2 shows the wind tunnel mapping chart for an AoA equal to zero. The data was collected for wind tunnel speeds varying from 0 to 50, for fan input requests of 0.5 and 0.8. Figure 4.3 shows the wind tunnel mapping chart by varying the AoA from 5°to 20°while the wind tunnel air velocity changing between 10 and 50 m/s. The fan input power was fixed to 0.8 except for the points where two numbers are identified (e.g. 16,17 & 18,19), the test was conducted for fan input power 0.5 *and* 0.8. Actually, these tables were the primary plan since an additional set of experiments was conducted by fixing AoA to zero, wind tunnel air velocity to 40 m/s and fan input request changing between 0.4 and 1. This set of experiment is performed to evaluate the effects of changing MFR, on the measured forces. As it can be seen in figure 4.8 all the tests are listed.

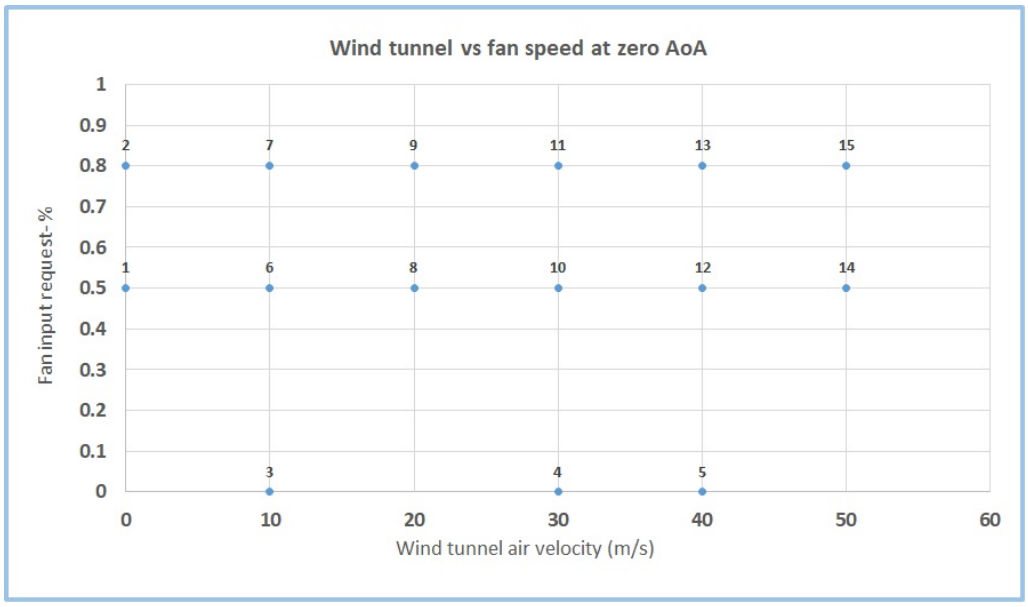

Figure 4.2: Wind tunnel mapping-table 1

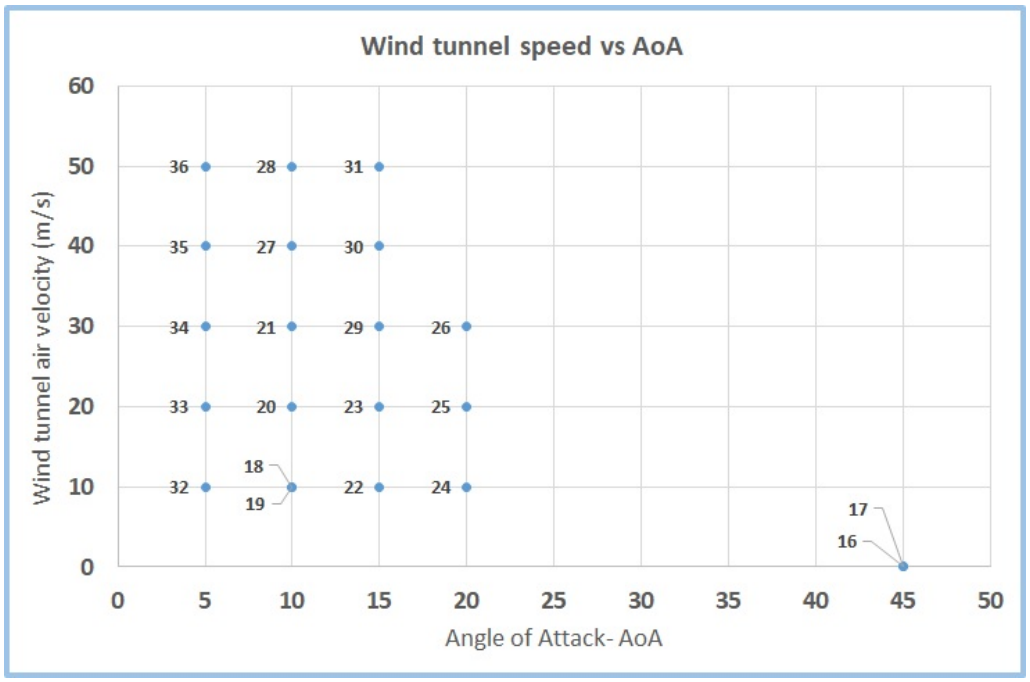

Figure 4.3: Wind tunnel mapping-table 2

4.5 Mass flow ratio calculation

Based on the definition of MFR in 2.5 we conducted the calculation referring to the figure 4.4 whereby we assumed the air is incompressible hence the density ρ remains constant between the two stations (∞) and (1) accordingly $\rho_\infty = \rho_1$. The continuity

equation or mass conservation law yields to:

$$\dot{m}_\infty = \dot{m}_1 \tag{4.1}$$

$$\rho_\infty V_\infty A_\infty = \rho_1 V_1 A_1 \tag{4.2}$$

$$\frac{A_\infty}{A_1} = \frac{V_1}{V_\infty} \tag{4.3}$$

Thus the MFR which denotes *mass flow ratio* turns out to be the inverse of corresponding velocities ratios

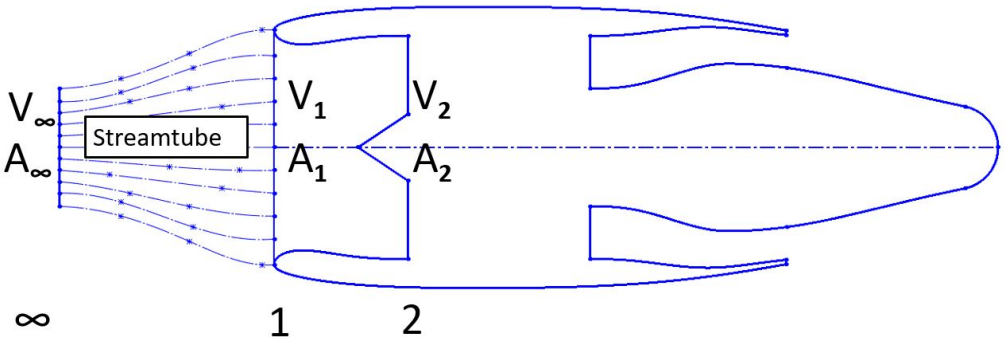

Figure 4.4: MFR calculation

The wind tunnel velocity represents V_∞. In order to calculate V_1 at the highlight area, V_2 at the fan face is calculated and mass flow conservation is employed between (1) and (2).
First we compute the total pressure P_{02} at the fan face by using the equation [1]

$$\frac{P_{02}}{P_\infty} = \left[1 + \eta_i \frac{V_\infty}{2c_p T_\infty}\right] \tag{4.4}$$

where η_i is the isentropic efficiency assumed to be equal to 0.99 for accounting the total pressure loss in the inlet duct. The air specific heat c_p=1005 j/KgK. The measured relative pressure at station (2) plus the ambient pressure yields to the static pressure (P_2). The latter combined with the total pressure P_{02} through the equation below [1] concludes (V_2)

$$\frac{P_{02}}{P_2} = \left(1 + \frac{\rho V_2^2}{2P_2} \times \frac{\lambda - 1}{\lambda}\right)^{\frac{\lambda}{\lambda - 1}} \tag{4.5}$$

Hence the velocity (V_2) is obtained at the fan face (2) and can be translated to (V_1), the velocity at station (1), by employing the mass conservation equation:

$$V_1 = \frac{A_2}{A_1} V_2 \tag{4.6}$$

The ratio $\frac{A_2}{A_1}$=0.9512

4.6 Observation of forward fan cowl force

During the preliminary tests while the rig has been mounted in the wind tunnel some interesting observations have been made concerning the drag measurement.These can be divided into two topics:

4.6.1 Wind tunnel on and fan off generates forward fan cowl force.

Under this setup, one might think that backward-force (i.e. force in the direction of V_∞) shall be measured. However the opposite was correct, i.e. a forward-force (force opposite to V_∞ direction) was detected. This can be seen in the first three rows in the table figure 4.8 wherein LC1+LC2 (6^{th}) columns is -0.023, -0.186 and -0.426. It is true that drag is acting on nacelle outer surface, however other factors could overcome this force and make the resulting measured force to be negative. The two main reasons are listed below with figures.

1. Pressure force acting in the internal surfaces of the nacelle cowl.
   It can be seen in figure 4.5, flow might enter the gap of 2mm and creates a pressure distributed force on the inner surface of the lip. The projected annular area (green colour) responding to such pressure forces is estimated to be 3.531E-3 m^2. As it can be seen in figure 4.5, two red lines parallel to the engine axis are drawn in the nacelle. The upper one is located in the radial position of the fan cowl trailing edge, whilst the lower one is placed in the end of the lip (just upstream of the gap). Integration of the pressure distributions above the upper line and below the lower line, would result in zero, for an axisymmetric nacelle, due to cancellation of the radial and axial components of force. Hence the area delimited between these two lines where the integration of the outward normal vector ($\hat{n}$) to the surface is equal to the annular projected area. The measured pressure at the gap is *relative pressure* hence the ambient pressure is added to obtain the *static pressure*. In fact, the pressure gradients create the surface pressure forces hence, ΔP should be the difference between the static pressure at the gap and the wind tunnel static pressure. The calculation has been made and presented in figure 4.6. It can be seen that the calculated pressure forces are of the same magnitude and pretty close to the measured forces (LC1+LC2). This justify the negative measured forces.

2. Forward force generated due to lip suction effect.
   Figure 3.9a which illustrates the pressure contour from the 2D CFD simulation can be simplified as shown in figure 4.7. The flow is accelerated in the inlet, between the highlight point and the throat hence, the static pressure decreases in that zone (represented by the red curve). However, the fan cowl is exposed to *almost* constant ambient pressure (represented by the green curve). The difference in pressure distribution or, pressure gradient, yields to forward force. This is a second reason contributing with the fact of reading a negative forces

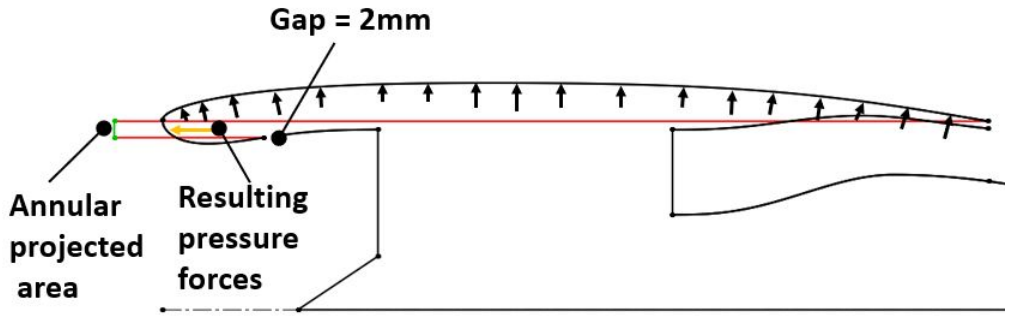

Figure 4.5: Internal pressure force illustration

S.n.	Set up	Fan RPM	LC1+LC2 (Kgf)	Wind Tunnel pressure (Pas)	Gap pressure (pas)	Annular projected area(m2)	Atmospheric pressure (Pas)	ΔP (pas)	Pressure force (Kgf)
1	AOA0_Fan0_Wind10	0	-0.023	101200	60.8	0.003531	101325	185.8	-0.066
2	AOA0_Fan0_Wind30	0	-0.186	101200	509.2	0.003531	101325	634.2	-0.224
3	AOA0_Fan0_Wind40	0	-0.426	101200	912.8	0.003531	101325	1037.8	-0.366

Figure 4.6: Internal pressure force calculation

under the setup of wind tunnel on and fan is off.

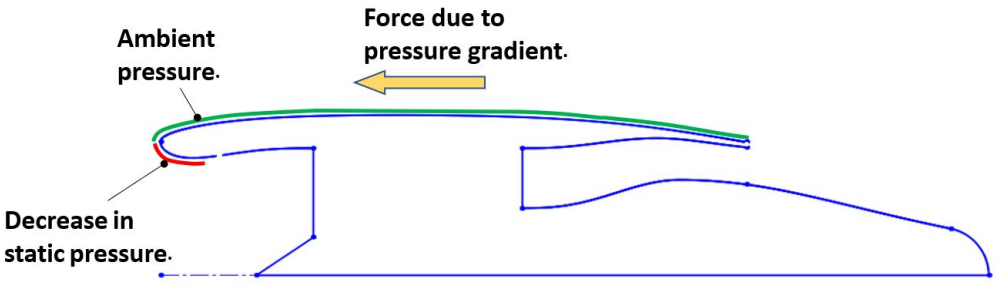

Figure 4.7: Lip suction effect - forward force

4.6.2 Forces are measured for the fan running at zero wind tunnel speed

The model was designed so that the fan cowl would not be directly mechanically attached to the EDF. Therefore, when the WT is turned off, the only measured forces are supposed to be dynamic loads transferred from the fan to the struts. However, some static loads were captured by the load cells. The output of this setup can be seen in the figure 4.8 row S.n 4 and 10. These two experiments have been set wind tunnel air velocity and AoA to zero with fan rotational speed to 50% and 80% respectively. The reading outputs from load cells (LC1+LC2) were -0.337 and -0.773 respectively. This has been interpreted as interference between fan parts and nacelle body. When the fan is on it generates forward force. In the same time if the

fan intervenes with any part of the nacelle body, this forward force is transferred to the nacelle body and subsequently to the load cells resulting in measured negative (or forward) force. The model has small gaps between the fan flanges and nacelle centrebody (approx. 1 mm) adding this, to the requirement of alignments leave the model in a sensitive status against gaps spacing. Furthermore, the power cables installed between the fan and nacelle body have been in high potential to create a bridge to convey the thrust force generated at the fan to the nacelle. On top of all there was no visual access to take any remedy action.

4.7 Measurements outputs

The following table shows the results obtained from the several tests. In total, 43 runs have been performed according to the procedure explained in section 4.3. Some physical quantity like the Reynolds number has been added to the the table by considering the nacelle chord length (448 mm) as characteristic length, kinematic viscosity and density are output data from the wind tunnel manometer. In the same time, some data have been omitted from the table because these quantities were constant for the different setup.

- Density $\rho = 1.2\, kg/m^3$
- Kinematic viscosity $\nu = 1.52\ E-05\, m^2/s$
- Wind tunnel temperature T=20.7 °C
- Wind tunnel pressure P=101,200 Pa

4.7.1 Measured forces vs AOA

Figure 4.9 shows how the measured forces change with varying the angle of attack at different wind tunnel air velocity. As it can be observed, the measured back force is increasing with the wind tunnel speed. Moreover, a pattern can be clearly observed for wind tunnel speeds from 10 to 40 m/s. The measured force increases up to some angle of attack and then starts to fall down again. This might be explained by two different phenomenon, happening in the upwind nacelle lip and cowl. As the AoA is increased, the static pressure is increased in the fan cowl (upwind), what contributes to the increase of the measured force. On the other hand, the higher the AoA, more downstream of the highlight the stagnation point is. Therefore, the flow streamlines need to accelerate in order to turn around the lip before entering the nacelle. This acceleration creates a high speed/low pressure zone in the upwind lip contributing to the decrease of the measured force. The results suggest that up to an AoA=10°, the increased pressure in the cowl is the predominant phenomenon. Otherwise, the high pressure in the fan cowl starts to be over-weighted by the lip suction effect for AoA higher than that.

S.n.	Set up	Fan RPM	LC1	LC2	LC1+LC2 (Kgf)	Power in demand	Wind Tunnel air speed	Wind tunnel Re	Fan face presssure (pas)	Gap pressure (pas)	Fan outlet pressure (pas)
1	AOA0_Fan0_Wind10	0	-0.007	-0.016	-0.023	0	9.83	2.91E+05	38.0	60.8	9.5
2	AOA0_Fan0_Wind30	0	-0.085	-0.101	-0.186	0	29.68	8.78E+05	356.8	509.2	70.7
3	AOA0_Fan0_Wind40	0	-0.199	-0.228	-0.426	0	39.88	1.18E+06	642.5	912.8	129.5
4	AOA0_Fan50_Wind0	5312	-0.193	-0.144	-0.337	50	2.56	7.56E+04	-236.7	-317.5	352.1
5	AOA0_Fan50_Wind10	5296	-0.014	-0.041	-0.055	50	10.45	3.09E+05	-177.7	-256.0	394.1
6	AOA0_Fan50_Wind20	5289	0.069	0.023	0.092	50	20.10	5.94E+05	-28.8	-100.6	484.7
7	AOA0_Fan50_Wind30	5283	0.114	0.033	0.147	50	30.02	8.88E+05	238.2	161.7	637.5
8	AOA0_Fan50_Wind40	5165	0.123	-0.009	0.113	50	40.16	1.19E+06	519.8	538.9	836.5
9	AOA0_Fan50_Wind50	5273	0.069	-0.107	-0.038	50	50.44	1.49E+06	874.8	1043.3	1072.1
10	AOA0_Fan80_Wind0	7942	-0.416	-0.357	-0.773	80	4.24	1.25E+05	-488.3	-712.4	821.2
11	AOA0_Fan80_Wind10	7906	-0.168	-0.190	-0.358	80	11.01	3.25E+05	-391.5	-628.7	857.5
12	AOA0_Fan80_Wind20	7871	0.033	-0.032	0.001	80	20.44	6.04E+05	-247.0	-480.9	947.6
13	AOA0_Fan80_Wind30	7871	0.148	0.045	0.193	80	30.30	8.96E+05	-54.0	-224.4	1119.7
14	AOA0_Fan80_Wind40	7806	0.233	0.052	0.285	80	40.36	1.19E+06	227.9	167.8	1336.0
15	AOA0_Fan80_Wind50	7803	0.250	0.030	0.280	80	50.64	1.50E+06	714.5	640.4	1631.2
16	wind10_A0A0_fan30	2880	0.120	-0.093	0.028	30	10.00	2.96E+05	-37.3	-35.9	134.5
17	wind40_A0A0_fan40	3958	0.131	-0.156	-0.025	40	40.00	1.18E+06	597.8	677.8	668.3
18	wind40_A0A0_fan50	5030	0.210	-0.094	0.116	50	39.99	1.18E+06	535.2	563.4	811.8
19	wind40_A0A0_fan60	5991	0.256	-0.054	0.203	60	40.06	1.18E+06	491.1	445.0	963.9
20	wind40_A0A0_fan70	6895	0.300	-0.020	0.280	70	40.13	1.19E+06	431.1	318.4	1129.2
21	wind40_A0A0_fan80	7557	0.325	0.000	0.326	80	40.20	1.19E+06	323.8	217.2	1266.1
22	wind40_A0A0_fan90	8287	0.344	0.018	0.361	90	40.22	1.19E+06	92.2	84.9	1431.2
23	wind40_A0A0_fan100	8727	0.352	0.024	0.376	100	40.27	1.19E+06	48.3	4.6	1538.8
24	AOA5_Fan80_Wind10	7978	-0.140	-0.221	-0.360	80	10.95	3.24E+05	-394.2	-642.8	858.6
25	AOA5_Fan80_Wind20	7951	0.037	-0.049	-0.011	80	20.36	6.02E+05	-267.6	-501.9	944.7
26	AOA5_Fan80_Wind30	7952	0.084	0.097	0.180	80	30.22	8.94E+05	-99.5	-267.6	1101.1
27	AOA5_Fan80_Wind40	7927	0.049	0.182	0.231	80	40.26	1.19E+06	178.6	101.2	1301.5
28	AOA5_Fan80_Wind50	7914	0.038	0.317	0.355	80	50.48	1.49E+06	490.3	561.3	1552.8
29	AOA10_Fan50_Wind10	5193	-0.037	-0.018	-0.056	50	10.40	3.08E+05	-166.3	-244.8	372.0
30	AOA10_Fan80_Wind10	7800	-0.174	-0.154	-0.327	80	10.91	3.23E+05	-375.3	-609.3	821.7
31	AOA10_Fan80_Wind20	7801	-0.037	0.036	-0.002	80	20.39	6.03E+05	-251.7	-484.5	925.7
32	AOA10_Fan80_Wind30	7744	0.052	0.140	0.191	80	30.22	8.94E+05	-86.8	-226.0	1067.1
33	AOA10_Fan80_Wind40	7729	0.012	0.242	0.253	80	40.30	1.19E+06	214.4	144.6	1268.8
34	AOA10_Fan80_Wind50	7713	-0.046	0.340	0.294	80	50.52	1.49E+06	517.7	608.3	1518.4
35	AOA15_Fan80_Wind10	7744	-0.193	-0.153	-0.347	80	10.80	3.19E+05	-375.4	-609.8	810.1
36	AOA15_Fan80_Wind20	7721	-0.054	0.017	-0.037	80	20.25	5.99E+05	-254.3	-473.0	884.8
37	AOA15_Fan80_Wind30	7694	-0.034	0.133	0.100	80	30.08	8.89E+05	-107.1	-229.2	1013.1
38	AOA15_Fan80_Wind40	7672	-0.089	0.271	0.182	80	40.11	1.19E+06	220.1	125.3	1194.3
39	AOA15_Fan80_Wind50	7651	0.039	0.370	0.409	80	50.24	1.49E+06	347.2	576.5	1409.3
40	AOA20_Fan80_Wind10	7942	-0.183	-0.238	-0.421	80	10.71	3.17E+05	-402.2	-647.9	846.8
41	AOA20_Fan80_Wind20	7905	-0.060	-0.055	-0.115	80	20.08	5.94E+05	-288.5	-513.9	906.9
42	AOA20_Fan80_Wind30	7873	-0.044	0.089	0.046	80	29.79	8.81E+05	-148.0	-280.2	1018.5
43	AOA45_Fan50_Wind0	5184	-0.197	-0.156	-0.353	50	1.91	5.65E+04	-228.5	-299.6	322.9
44	AOA45_Fan80_Wind0	7800	-0.483	-0.393	-0.876	80	3.26	9.65E+04	-496.4	-693.1	775.2

Figure 4.8: Wind tunnel measurements output

4.7.2 Measured forces vs MFR

A series of experiments have been conducted to investigate the influence of changing the MFR on the measured force. Reference to the table shown in figure 4.8 the tests with serial numbers from S.n. 18 till 23 have been performed with fixed wind tunnel air velocity equal to 40m/s, zero angle of attack and by changing the fan speed from 50 to 100 (RPM: 5030 - 8727) to simulate a different MFRs. The calculation has been conducted according to section 4.5 and the results are shown through the graph illustrated in figure 4.10. It can be seen that the higher the MFR is, the larger the back-force attains.

4.7.3 Flow visualisation

This section illustrates the findings obtained from the implementation of surface tufts. Flow is visualised around the nacelle outer surface from figure 4.11 till figure

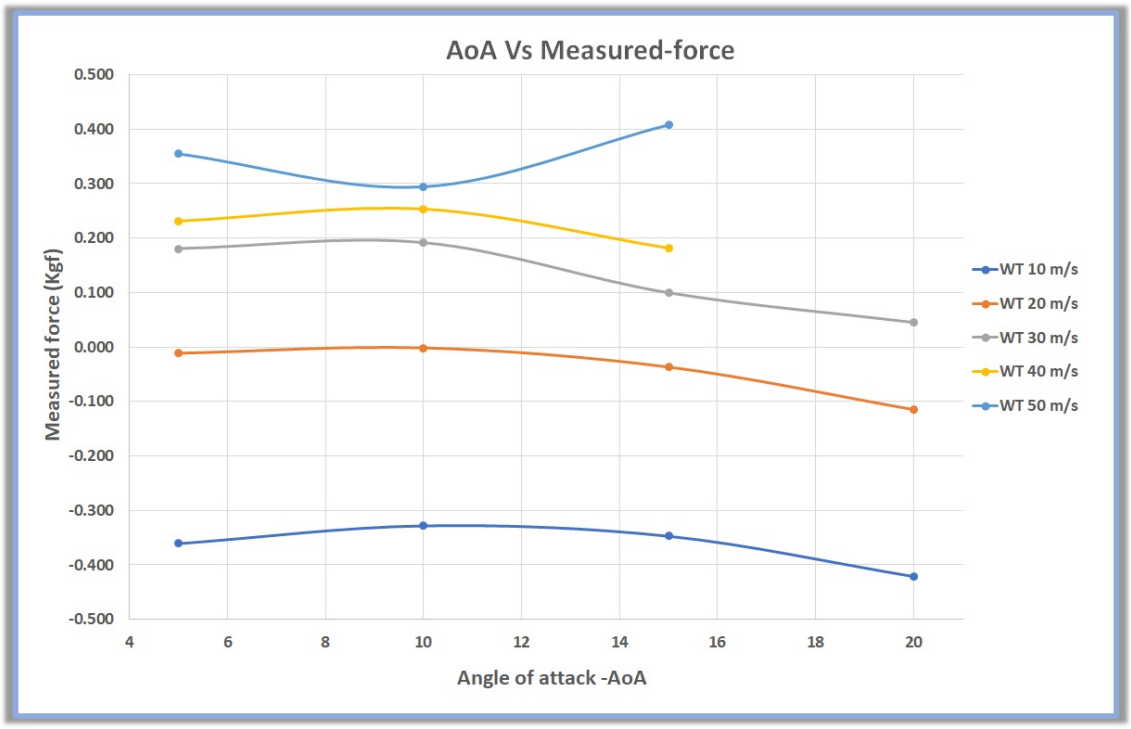

Figure 4.9: Measured force vs AoA

4.16. For the lip inner and outer surface the flow visualisation is presented in figures from 4.17 till 4.22. The setup condition for Wind tunnel air velocity, AoA and EDF rotational speed can be read under each figure. Wind tunnel air velocity has been fixed to 30m/s. Fan input request has two value "0" i.e. the fan was off and 80 which corresponds to an RPM=7871. Several important aspects have been noticed upon increasing the angle of attack from 0°to 25°.

- Separation bubble.
  Separation bubble occurs on the outer surface of the nacelle centrebody. Figures 4.12 and 4.16 left side illustrate the flow for AoA 5° and 10°. The red circle shows, in both figures, the separation points while the green one shows the attached flow. It can be noticed that the flow separates upstream the centrebody and reattached downstream on the after-body surface.
- The effect of the EDF
  The most striking result to emerge from the flow visualisation is that when the EDF is turned on the flow nature around the nacelle changes substantially. This is an evidence that flow-though nacelle models might not be proper to guarantee similarity with real engine nacelles (specially at high AoA), and therefore, powered models are needed. This can be seen, particularly in figure 4.14. The left side of this figure, the fan is off, shows that the the flow is separated from the nacelle outer surface. Meanwhile, right sides, the fan is on, the flow is attached for almost the entire distance of the nacelle. The same phenomena can be seen in figures 4.12 and 4.13 left and right side. However, when AoA=20° and higher the separation occurs at both conditions i.e. whether the fan is on or off.

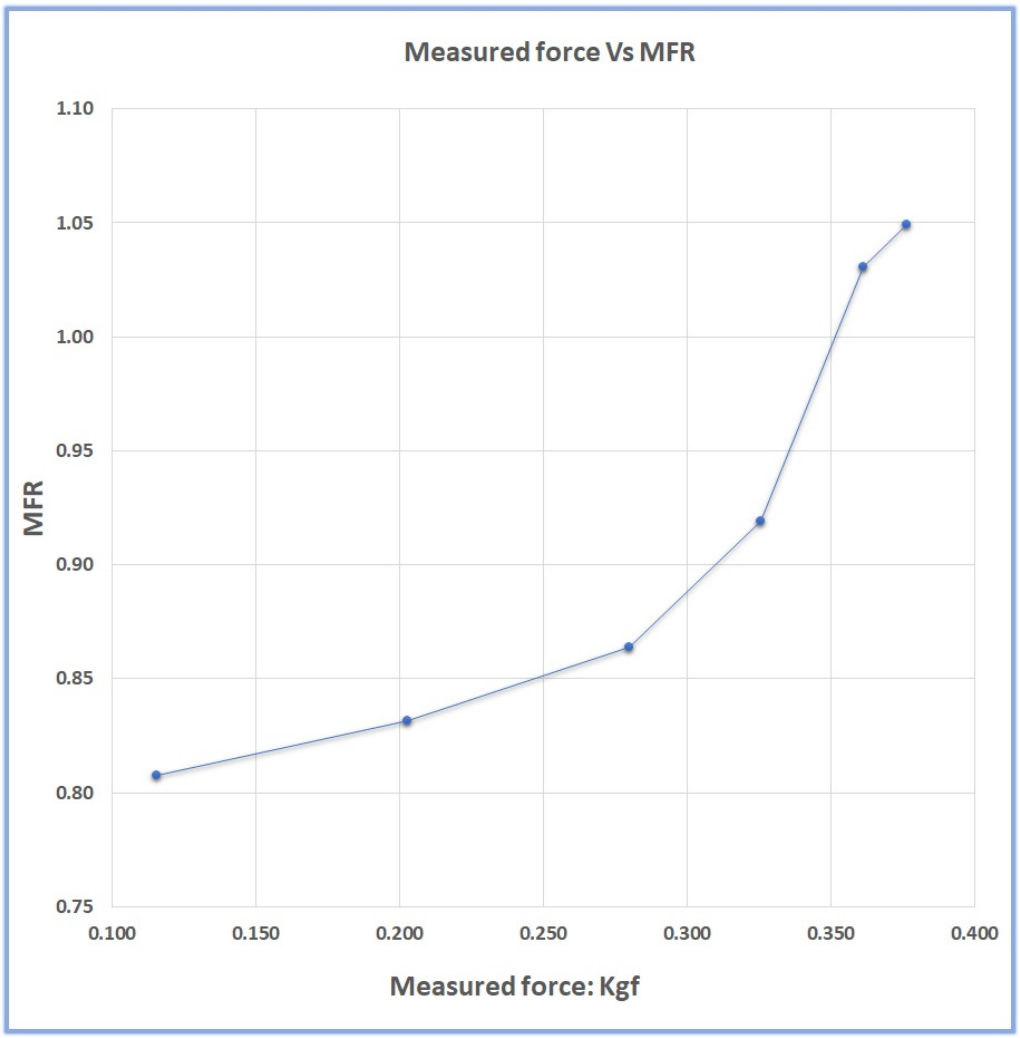

Figure 4.10: Measured force Vs MFR

- Inlet separation
  Figure 4.20 left side shows that flow is separated downstream the outer surface of the lip (marked with red), however the flow remain attached in the inlet side (marked with green). The right side of the same figure is exactly the opposite status. It can be remarkably noticed that the flow through the inlet lip separates completely when the AoA higher or equal to 20°and this is regardless the fan status whether it is on or off.

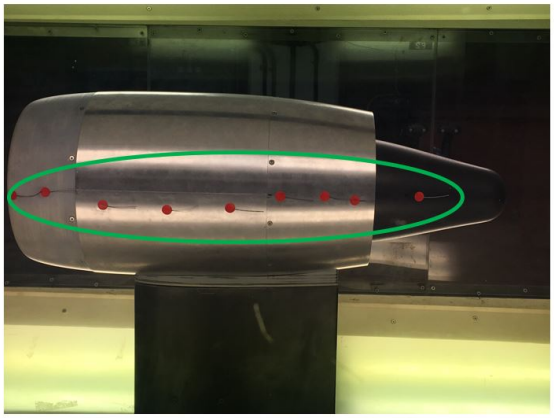

AOA=0, WT speed=30, Fan input request=0.

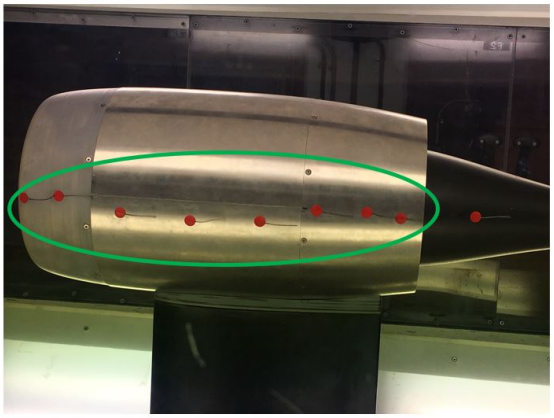

AOA=0, WT speed=30, Fan input request=80.

Figure 4.11

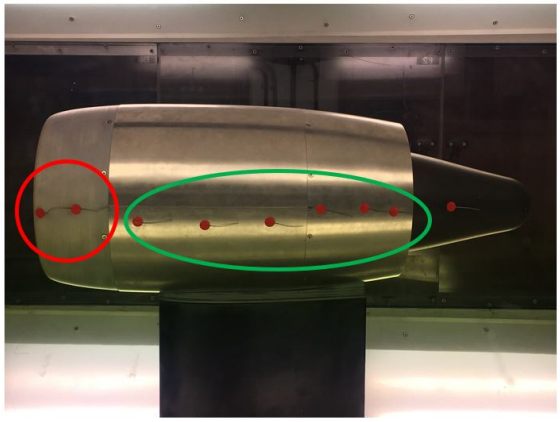

AOA=5, WT speed=30, Fan input request=0.

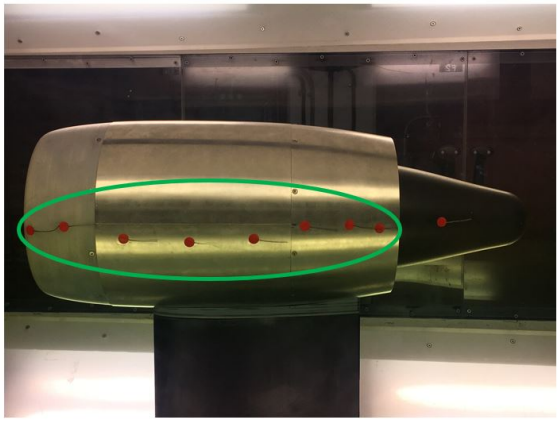

AOA=5, WT speed=30, Fan input request=80.

Figure 4.12

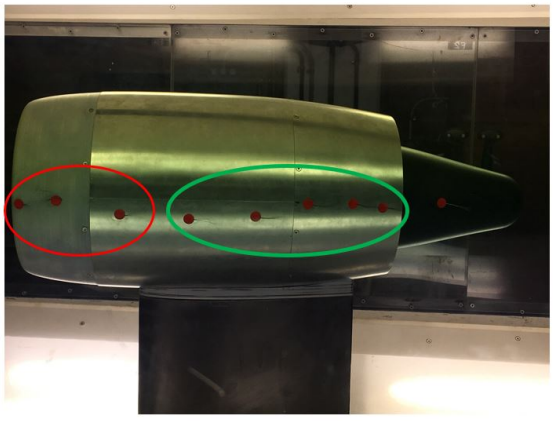

AOA=10, WT speed=30, Fan input request=0.

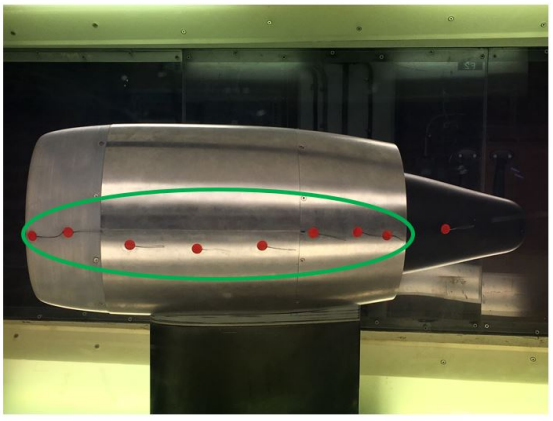

AOA=10, WT speed=30, Fan input request=80.

Figure 4.13

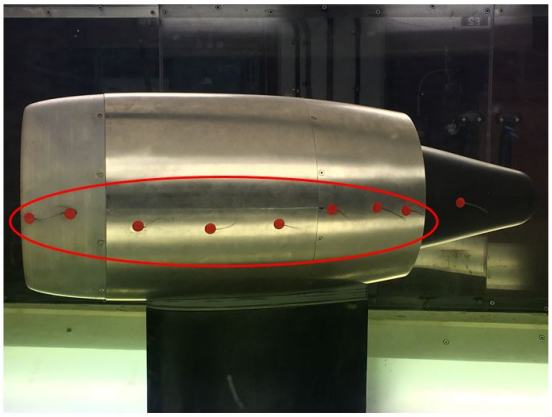

AOA=15, WT speed=30, Fan input request=0.

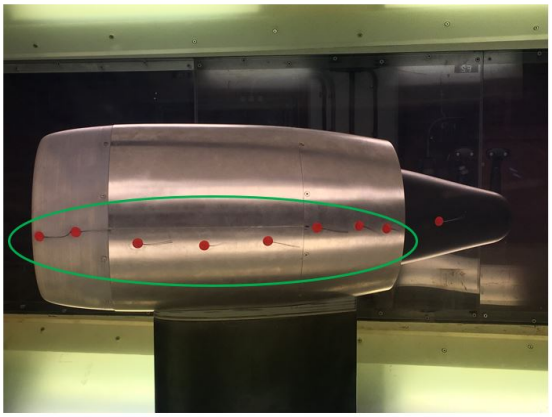

AOA=15, WT speed=30, Fan input request=80.

Figure 4.14

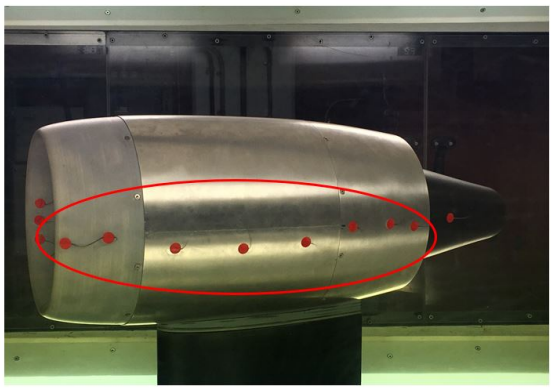

AOA=20, WT speed=30, Fan input request=0.

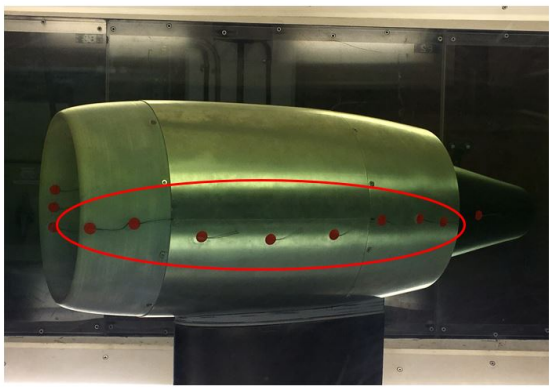

AOA=20, WT speed=30, Fan input request=80.

Figure 4.15

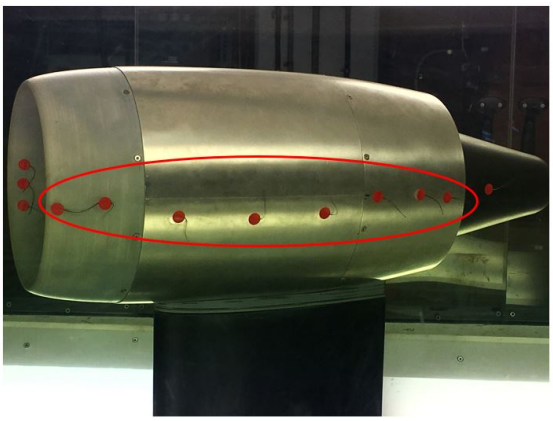

AOA=25, WT speed=30, Fan input request=0.

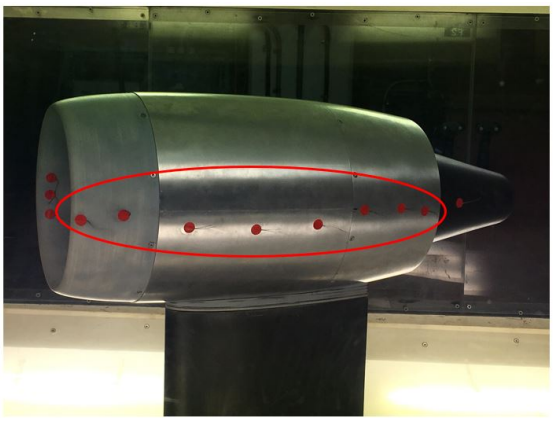

AOA=25, WT speed=30, Fan input request=80.

Figure 4.16

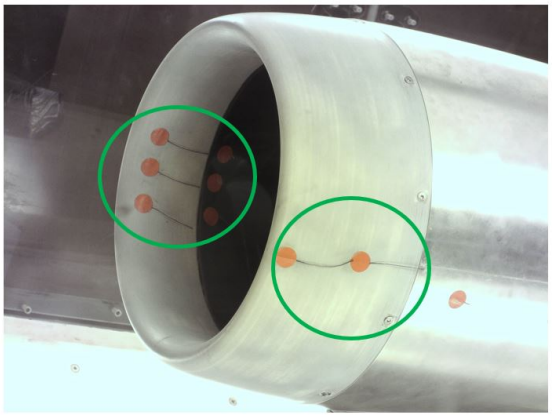

AOA=0, WT speed=30, Fan input request=0.

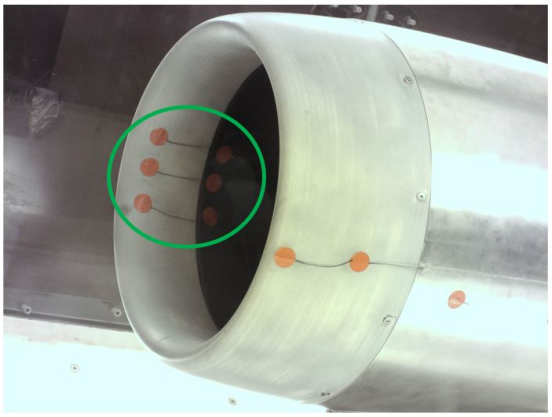

AOA=0, WT speed=30, Fan input request=80.

Figure 4.17

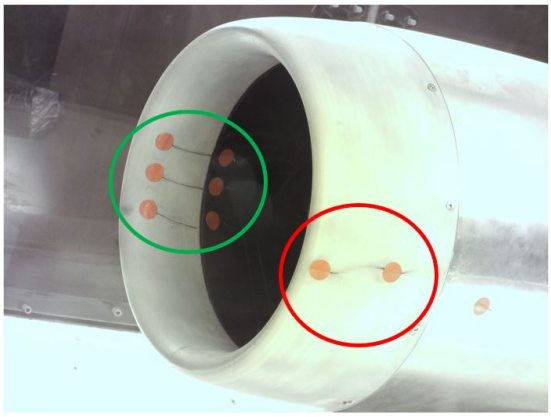

AOA=5, WT speed=30, Fan input request=0.

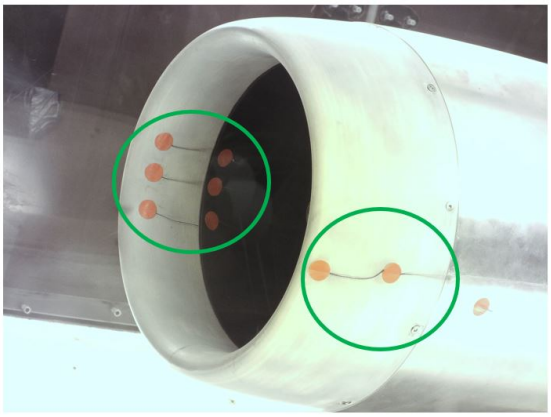

AOA=5, WT speed=30, Fan input request=80.

Figure 4.18

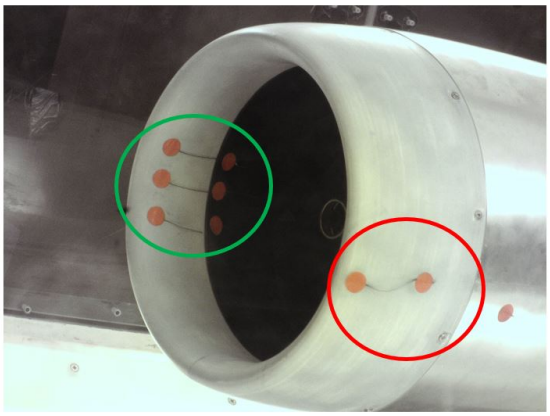

AOA=10, WT speed=30, Fan input request=0.

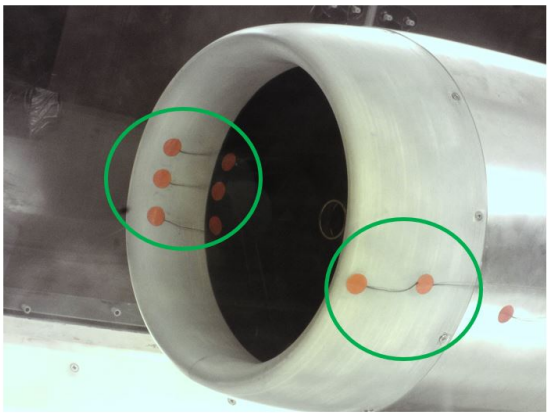

AOA=10, WT speed=30, Fan input request=80.

Figure 4.19

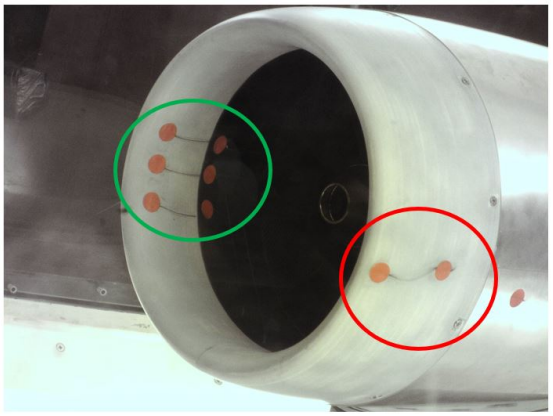

AOA=15, WT speed=30, Fan input request=0.

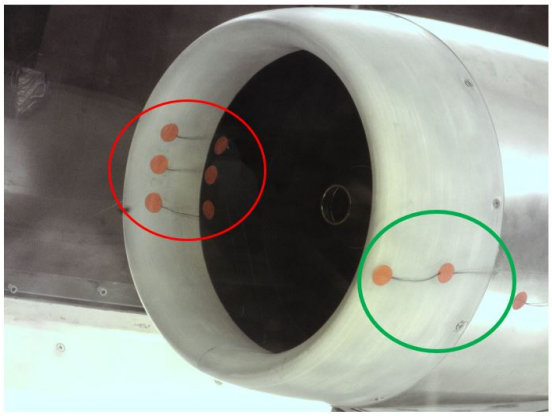

AOA=15, WT speed=30, Fan input request=80.

Figure 4.20

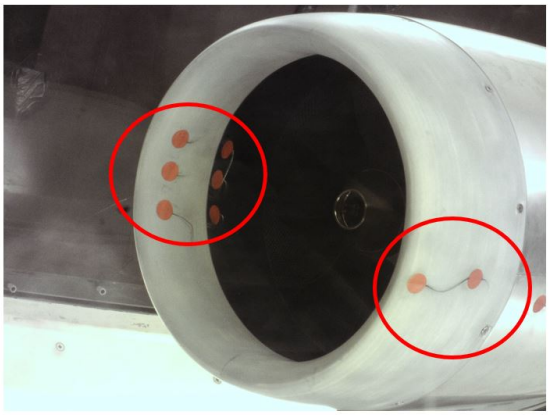

AOA=20, WT speed=30, Fan input request=0.

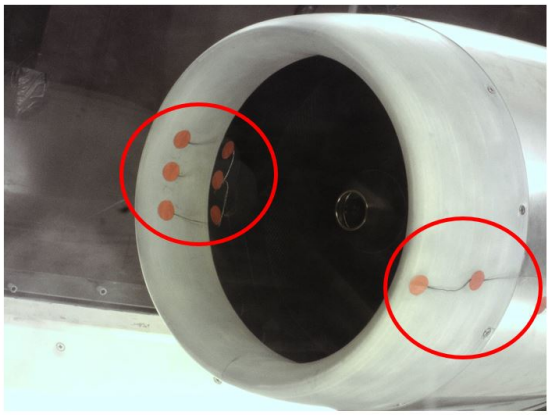

AOA=20, WT speed=30, Fan input request=80.

Figure 4.21

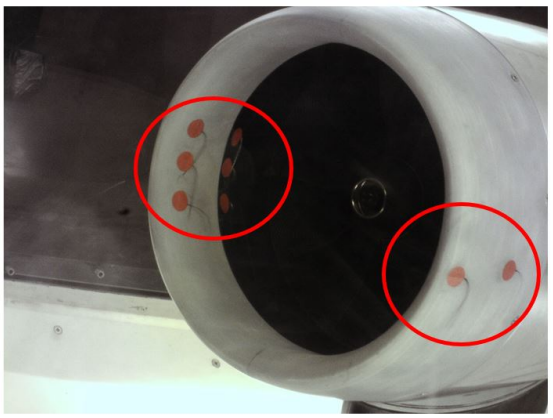

AOA=25, WT speed=30, Fan input request=0.

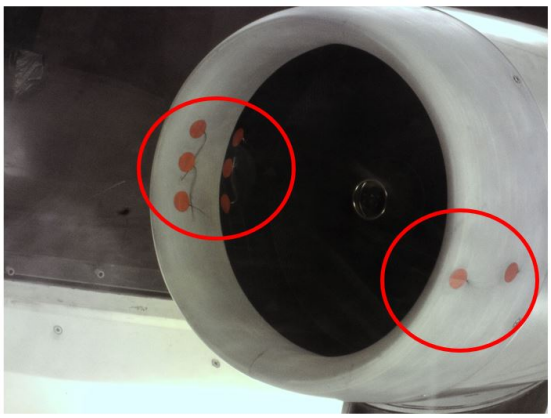

AOA=25, WT speed=30, Fan input request=80.

Figure 4.22

5
Conclusion

The primary objective of this thesis was an experimental investigation of the effects of different mass flow ratios and angle of attacks on the nacelle drag. For that purpose the rig has been designed and built to agree with the requirements of the research. Space limitation was one of the highest challenge during the process of building the model. Some parts were 3D printed with PLA materials others were CNC machined with Aluminium. Load cells selection and installation was an essential task particularly to meet with the space limitation requirement and damping the considerable vibration. Alignment was performed to keep equidistant distance around the circumferential and longitudinal gap. Data acquisition have been performed using the LABVIEW software, such as the code allows to save inputs and outputs in different text file. The MFR has been controlled by changing the EDF rotational speed and keep the wind tunnel air velocity constant. The angle of attack was modified by employing a rotary table. Surface tufts have been used to visualise the flow behaviour around the nacelle surfaces. The values collected from the wind tunnel were not corrected for blockage, doing so would give more accurate results. The main finding of this thesis can be presented in the following three topics:

- The powered nacelle i.e. using an EDF or any propeller inside the nacelle have different flow nature comparing to flow-through nacelle experiments. Flow nature here refers to: the boundary layer thickness, separation and reattachment.
- It has been shown a strong correlation between the MFR and the measured forces. With increased MFR the back-forces become larger. This can be interpreted as when the MFR gets higher the captured stream tube become larger and the stagnation point moves downstream of the outer surface of the nacelle yielding to higher drag forces.
- The measured forces increases for changing AoA from 5° to 10° due to the growth of static pressure in the fan cowl (upwind). For larger AoA, the stagnation point is moved downstream of the highlight, such that, the flow streamlines need to accelerate in order to enter the nacelle. Due to this acceleration low pressure zone in the upwind lip contributes to the decrease of measured forces.

The measured forces are not properly the nacelle drag. A detailed thrust and drag bookkeeping method should be used in order to accurately compute the nacelle drag. However, the measured forces are strongly related to the nacelle drag and are able to provide information on how it behaves at different operating conditions.

6
Future Work

This experimental study is one the first steps towards the development of advanced models for engine aircraft integration systems. There is still space for improving the current model and the results can be used to aid the construction of new and more advanced models. The next steps for the current model are suggested to be: tests with asymmetric nacelles, new measurements such as thrust, pressure distributions, wake survey for drag measurements. Future rigs with more integrated and advanced configurations can be also built. Moreover, the model is intended to be used to validate CFD simulations.

6.1 Asymmetric nacelle with droop angle

Most of the current engine employ nowadays an asymmetric nacelle due to the reasons listed previously in our paper. Future research should further develop and assess what is the impact of asymmetric geometries (such as drooped inlets and thicker bottom lips) on the nacelle aerodynamic performance. To put it differently, it is recommended to conduct drag measurement on the same model but changing the current lip geometry to an asymmetric one since this rig has been designed to be suitable for such future researches.

6.2 Other measurements

In fact this study has dropped at the last stage the option of measuring the thrust generated by the fan. It would be nice to calculate the net propulsive force knowing the gross force and the intake momentum drag. Bearing in mind that the current rig setup allows separate measurement for profile drag and the thrust generated by the fan. Other types of measurement could be promising such as:

- Pressure taps in different longitudinal positions of the nacelle and inlet.
- PIV (particle image velocimetry)
- Wake surveys for getting the skin friction drag

6.3 Integrated model nacelle, pylon and wing

The most promising results can be obtained if such model is integrated with pylon and modelled aircraft wing to constitute what is called "the pod". The latter being tested in the wind tunnel under different AoA and MFR would give deeper and

wider understanding how the drag changes according to the modification of those parameters.

6.4 3D CFD simulation

Future CFD simulations shall be validated against the model results.

6.5 Resolving the issues that affected the drag

The issues presented previously in this work could be corrected by improving the radial fan alignment and by employing corrections for the pressure acting in the internal nacelle surfaces. Last but not least, wind tunnel blockage correction would enhance the overall results.

Bibliography

[1] H.I.H. Saravanamutto et al. *Gas Turbine Theory*. Pearson, Harlow, United Kingdom, 2017.

[2] https://ec.europa.eu/transport/sites/transport/files/modes/air/doc/flightpath2050.pdf.

[3] Frank M. White. *Fluid Mechanics*. McGraw-Hill, 2 Penn Plaza, New York, NY, 10121, 2016.

[4] Olivier Petit. *Gas turbine technology – MTF 171*. Chalmers, 2019.

[5] Anders Lundbladh et al. Installation effects for ultra-high bypass engines, 2017.

[6] Daniel P. Raymer. *Aircraft design: A Conceptual Approach*. AIAA Education series, Reston, Virginia, 2018.

[7] John Anderson. *Fundementals of Aerodynamics*. McGraw-Hill, 2 Penn Plaza, New York, NY, 10121, 2017.

[8] John Anderson. *Introduction to Flight*. McGraw-Hill, 2 Penn Plaza, New York, NY, 10121, 2015.

[9] Andreas Peters et al. Ultrashort nacelles for low fan pressure ratio propulsor. *Journal of Turbomachinery*, 137(TURBO-14-1120):14, 2015.

[10] https://en.wikipedia.org/wiki/File:B787-2139.jpg.

[11] https://commons.wikimedia.org/wiki/File:CFM_56-3_on_a_Continental_Airlines_Boeing_737-500.jpg.

[12] Viktor Pettersson Johan Olofsson. Experimental investigation of an innovative high speed propeller. Master's thesis, Chalmers, 2013.

[13] https://en.wikipedia.org/wiki/Strain_gauge.

[14] J. Anthoine et al. *Measurement Techiniques in Fluid Dynamics*. Von Karaman Institute for Fluid Dynamics, Waterloosesteenweg 72, 1640 Sint-Genesius-Rode, Belgium, 2009.

[15] John E. Bussoletti Brenda M. Kulfan. Fundamental parametric geometry representations for aircraft component shapes. http://imap.brendakulfan.com/docs/CST1.pdf, 2006.

[16] Andreas Petrusson. Aerodynamic evaluation of nacelles for engines with ultra high bypass ratio. Master's thesis, Chalmers, 2017.

[17] Brenda M. Kulfan. A universal parametric geometry representation method - "cst". http://brendakulfan.com/docs/CST2.pdf, 2007.

[18] D. J. Cerantola M. S. Zawislak and A. M. Birk. Identifying opportunities for reducing nacelle drag. In *Proceedings of ASME Turbo Expo 2017: Turbomachinery Technical Conference and Exposition*, GT2017-63977, 2017.

[19] M.J. Langley. The design of axisymmetric cowls for podded nacelles for high bypass ratio turbofan engines. In *Aircraft research Association Limited, Bedford*, RM No. 3846, 1979.

[20] John R. Carlson and William B. ComptonIII. An experimental investigation of nacelle-pylon installation on an unswept wing at subsonic and transonic speed. https://ntrs.nasa.gov/search.jsp?R=19840010094, 1984.

[21] http://www.schuebeler-jets.de/en/products/hst-en.

[22] C.A.Hall S.L. Dixon. *Fluid Mechanics and Thermodynamics of Turbomachinery*. Butterworth-Heinemann, Oxford UK, 2014.

[23] http://www.ni.com/data-acquisition/what-is/.

[24] https://people.clarkson.edu/~pmarzocc/AE429/The%20NACA%20airfoil%20series.pdf.

[25] http://airfoiltools.com/search/index?m%5BmaxCamber%5D=0&m%5Bsort%5D=5&MAirfoilSearchForm%5BtextSearch%5D=&MAirfoilSearchForm%5BmaxThickness%5D=&MAirfoilSearchForm%5BminThickness%5D=&MAirfoilSearchForm%5BmaxCamber%5D=0&MAirfoilSearchForm%5BminCamber%5D=&MAirfoilSearchForm%5Bgrp%5D=naca4d&MAirfoilSearchForm%5Bsort%5D=5&yt0=Search.

[26] https://www.vetek.com/load-cell-03-kg-single-point-aluminium-oiml-/article.

[27] http://www.ni.com/pdf/manuals/374186a_02.pdf.

[28] Sandra Busch Isak Jonsson. Wind tunnel test of a double blade swept propeller and analysis of real geometry effects. Master's thesis, Chalmers, 2015.

[29] https://www.mgm-controllers.com/multicopters/speed-controllers-escs-4/tmm-40063-3-for-multicopters-x2-series.html.

[30] https://www.lem.com/sites/default/files/products_datasheets/has_50_600-s_e.pdf.

[31] https://www.ni.com/sv-se/support/model.usb-6210.html.

A

Appendix 1

SCHÜBELER
TECHNOLOGIES GmbH

Our successful HST fan series is now in 2016 extended with a noteworthiness. The logical consequence from several customer requests and usage potential in jet model flying is our DS-215-DIA HST, a propulsion of the new 195mm series. This imposing propulsion is based on know-how referring to all the other HST models we have developed trhoughout the years. Besides, the DS-215-DIA HST has been fully developed in assistance with a CFD-tool. This results in an increased level of efficiency and an extremely low level of sound.

All mechanical components of the fan have been designed with a special focus on durability and robustness. For example the 35mm hollow shaft from aluminum 7075 provides highest stiffness.

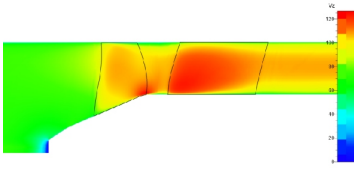

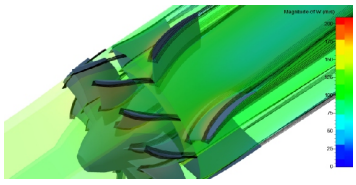

All mechanical components of the fan have been designed with a special focus on durability and robustness. For example the 35mm hollow shaft from aluminum 7075 provides highest stiffness. Such mechanical feature allows for a fan composition with minimum blade clearance.

The internal rotor in its new patented design propells the fan with powerful 10Nm of torsional moment. The rotational speed was intentionally kept low at 14.000 U/min. The motor is cooled by means of our patented cooling system. The DS-215-DIA HST is the ideal propulsion for your single-engined jet modell with a maximum weight of 25kg.

DS-215-DIA HST®

Efficiency and thrust in new dimensions

Technical Data:

DS-215-DIA HST® (195mm) withDSM10066-290

Inner shroud diameter: 195 mm
Fan swept area: 215 cm²
Weight incl. motor, wiring,
Plug and Secure Fan Fix: 3400 g
Thrust range: 215-250 N
Exhaust Speed Range: 84-98 m/s
RPM range: 12.000-14.000 U/min
Input power: 9,8-15,6 kW
Allowed battery: 10-14S 20000 mAh
Overall efficiency: 78 %

Schübeler Technologies GmbH
Phone +49 5252 8398495
info@schuebeler-jets.de
www.schuebeler-store.de
www.schuebeler-jets.de

Figure A.1: Fan data sheet

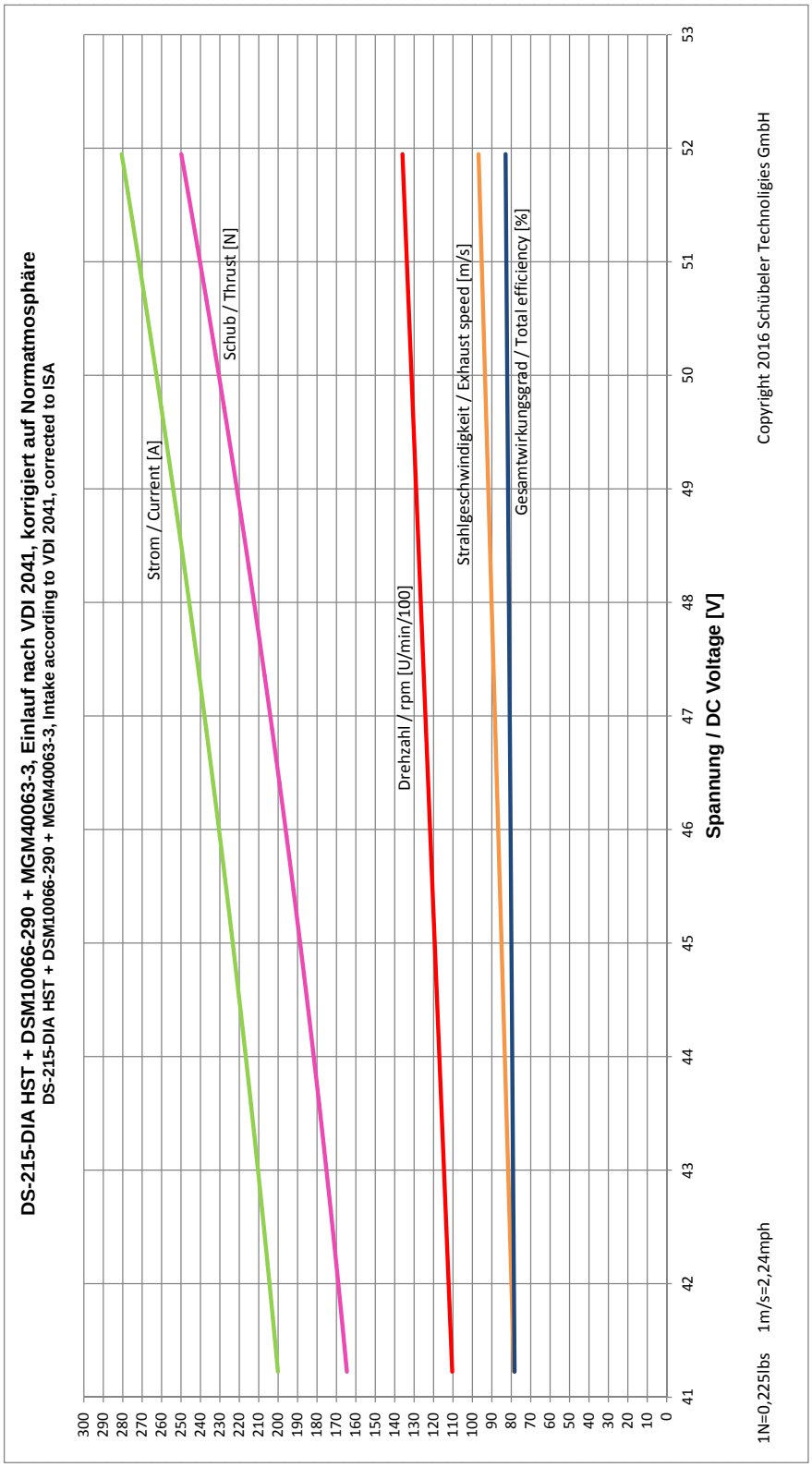

Figure A.2: Fan measurements

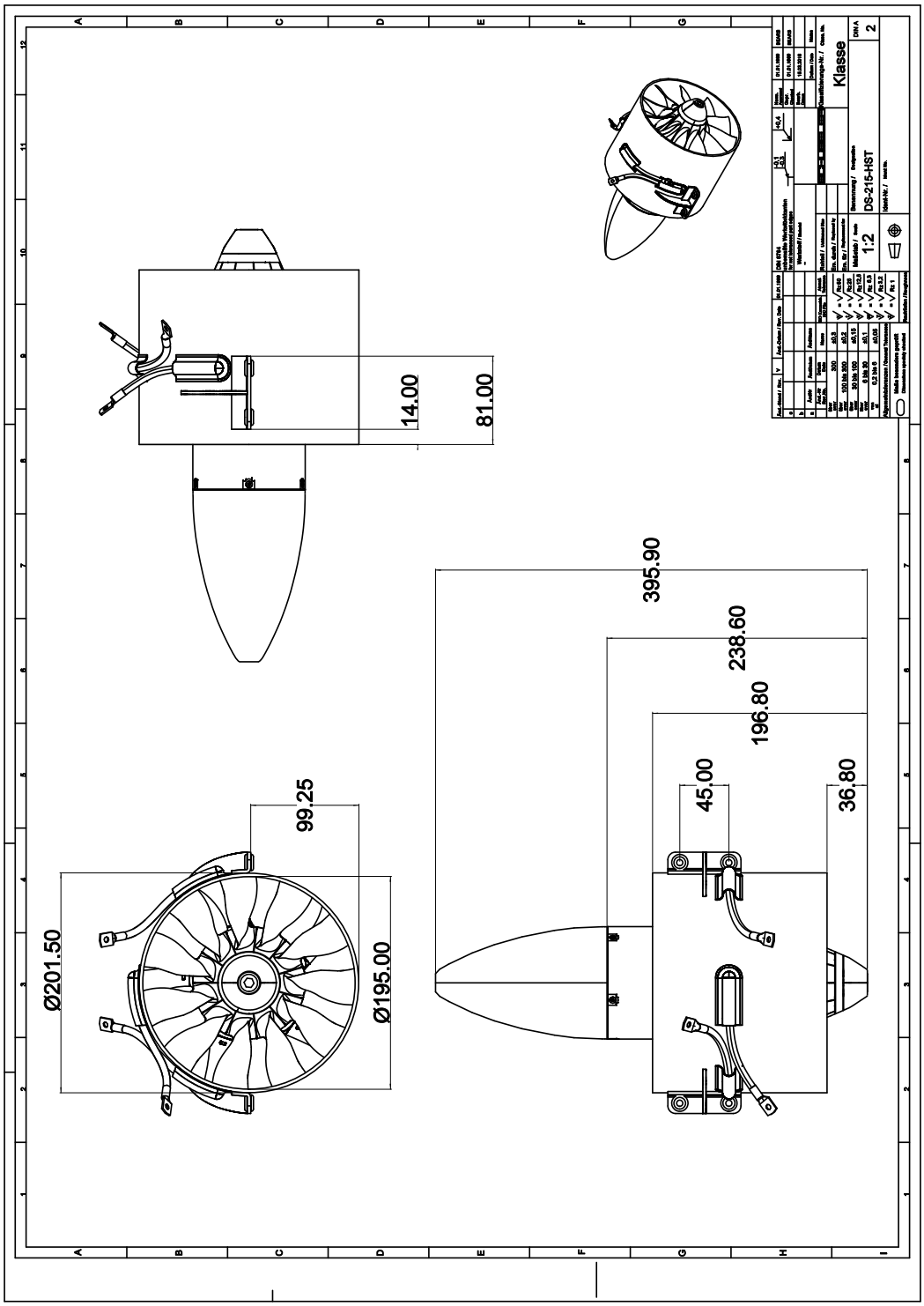

Figure A.3: Fan dimensions 1

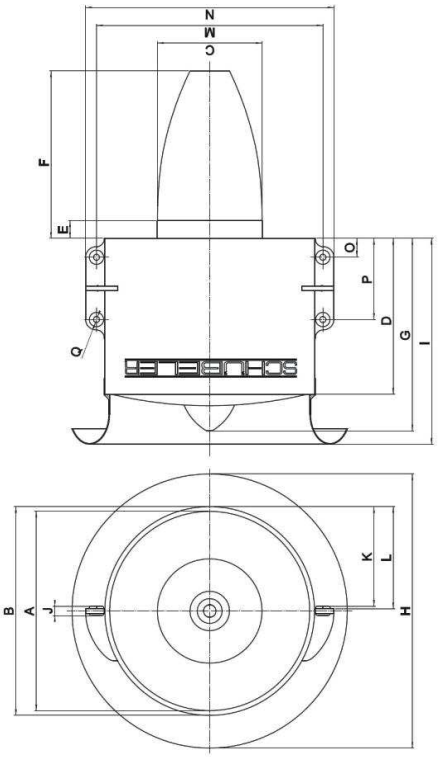

-15-

Drawing #6 (Dimensions of the Impeller):

Table #2:

	Ducted Fan							Intake			Secure Fan Fix								
	A	B	C	Stator Inside ⌀	D	E	F	G	H	I	J	tightened	K	L	M	N	O	P	Q
	⌀ mm	⌀ mm	⌀ mm	mm	mm	mm	mm	mm	⌀ mm	mm	mm	mm	mm	mm	mm	mm	mm	mm	
DS 30 AXI HDS®	69.0	70.5	30.5	29.0	49.0			61.0	95.0	66.0	5.5	4.5 – 3.0	32.5	34.5	79.5	90.0	9.0	31.0	M3x12
DS 51 AXI HDS®	90.0	92.0	41.0	39.0	60.0	-	-	78.0	124.0	82.5	6.0	5.0 – 3.5	43.0	44.5	103.0	113.0	9.0	39.0	M4x12
DS 86 AXI HDS®	120.0	122.6	58.5	56.0	78.0			97.5	165.0	108.0	6.0	5.0 – 3.5	58.5	60.0	137.0	147.0	10.5	50.5	M4x12
DS 51 DIA HST®	93.0	98.5	46.0		67.0	34.0	100.0	83.0	130.0	90.0			46.0	47.5	108.5	118.5	10.0	40.0	
DS 82 DIA HST®	120.0	126.0	63.0		100.0	15.0	114.5	123.5	168.0	130.0	6.0	5.0 - 3.5	60.0	61.5	136.5	150.5	12.0	52.0	M4x12
DS 98 DIA HST®	128.0	134.0		-					176.0	132.0			64.0	65.5	144.5	158.5			
DS 171 DIA HST®	180.0	187.0	103.0		160.0	45.5	200.0	195.0	248.0	205.0	8.0	7.5 – 6.5	89.0	91.5	205.5	224.5	25.0	70.0	M6x16
DS 215 DIA HST®	195.0	202.0							268.0	208.0			96.5	99.5	220.5	239.5			

Figure A.4: Fan dimensions 2

VETEK

108AA

Aluminum

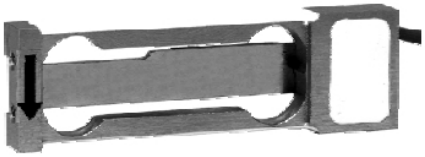

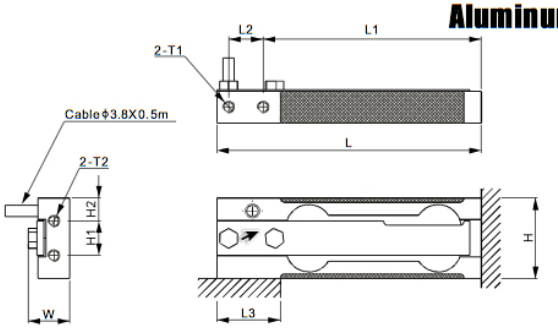

CE RoHS IP66 OIML

DIMENSIONS

RATED CAPACITY	H	H1	H2	L	L1	L2	L3	W	T1	T2
kg/mm										
0.1···5	28.0	12.0	8.0	92.0	76.0	12.0	22.0	14.5	2-M4 Depth 8	2-M4
lb/inches (conversion of above dimensions)										
0.22···11.02	1.10	0.47	0.31	3.62	2.99	0.47	0.87	0.57	2-M4 Depth 0.31	2-M4

SPECIFICATIONS			
Accuracy class		-	C3
Rated Capacity	kg	0.1; 0.2; 0.3; 0.5	1; 2; 3; 5
Weight (G), approx.	kg/lb	0.1 / 0.22	0.1 / 0.22
Reference Max. Platform Size	mm	200×200	230×230
Full Scale Output	mV/V	1 ± 20%	2 ± 20%
Zero Balance	mV/V	± 0.05	0.05
Non-linearity *	%	< ± 0.023	< ± 0.017
Repeatability *	%	< ± 0.023	< ± 0.017
Hysteresis Error *	%	< ± 0.023	< ± 0.017
Creep in 30 min.	%	< ± 0.050	< ± 0.023
Bridge Resistance	Ω	415 ± 15	
Rated Excitation	V(DC/AC)	10 (15V Maximum)	
Insulation Resistance	GΩ	>1 [50 VDC]	
Nominal Temperature Range	°C/°F	-10 to 40 / 14 to 104	
Safe Overload	% of full scale	150	
Breaking Overload	% of full scale	300	
Seal Type		Environmentally-sealed, IP66	
Reference Mounting		Socket-head cap screw: M4-8.8 Tightening torque: 2.5Nm	

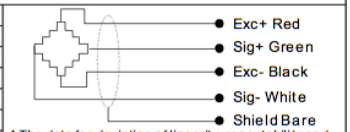

** The data for deviation of linearity, repeatability and hysteresis error meets the requirements according to OIML R60*

Figure A.5: Load cell: data sheet

RS PRO

ENGLISH

Datasheet

Sealed Lead-Acid Battery
General Purpose

727-0398(12V100Ah)

Specification

Cells Per Unit	6
Voltage Per Unit	12
Capacity	100.0Ah@10hr-rate to 1.80V per cell @25°C
Weight	Approx 30.4 kg
Max. Discharge Current	1200A (5 sec)
Internal Resistance	Approx 4.9mΩ
Operating Temp.Range	Discharge : -15~50°C (5~122°F) Charge : 0~40°C (32~104°F) Storage : -15~40°C (5~104°F)
Nominal Operating Temp. Range	25±3°C (77±5°F)
Float charging Voltage	13.5 to 13.8 VDC/unit Average at 25°C
Recommended Maximum Charging Current Limit	30.0A
Equalization and Cycle Service	14.4 to 15.0 VDC/unit Average at 25°C
Self Discharge	The batteries can be stored for more than 6 months at 25°C. Self-discharge ratio less than 3% per month at 25°C. Please charge batteries before using.
Terminal	T11
Container Material	A.B.S. (UL94-HB) , Flammability resistance of UL94-V0 can be available upon request.

Applications

- *All purpose*
- *Uninterruptable Power Supply (UPS)*
- *Electric Power System (EPS)*
- *Emergency backup power supply*
- *Emergency light*
- *Railway signal*
- *Aircraft signal*
- *Alarm and security system*
- *Electronic apparatus and equipment*
- *Communication power supply*
- *DC power supply*
- *Auto control system*

Dimensions

Unit: mm Dimension: 330(L)×173(W)×212(H)×220(TH)

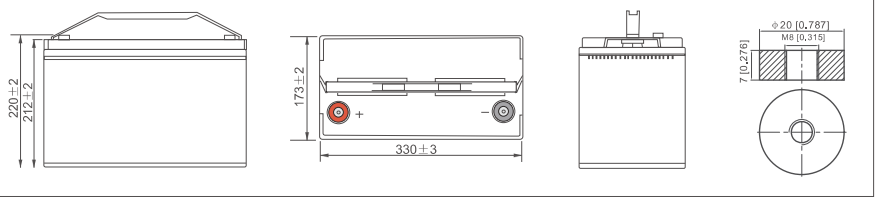

Constant Current Discharge Characteristics : A (25°C) — Amps

F.V/Time	5min	10min	15min	20min	30min	45min	1h	2h	3h	4h	5h	6h	8h	10h	20h
1.85V/cell	173.6	146.4	130.2	115.3	87.5	65.2	52.4	31.3	23.5	19.2	16.4	14.4	11.6	9.65	5.13
1.80V/cell	210.0	167.6	143.7	123.5	92.1	68.7	55.1	33.1	24.6	20.2	17.2	15.0	12.0	10.0	5.20
1.75V/cell	237.0	186.3	154.0	130.8	96.5	71.3	57.1	34.4	25.4	20.7	17.6	15.3	12.2	10.1	5.29
1.70V/cell	261.6	199.5	165.1	138.9	101.8	74.6	59.5	35.3	26.0	21.2	17.9	15.6	12.4	10.2	5.34
1.65V/cell	291.7	215.1	178.5	146.6	106.7	77.4	61.9	36.3	26.7	21.7	18.3	15.9	12.6	10.3	5.40
1.60V/cell	330.8	232.5	188.5	154.3	112.3	80.5	63.8	37.5	27.6	22.2	18.6	16.2	12.7	10.5	5.45

Constant Power Discharge Characteristics : W (25°C) — Watts

F.V/Time	5min	10min	15min	20min	30min	45min	1h	2h	3h	4h	5h	6h	8h	10h	20h
1.85V/cell	322.5	274.9	247.1	220.5	168.5	126.4	102.2	60.8	45.7	37.5	32.2	28.2	22.9	19.1	10.2
1.80V/cell	386.4	312.2	271.0	235.1	176.8	132.7	107.2	63.8	47.7	39.2	33.6	29.4	23.7	19.8	10.3
1.75V/cell	431.3	344.9	288.7	247.8	184.3	137.3	110.8	66.0	49.1	40.1	34.3	29.9	24.0	19.9	10.4
1.70V/cell	470.9	366.5	307.7	261.8	193.6	143.0	115.0	67.6	50.1	41.0	34.8	30.4	24.3	20.1	10.5
1.65V/cell	519.3	391.4	330.2	274.5	201.9	147.7	119.1	69.2	51.3	41.8	35.3	30.8	24.6	20.3	10.6
1.60V/cell	578.9	418.2	345.1	286.6	211.1	152.9	122.4	71.1	52.7	42.6	35.9	31.3	24.8	20.5	10.7

Figure A.6: Battery: data sheet 1 of 2

RS PRO

ENGLISH

Effect of Temperature on Long Term Float Life

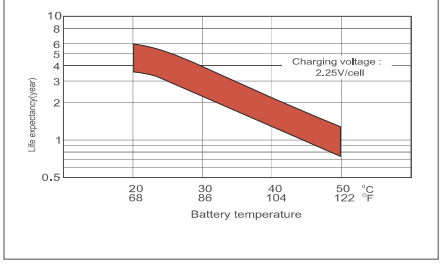

Self Discharge Characteristics

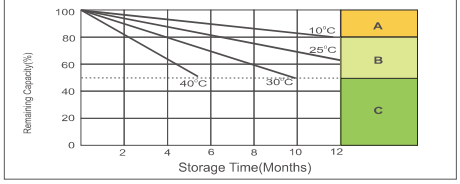

A No supplementary charge required
(Carry out supplementary charge before use if 100% capacity is required.)

B Supplementary charge required before use.Optional charging way as below:
1.Charged for above 3 days at limted current 0.25CA and constant volatge 2.25V/cell.
2.Charged for above 20hours at limted current 0.25CA and constant volatge 2.45V/cell.
3.Charged for 8~10hours at limted current 0.05CA .

C Avoid this storage period unless regular Top charge.
Supplementary charge may often fail to recover the full capacity

Float Charging Characteristics

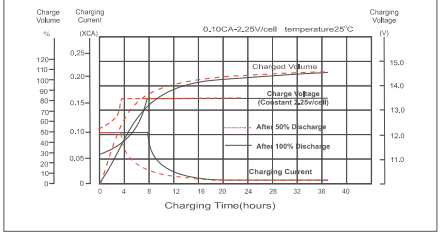

Discharge Characteristics

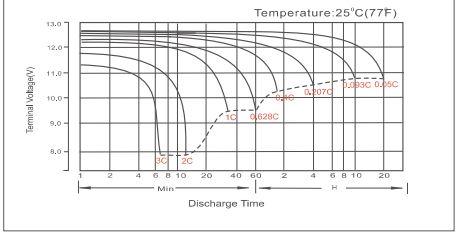

Available Capacity Subject to Temperature

Battery Type		-20℃	-10℃	0℃	5℃	10℃	20℃	25℃	30℃	40℃	45℃
AGM Battery	6V&12V	46%	66%	76%	83%	90%	98%	100%	103%	107%	109%

Discharge Current VS. Discharge Voltage

Final Discharge Voltage V/cell	1.80V	1.75V	1.60V
Discharge Current (A)	（A）≤0.2C	0.2C＜（A）＜1.0C	（A）≥1.0C

Charge the batteries at least once every six months, if they are stored at 25°C.

Charging Method:

Constant Voltage	-0.2Cx2h+2.4~2.45V/Cellx24h,Max. Current 0.3CA
Constant Current	0.1C until the voltage reaching 14.4V,then 0.1Cx4h

Maintenance & Cautions

Float Service:
◆It is recommended to check battery/Float voltage each month.
Equalisation charge:
◆Equalisation charging is recommended once every 3 to 6 months using.
◆Discharge 100% rated capacity.
◆Charge 2.35v/cell constant voltage, maximum 0.3CA 24hrs.
Cyclic Service:
◆Temperature compensation for varying temperatures:
-Charge voltage -3mV/Cell/degC from 25degC norm.
◆The service life of your battery will be affected by:
-The number of discharge cycles, depth of discharge, ambient
temperature and charging voltage.

RS, Professionally Approved Products, gives you professional quality parts across all products categories. Our range has been testified by engineers as giving comparable quality to that of the leading brands without paying a premium price.

Figure A.7: Battery: data sheet 2 of 2

B

Appendix 2

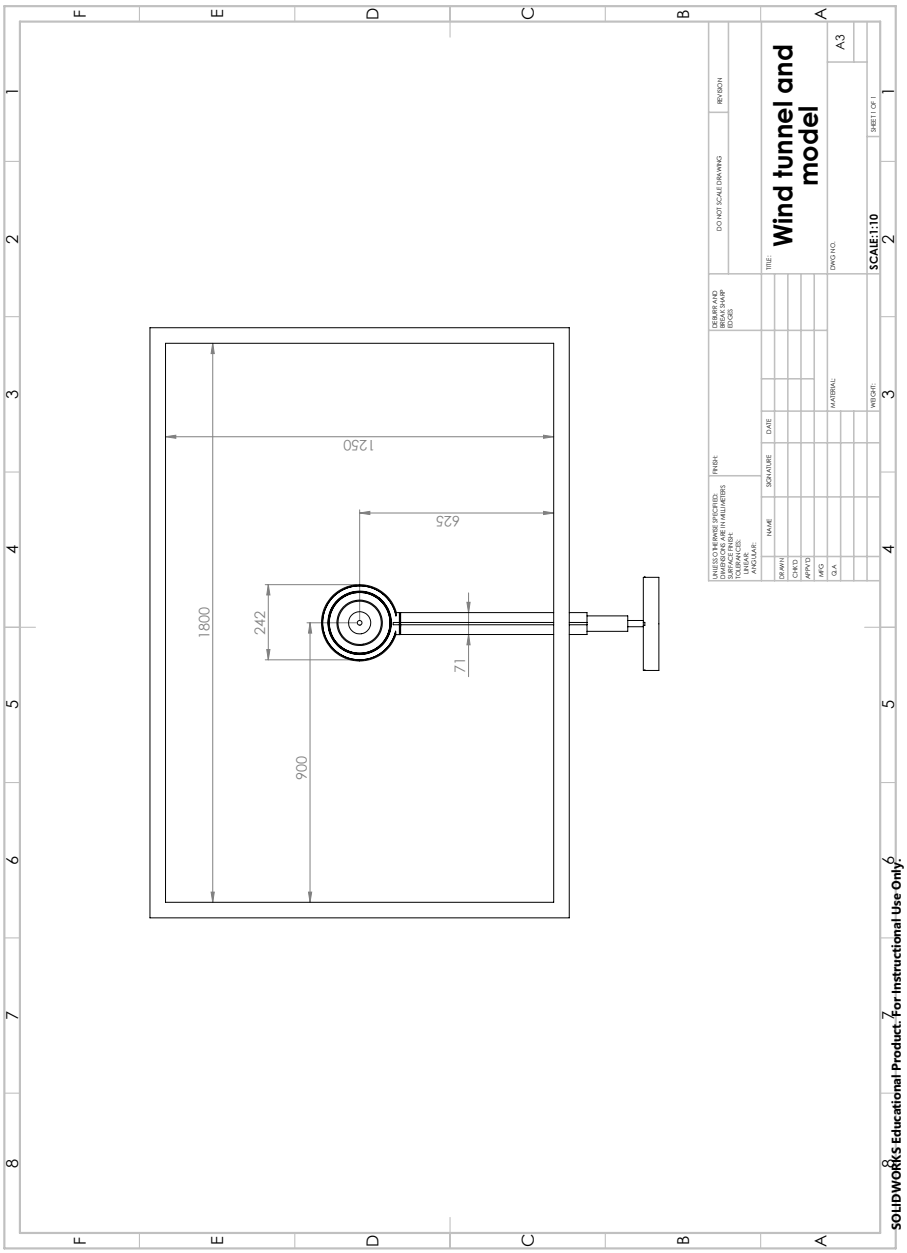

Figure B.1: Overview wind tunnel-model

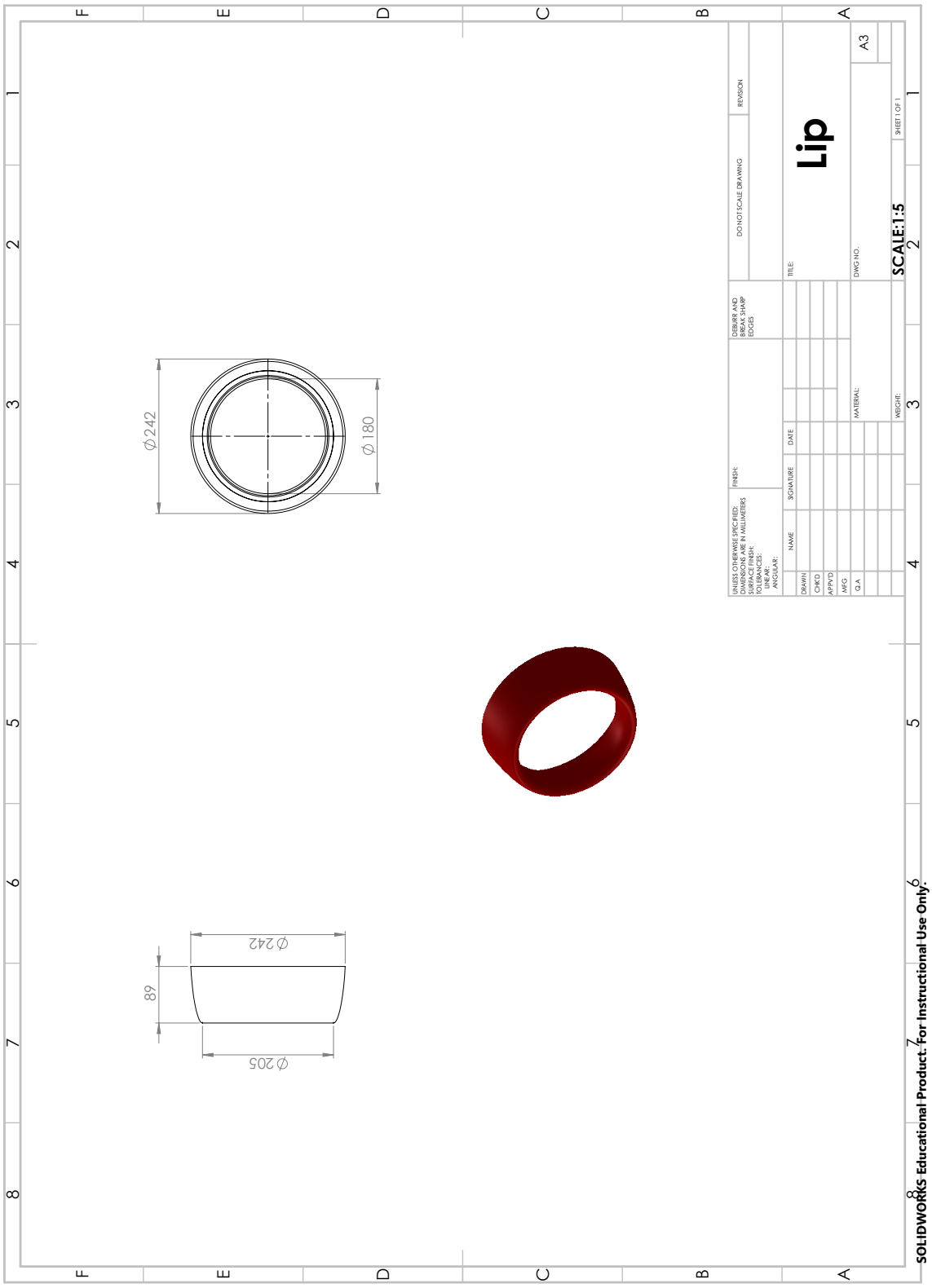

Figure B.2: Lip technical drawing

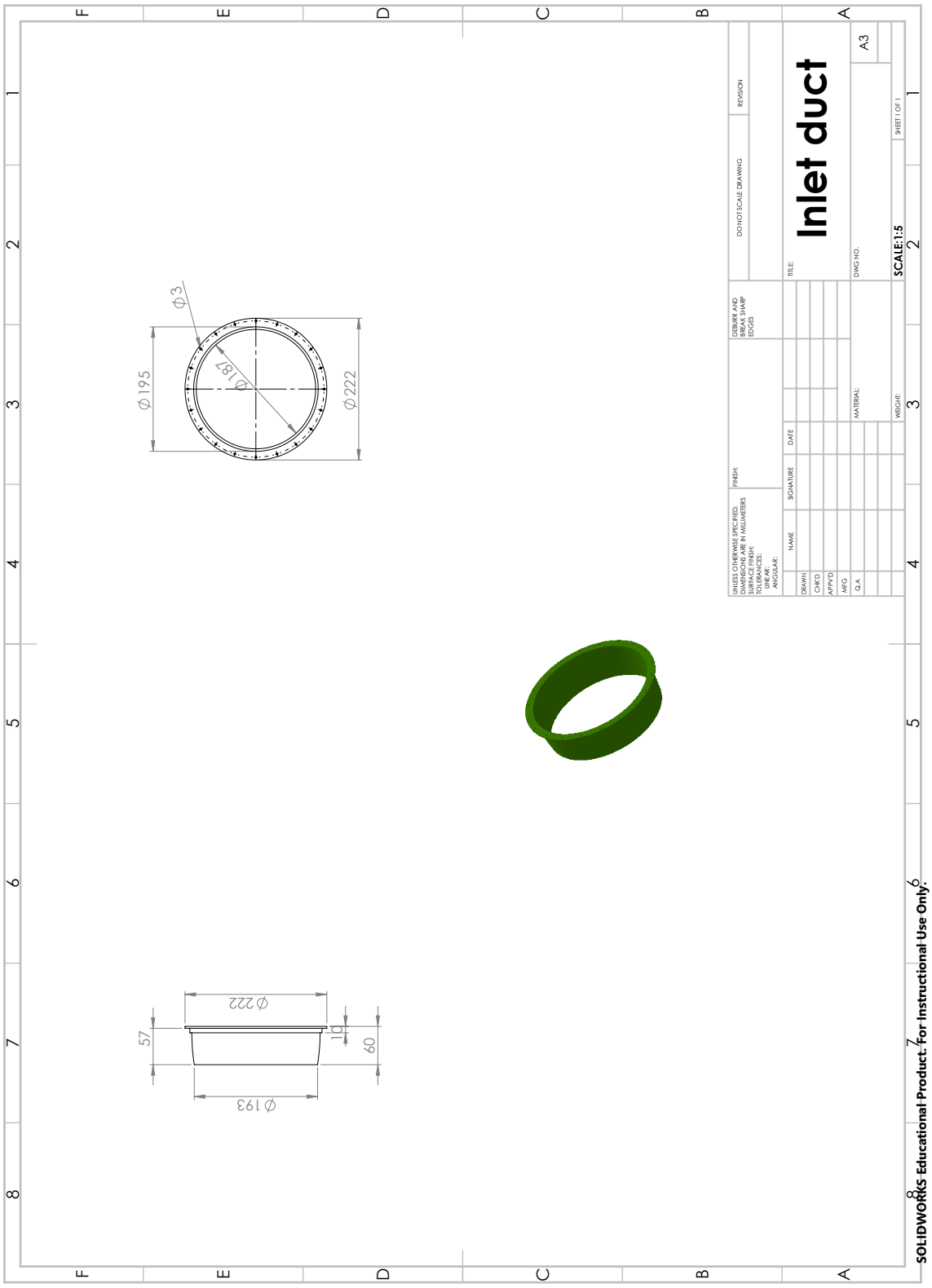

Figure B.3: Inlet duct technical drawing

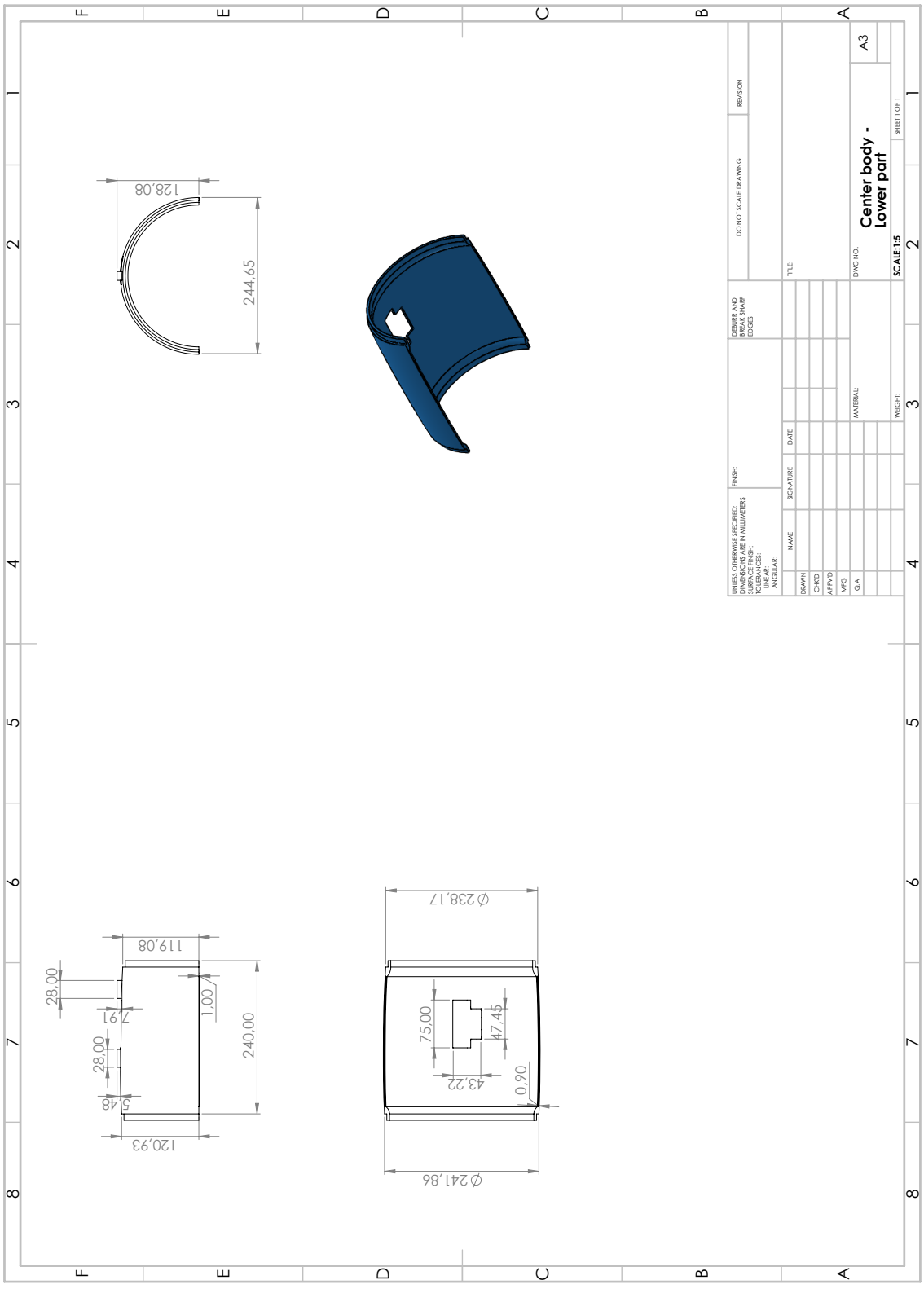

Figure B.4: Centre body lower part technical drawing

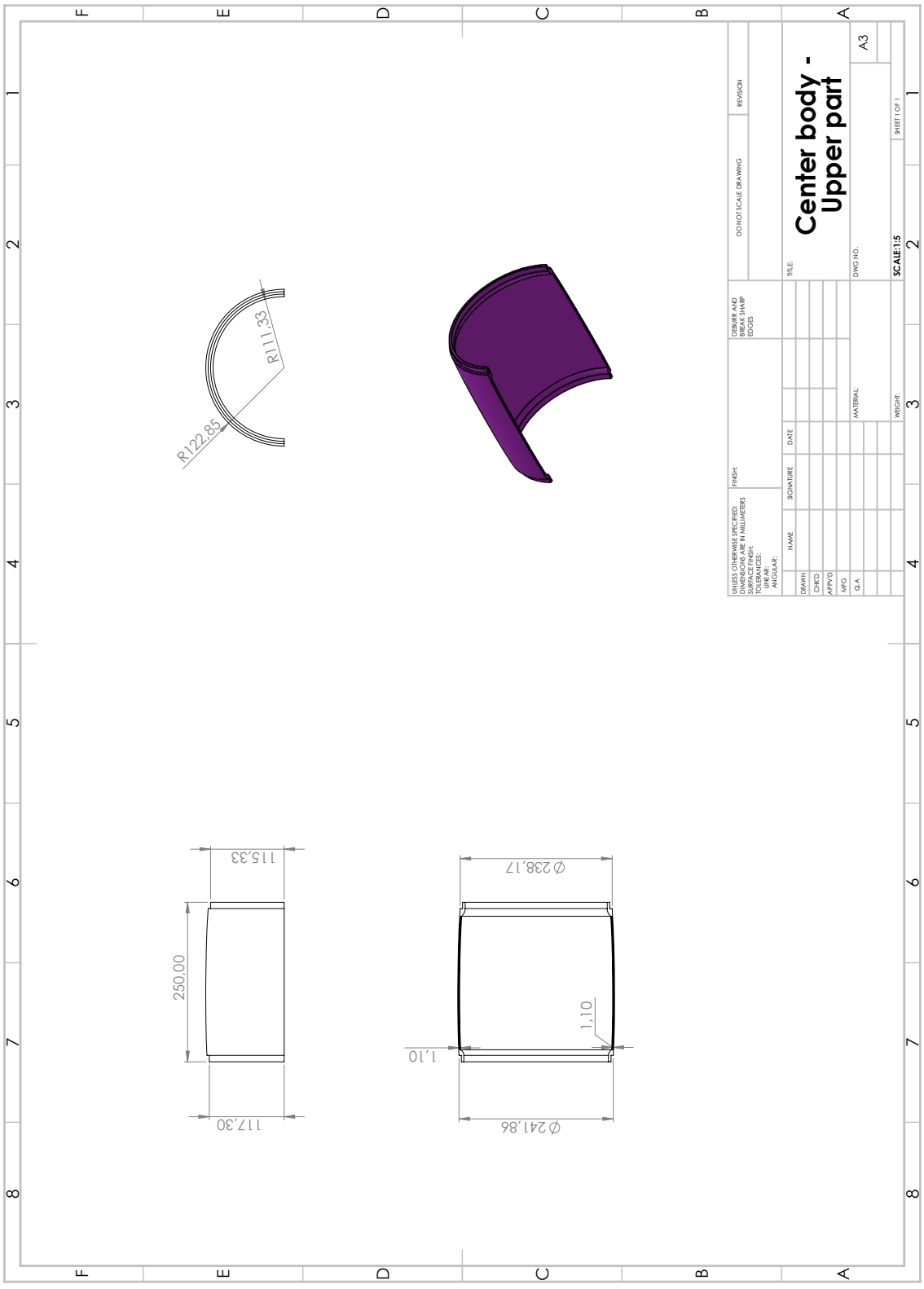

Figure B.5: Centre body upper part technical drawing

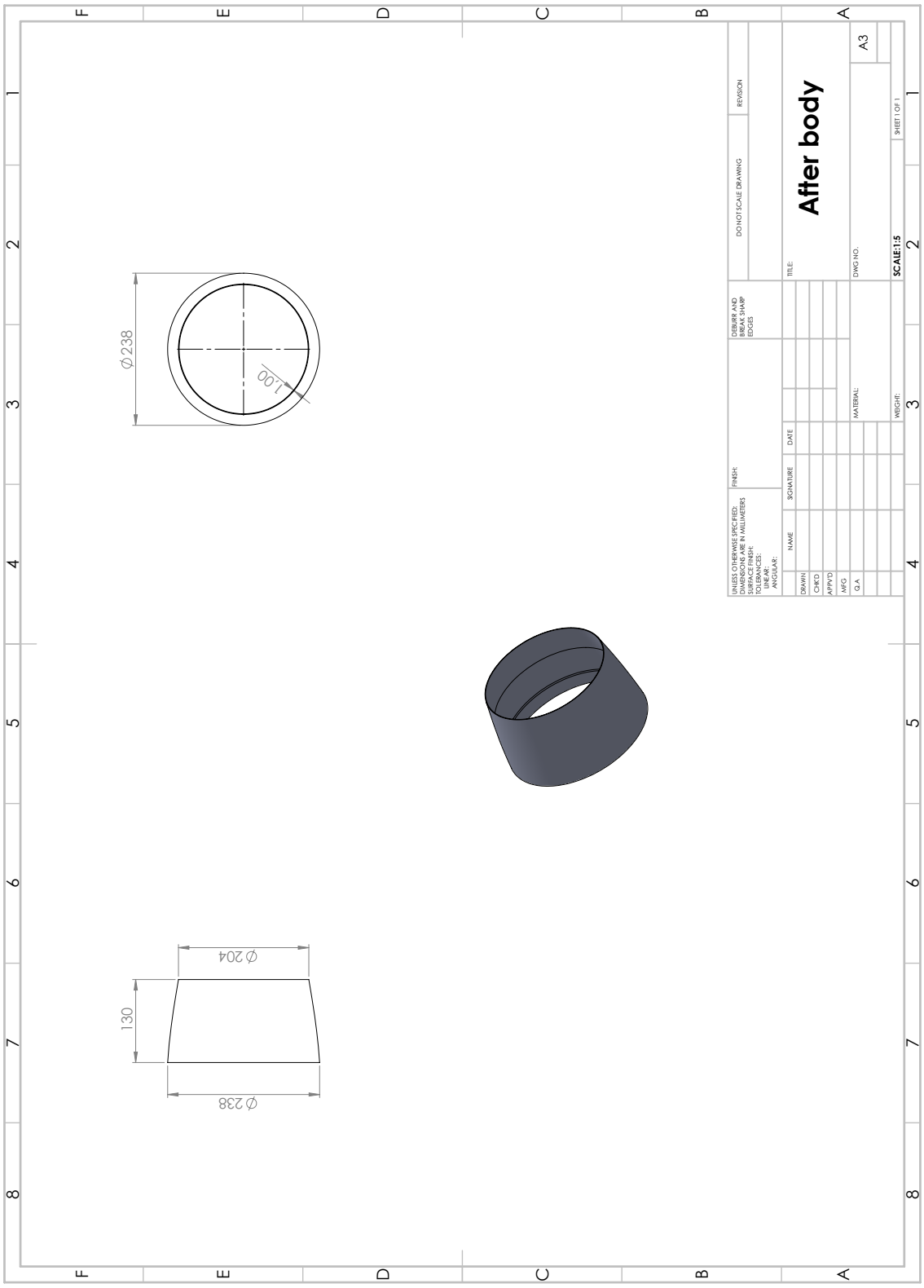

Figure B.6: After body technical drawing

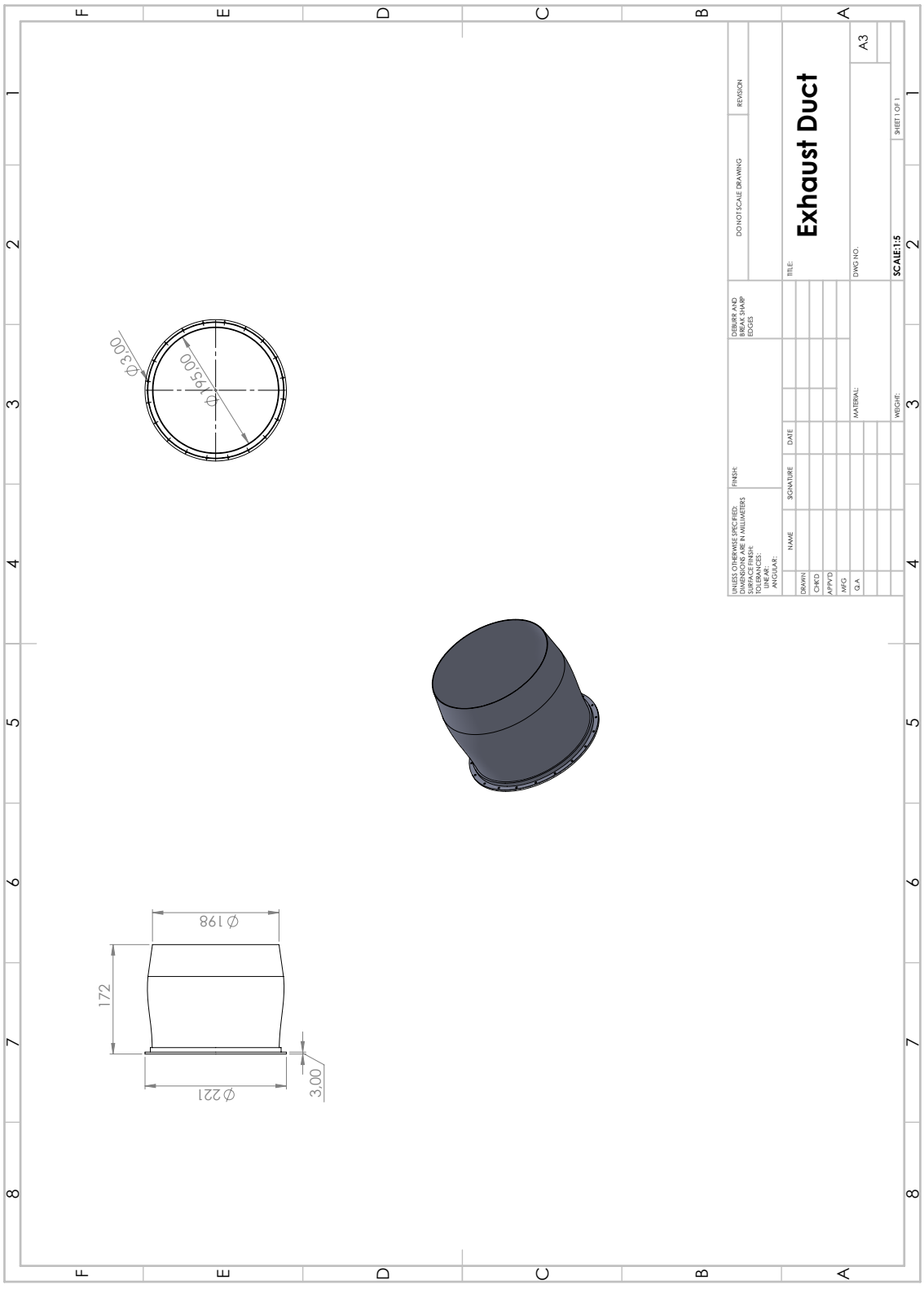

Figure B.7: Exhaust duct technical drawing

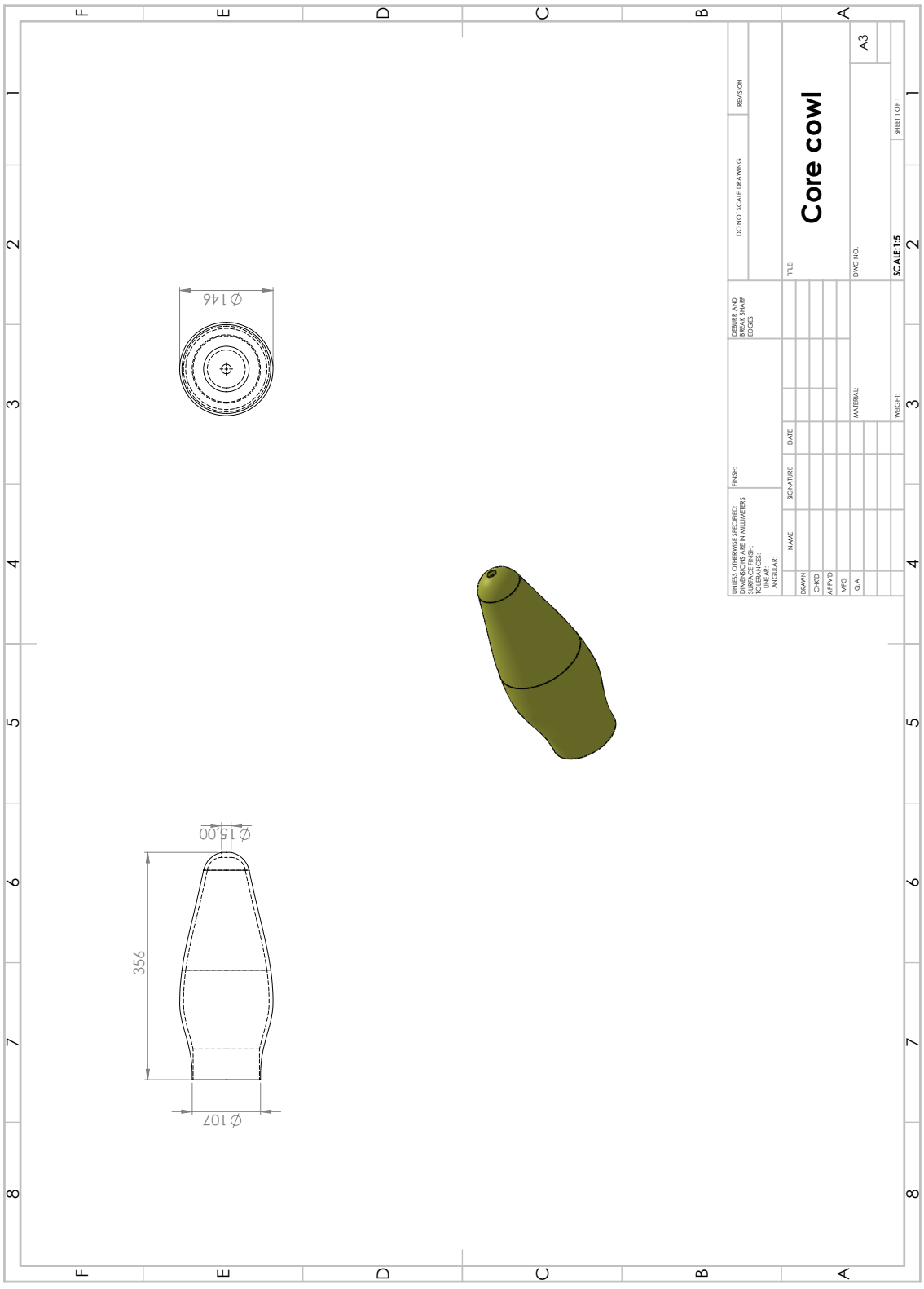

Figure B.8: Core cowl technical drawing

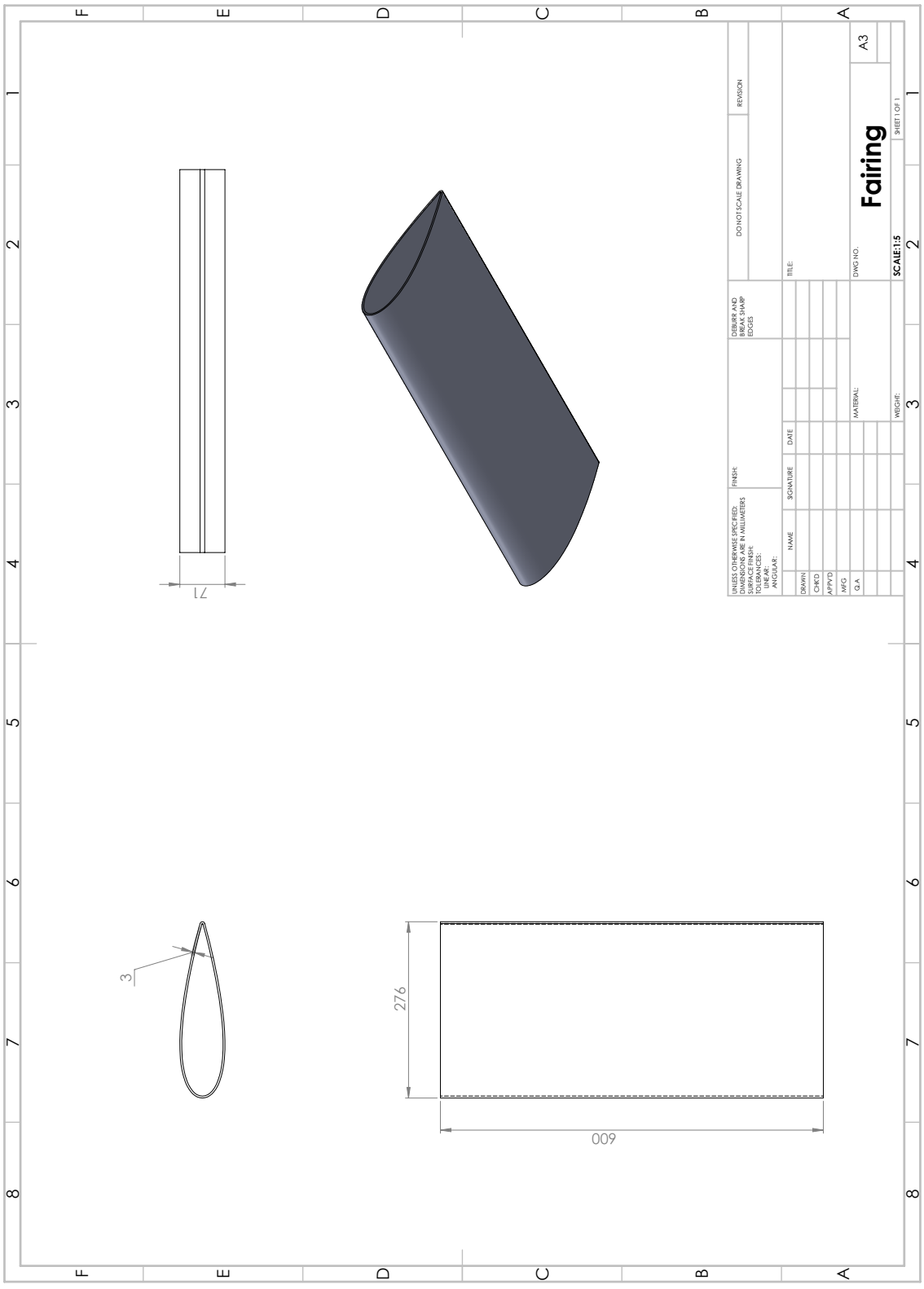

Figure B.9: Fairing

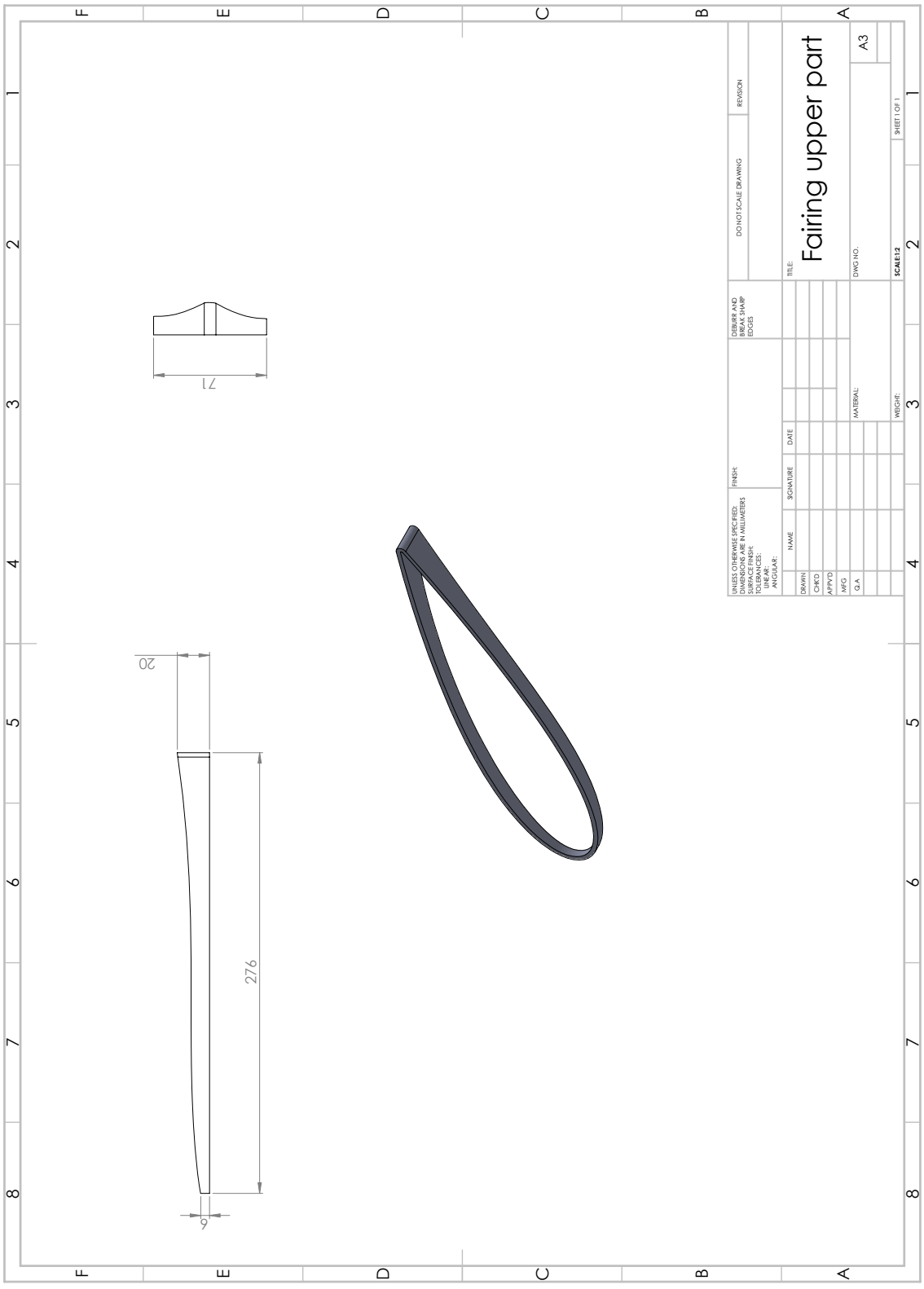

Figure B.10: Fairing upper part

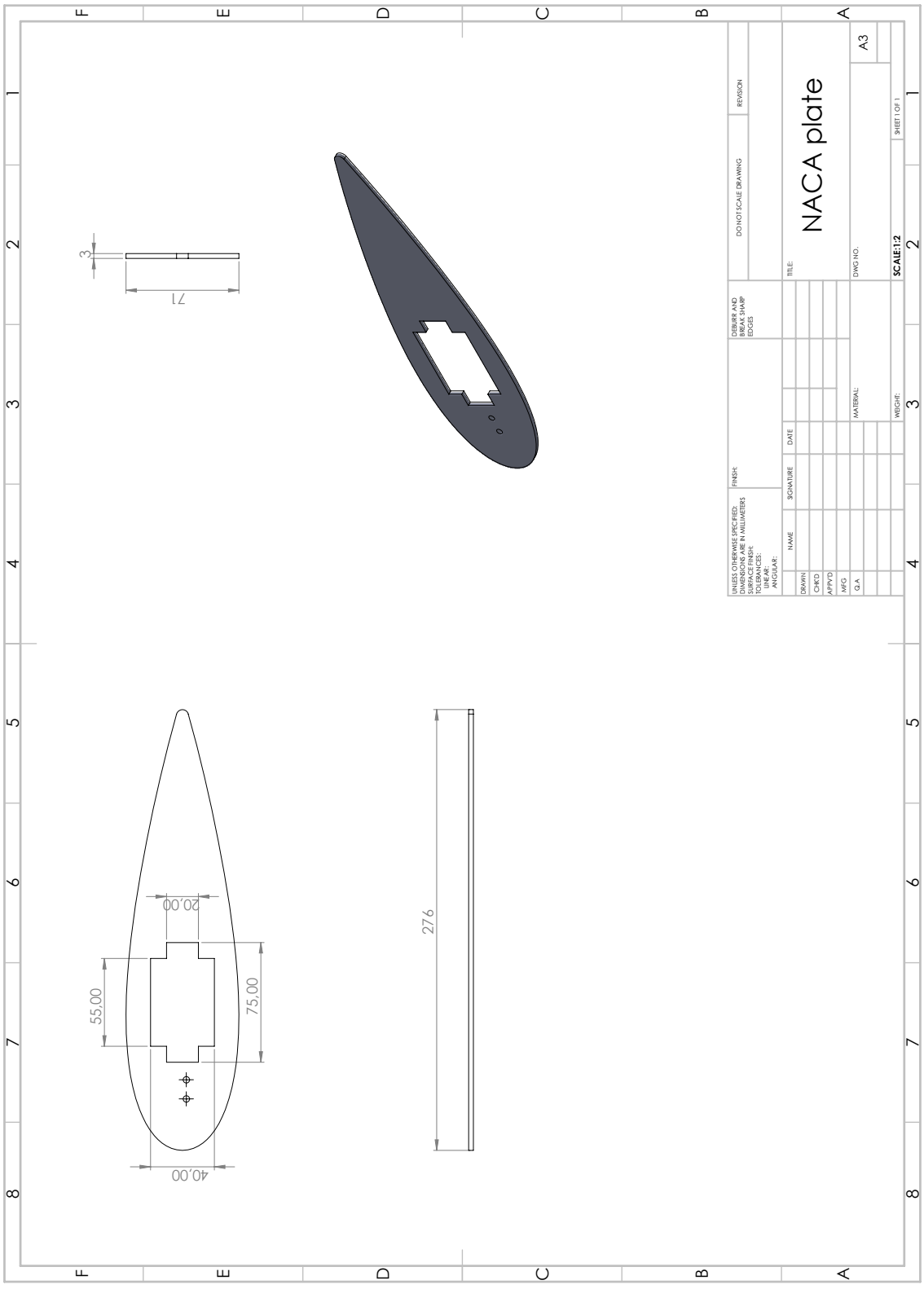

Figure B.11: NACA plate

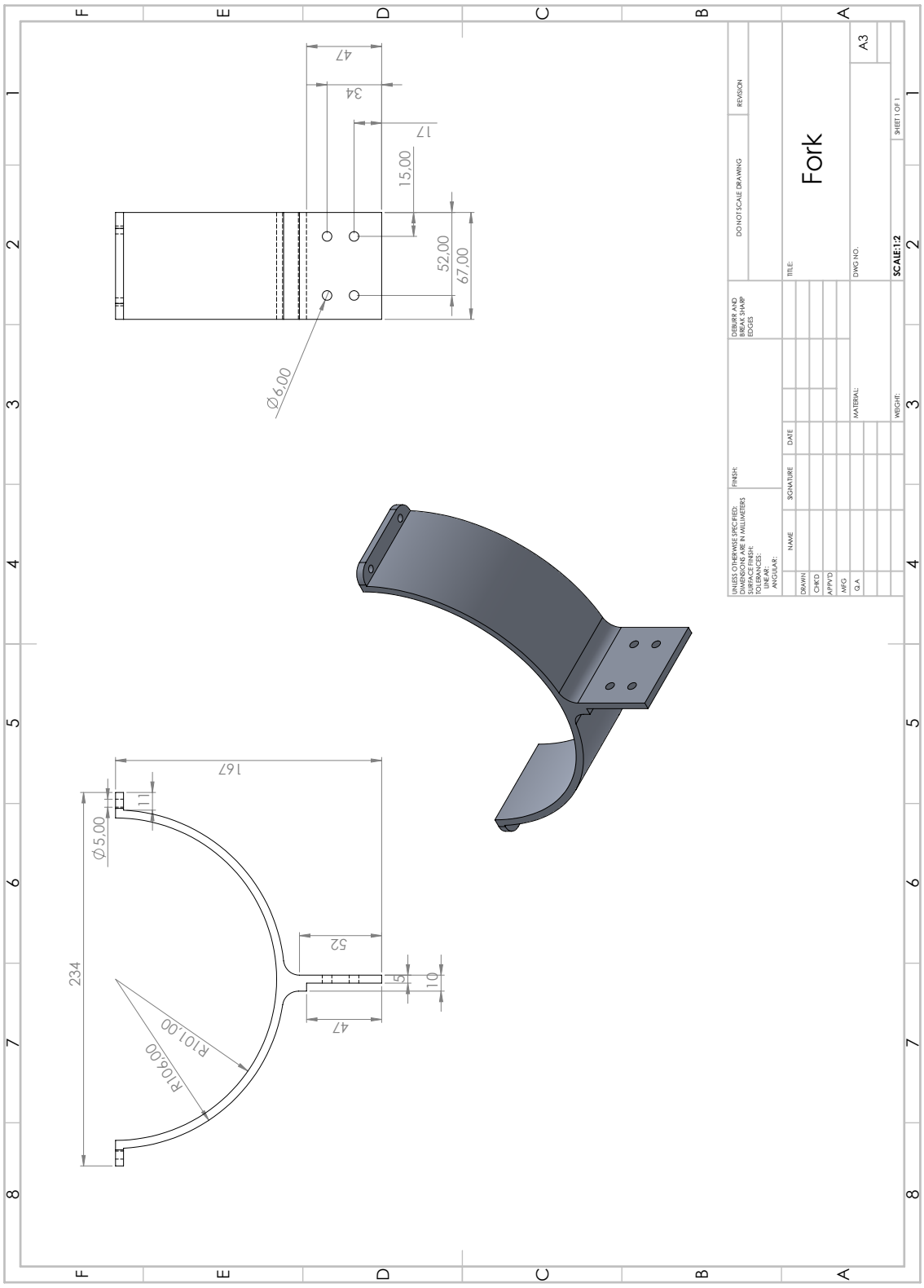

Figure B.12: Fork

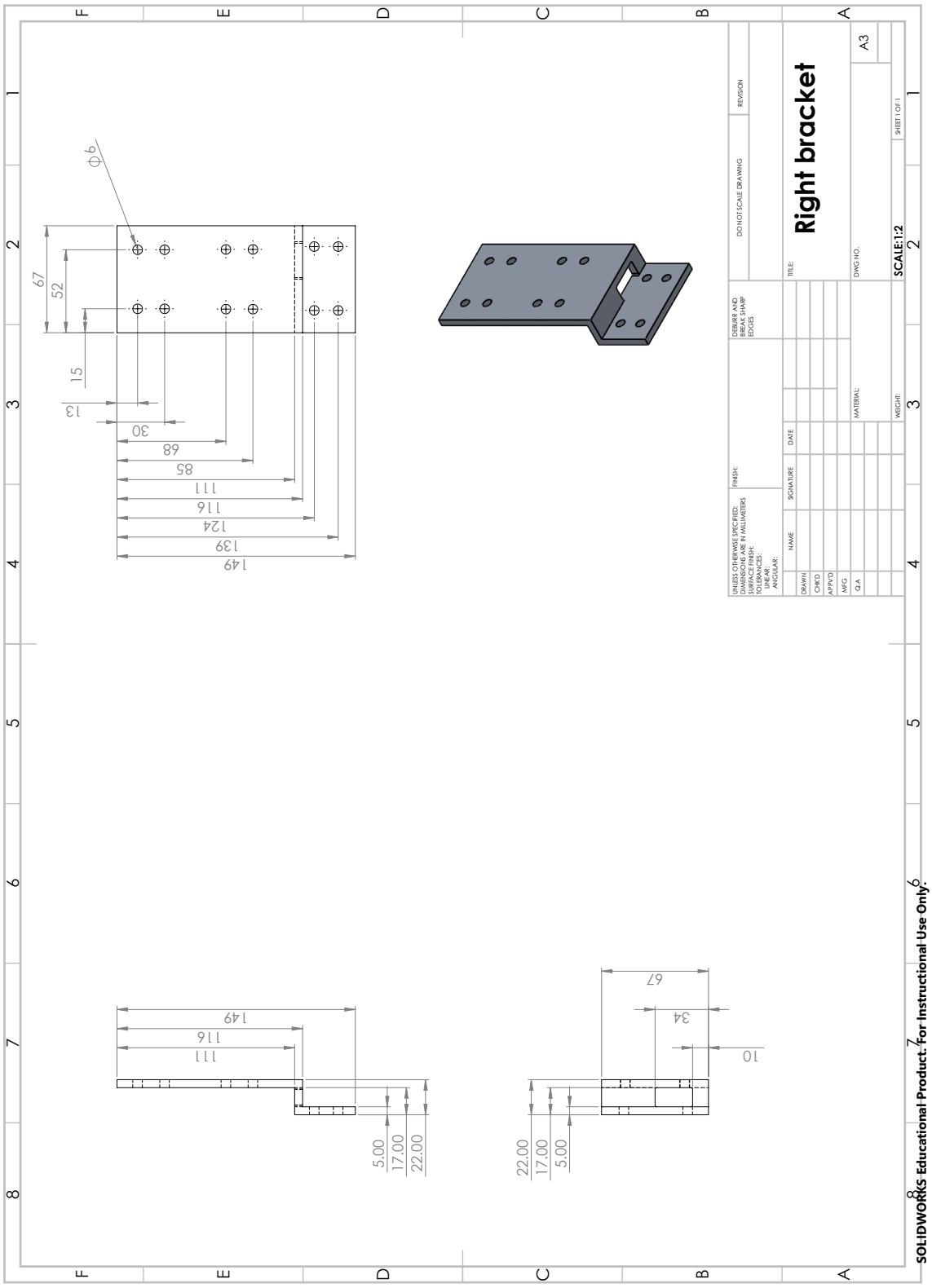

Figure B.13: Right bracket

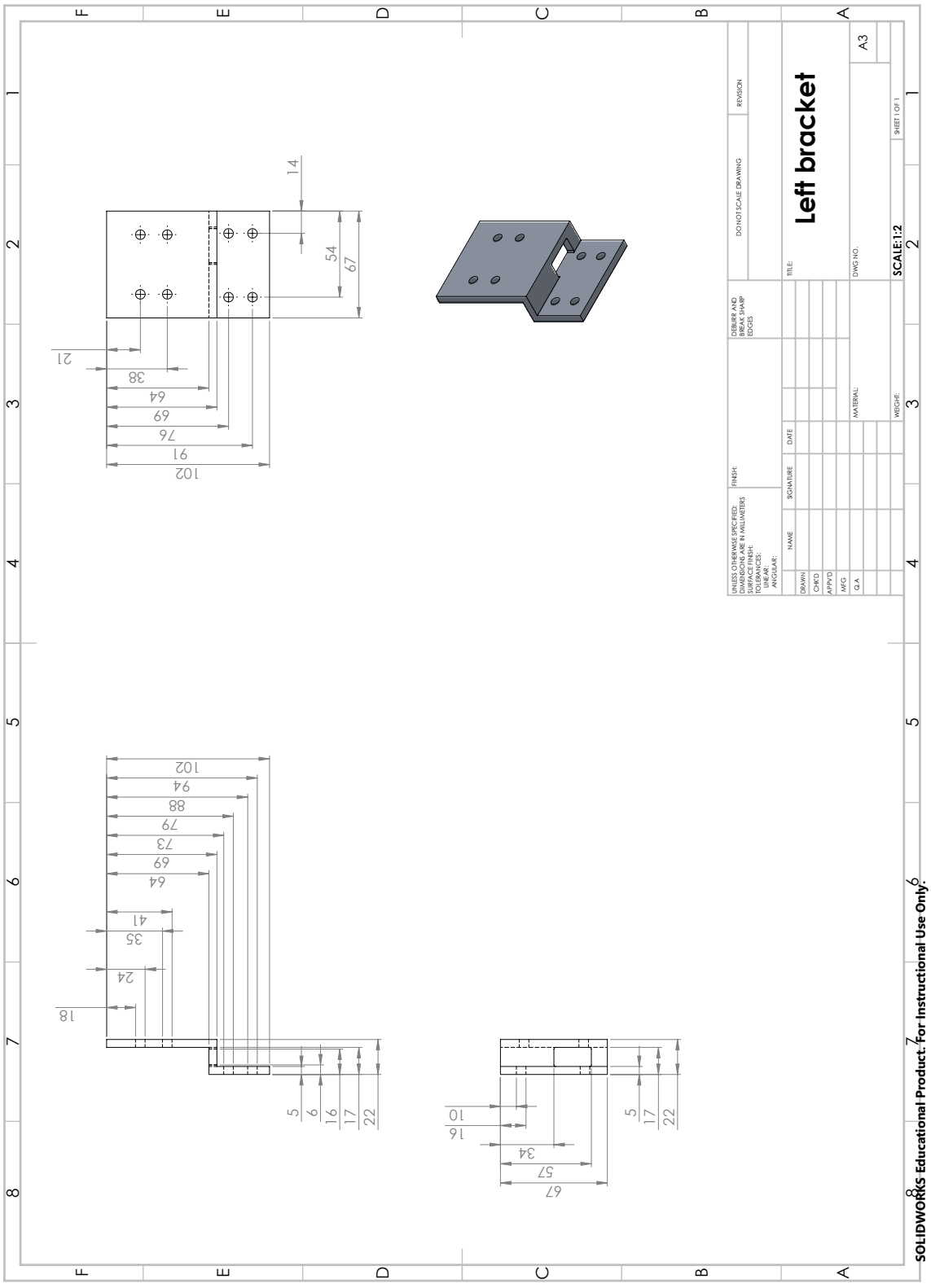

Figure B.14: Left bracket

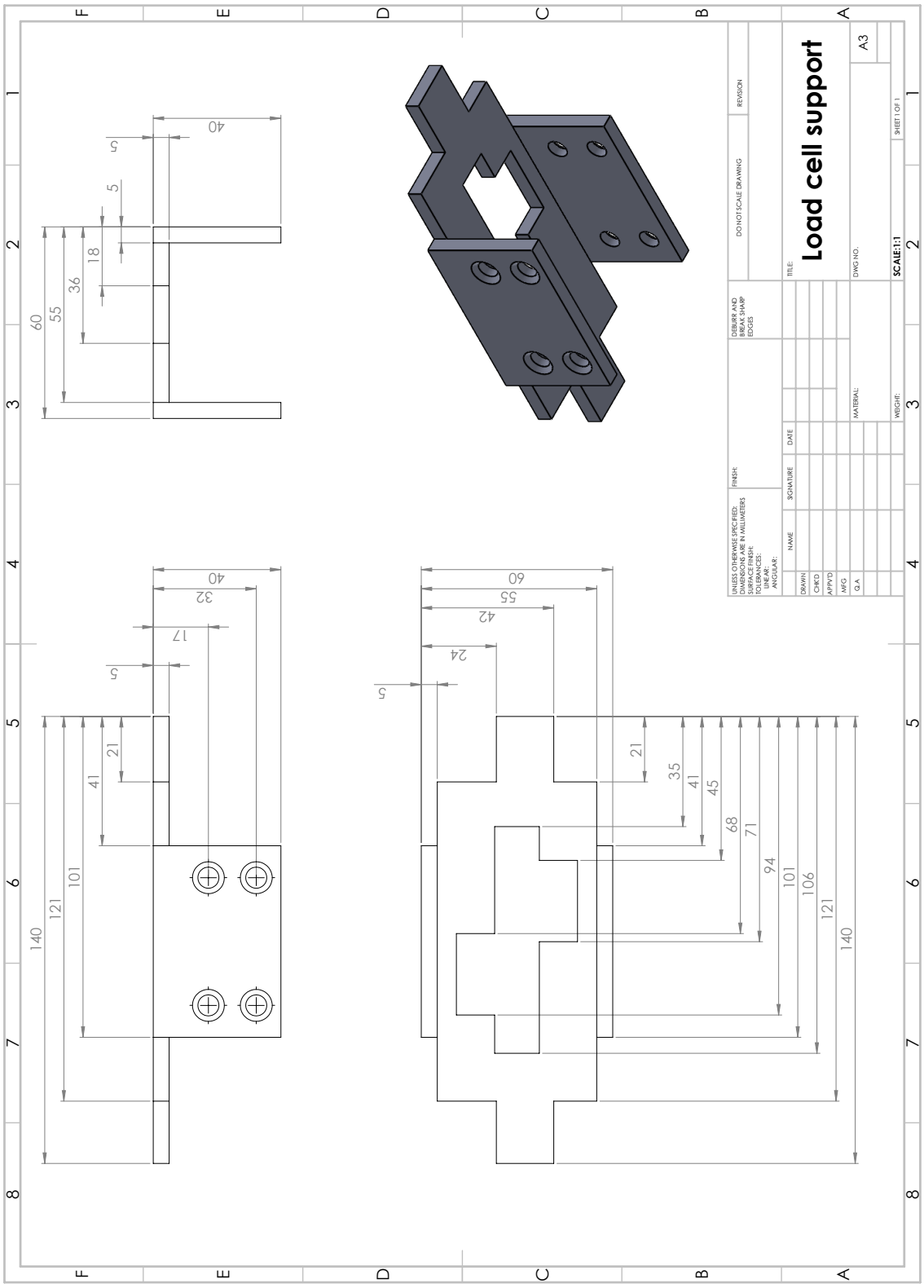

Figure B.15: Load cell support

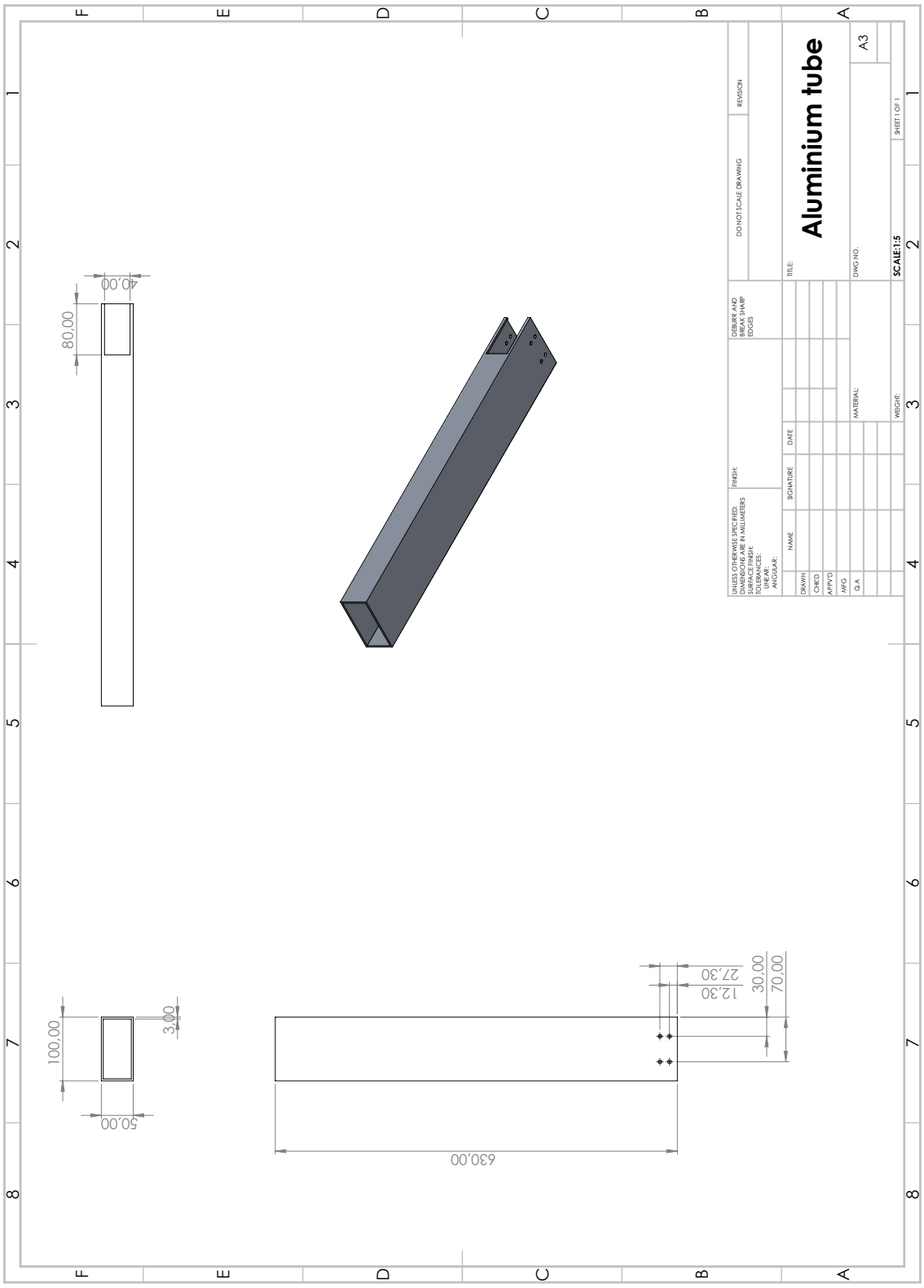

Figure B.16: Aluminium tube

C

Appendix 3

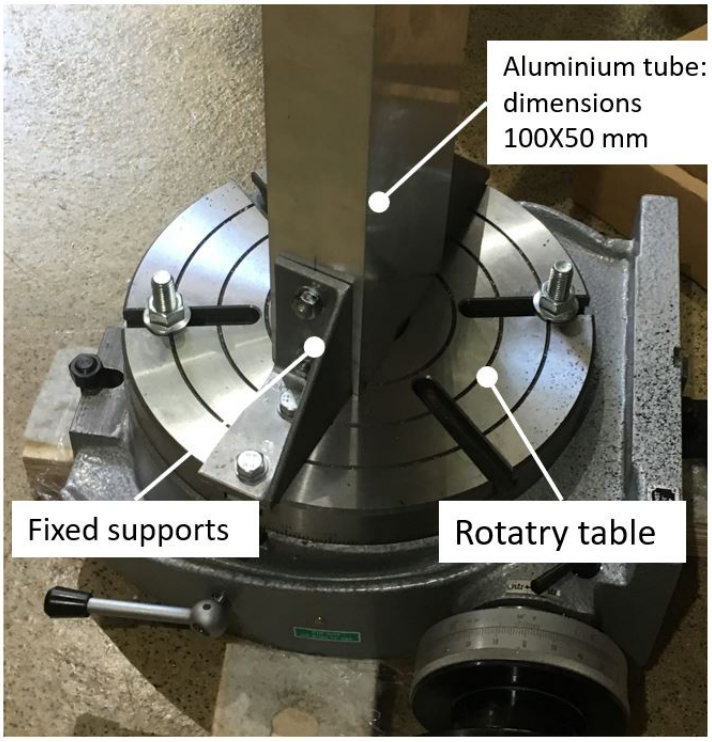

Figure C.1: Fixation detail between aluminium tube and rotary table